The Thesis Committee for Hongyang Fan
Certifies that this is the approved version of the following thesis:

An Improved Panel Method for the Prediction of Performance of Ducted Propellers

APPROVED BY
SUPERVISING COMMITTEE:

Supervisor: Spyros A. Kinnas

Ye Tian

An Improved Panel Method for the Prediction of Performance of Ducted Propellers

by

Hongyang Fan, B.S.E.

Thesis

Presented to the Faculty of the Graduate School of

The University of Texas at Austin

in Partial Fulfillment

of the Requirements

for the Degree of

MASTER OF SCIENCE IN ENGINEERING

The University of Texas at Austin

August 2015

Dedicated to my family and friends.

Acknowledgements

Firstly I would like to thank my supervisor, Prof. Kinnas, for his enduring assistance and encouragement during my graduate period at the University of Texas at Austin. His wisdom and passion for research and life lead me forward on my way of pursuing academic career and help me overcome difficulties in my daily life.

Then I would like to thank all my friends in the Computational Hydrodynamics Laboratory (CHL) for their unlimited help and kind companionship. I would especially thank Dr. Ye Tian for taking time out of his busy schedule to review my thesis and his strong support to my daily research. I would also like to thank Mr. Yiran Su, Weikang Du and Guangyao Wang for their significant help in both my research and life.

I would also thank my friends at Austin: Mr. Hai Yan, Mr. Xian Wu, Mr. Jinsong Liu and Miss Xiaoning Sun. Their companionship makes my life at Austin much more colorful and memorable than I have ever expected.

Finally, I would like to express my sincere appreciation to my father Cailiang Fan, my mother Fengjuan Wang, my sister Xiaodan Fan and my girl friend Lingna Yu. I would never finish this work without their love and encouragement.

This work was supported by the U.S. Office of Naval Research (Contracts N00014-10-1-0931 & N00014-14-1-0303) and Phases VI and VII of the "Consortium on Cavitation Performance of High Speed Propulsors" with the following current members: American Bureau of Shipping, Kawasaki Heavy Industry Ltd., Rolls-Royce Marine AB,

Rolls-Royce Marine AS, SSPA AB, Andritz Hydro GmbH, Wärtsilä Netherlands B.V., Wärtsilä Norway AS, Wärtsilä Lips Defense S.A.S., Wärtsilä CME Zhenjiang Propeller Co. Ltd and Steerprop Ltd.

Abstract

An Improved Panel Method for the Prediction of Performance of Ducted Propellers

by

Hongyang Fan, M.S.E.
The University of Texas at Austin, 2015
Supervisor: Spyros A. Kinnas

An improved perturbation potential based lower order panel method is applied to the three dimensional problems of flow around ducts and ducted propellers. One significant development of this method is the application of full wake alignment scheme in which the trailing vortex wake sheets of the blades are aligned with the local flow velocity by also considering the effects of duct and duct wake. A process of repaneling the duct is simultaneously introduced to improve the accuracy of evaluation of the method. The results from the improved wake model are compared with those from a simplified wake alignment scheme (PSF-2 type scheme). At the same time, full-blown RANS simulations of the three dimensional problem are conducted. The forces, i.e. thrust and torque on the propeller predicted by the present panel method under the improved wake alignment model show good agreement both with experimental measurements, a hybrid method developed by the Ocean Engineering Group of UT Austin, and the full

blown RANS simulations. Moreover, detailed pressure distribution on the blades and duct are compared among the various methods.

The interactive method which couples the lower order panel method with a two dimensional boundary layer solver through a wall transpiration model is also introduced. An assumption of two dimensional flow is made on the individual stations of a three dimensional geometries and the coupling is applied in a stripwise manner by including the interaction effects from other strips. The interactive method is then validated through the cases of bare ducts and ducted propellers. An important improvement is also made on the extension scheme for hydrofoils and propeller blades with blunt trailing edge. A more physical criterion has been established for determining the location of cut planes or the starting points of the extension. The extension scheme is applied to both axisymmetric problems and fully three dimensional problems. Correlations of results with experimental measurements and RANS simulations are presented.

Table of Contents

List of Tables

List of Figures

Nomenclature

Latin Symbols

C_D	Dissipation coefficient $(1/\rho U^3)\int_0^\delta \tau \frac{\partial u}{\partial \eta} d\eta$
C_f	Skin friction coefficient $C_f = \tau_{wall}/(0.5\rho U^2)$
C_p	Pressure coefficient $C_p = (P - P_O)/(0.5\rho n^2 D^4)$
D	Propeller diameter
G	Green's function
H	Shape factor, $H = \delta^*/\theta$
H^*	Kinetic energy shape factor, $H^* = \theta^*/\theta$
H_K	Kinematic shape parameter
J	Advance ratio based on V_s, $J = V_s/(nD)$
K_Q	Torque Coefficient, $K_Q = Q/(\rho n^2 D^5)$
K_{TD}	Thrust coefficient due to the duct, $K_{TD} = T_D/(\rho n^2 D^4)$
K_{TP}	Thrust coefficient due to the blades, $K_{TP} = T_P/(\rho n^2 D^4)$
n	Propeller rotational frequency
$\tilde{n}$	Transition disturbance amplification variable
P	Static pressure
P_o	Reference pressure at far upstream
$\boldsymbol{q}$	Total velocity
Q	Torque on the propeller
R	Propeller radius

R_e	Reynolds number based on inflow velocity
S_B	Body surface
S_W	Wake surface
T_D	Thrust on the duct
T_P	Thrust on the blades
u	Perturbation velocity
U_e	Edge velocity
U_{in}	Local inflow velocity
U^{inv}	Total inviscid velocity
U^{vis}	Total viscous velocity or edge velocity
u_τ	Wall shear velocity, $u_\tau = \sqrt{\tau_{wall}/\rho}$
V_s	Ship speed
y^+	Non-dimensional wall distance, $y^+ = \frac{u_\tau y}{v}$

Greek Symbols

α	Angle of attack
Γ	Circulation on blade sections
δ^*	Displacement thickness, $\delta^* = \int(1 - \frac{u}{U_e})dz$
Δt	Time step size
θ	Momentum thickness

θ^*	Kinetic energy thickness, $\theta^* = \int \frac{u}{U_e}(1 - \frac{u}{U_e})dz$
ρ	Fluid density
σ	Strength of blowing sources
τ	Wall shear stress
v	Fluid kinematic viscosity
ϕ	Perturbation potential
ϕ^{inv}	Inviscid perturbation potential
ϕ^{vis}	Viscous perturbation potential
ϕ_{total}	Total potential
ω	Propeller angular velocity

Acronyms

2-D	Two dimensional
3-D	Three dimensional
BEM	Boundary element method
CFD	Computational fluid dynamics
CPU	Central processing unit
RANS	Reynolds-averaged Navier-Stokes
VLM	Vortex-lattice method

Computer Program Names

PROPCAV	A cavitating propeller potential flow solver based on BEM
XFOIL	2-D integral boundary layer analysis code
FLUENT	A commercial RANS solver provided by ANSYS
MPUF-3A	A VLM based code for solving flow around propellers
Star-CCM+	A commercial RANS solver provided by CD-adapco

Chapter 1 Introduction

1.1 Background

As a viable alternative of propulsion, ducted propellers can produce higher efficiency than open propellers particularly at high loading conditions or low speeds. The utilization of ducted propellers can be found in many types of marine vehicles and structures such as the floating production storage and offloading (FPSO) and liquid natural gas (LNG). The duct surrounding the blades can provide extra benefits: compared to open propellers, the propellers bounded by the duct become less sensitive to ambient flow and more resistant to environmental debris.

Satisfactory predictions of the performance of ducted propellers have been a significant concern in the marine industry for a long time. Full blown Reynolds Averaged Navier-Stokes (RANS) simulation, though can provide reliable results, is considered to be numerically too expensive especially at the design stage. Additionally, the RANS simulations require significant time in setting the proper grid. Boundary element methods are found to be an ideal alternative since they do not require the discretization of the whole fluid domain and therefore are much more computationally efficient. Hess et al. (1964) published the pioneering work of panel method. Since then, a large number of panel codes have been proposed. Subsequently, Gibson and Levis (1973), Hess et al. (1985) developed the panel method for the specific applications of marine propellers. Morino et al. (1974) introduced a panel method based on Green's formulation in which the primary unknown was the potential. Lee (1987) carried out a comprehensive

investigation of panel methods for a more suitable formulation for simulations of marine propellers.

The free vortex sheets shed from the trailing edge of a propeller blade are material surfaces, which have to be aligned with the local flow velocity. The influence of the wake shape on the prediction of propeller performance was initially discussed by Kerwin and Lee (1978). After that Greeley et al. (1982) proposed a fast scheme of wake alignment denoted as PSF-2 wake alignment. In this scheme, the trailing wake shape of a propeller subjected to axisymmetric inflow is investigated through an iterative vortex lattice method. The correct pitch of the wake geometry is firstly calculated at some points in the wake area, after which the wake geometry is updated by adopting the newly computed pitch distribution. The process continues until a convergence on wake geometry is achieved. Kinnas and Pyo (1997) improved this scheme such that it is applicable to the problem of a propeller subjected to inclined inflows. The influence of the shaft inclination on the velocity within the wake area has been included and the predicted performance agreed quite well with experimental data. Later Pyo and Kinnas (1997) developed a high order panel method by adopting biquadratic dipoles on the trailing vortex sheet. This method, though produced good prediction of the roll-up characteristic of the wake and the force performance around design advance ratio, was relatively more time-consuming than lower order method. More recently Lee and Kinnas (2004) implemented an unsteady wake alignment scheme based on lower order panel method. The method introduced a finite core tip vortex at the tip of the wake sheet and it was applied to the numerical modeling of unsteady wake sheet and developed tip vortex

cavitation on hydrofoils and marine propellers. Tian and Kinnas (2012) presented a wake alignment model based on a pseudo-unsteady scheme for a lower order panel method. The scheme is validated with experiments and RANS results in the case of propellers at both design loading condition and high loading conditions.

To include the effects of viscosity into consideration is a common concern when modeling ducted propellers with boundary element methods. Usually this is addressed by coupling inviscid formulation of boundary element methods with either two dimensional or three dimensional boundary layer solvers. Drela (1989) initially developed the coupling of a vorticity based panel method with a two dimensional boundary layer solver, XFOIL, for the problems of airfoils. Milewski (1997) made the coupling more physical by applying three dimensional boundary layer solver rather than two dimensional ones. However it was proved to be much too time-consuming for solving the three dimensional boundary layer equations. Hufford (1992, 1994) simplified the coupling by applying a two dimensional boundary layer solver where the boundary layer equations were solved in a stripwise manner and three dimensional sources were placed on the targeted geometries to partially resolve for the three dimensional effects. Sun (2008) as well as Sun and Kinnas (2008) further simplified the coupling by adopting two dimensional sources rather than three dimension sources as used in Hufford's method and neglecting the effects from other geometric strips. Yu (2012) and Kinnas et al. (2012) developed a coupling scheme where three dimensional sources were applied and the extra effects from other strips were taken into consideration. Purohit (2013) and Kinnas et al. (2013) further

improved Yu's scheme by including important interaction terms between strips which were previously neglected.

1.2 Objective

The main objective of this thesis is to develop a more reasonable wake model for the present boundary element method by aligning the wake panels with the local flow velocity and including the effects of all the singularities on blades and duct and achieve satisfactory correlations on general force as well as detailed pressure distribution with experimental measurements and full blown RANS simulation.

1.3 Organization

This thesis is organized into six chapters.

Chapter 1 contains the literature review, the objective and the organization of the current work.

Chapter 2 introduces the inviscid formulation of the lower order panel method, the two dimensional boundary layer solver coupled with the panel method and the iterative algorithm of the coupling for two dimensional problems.

Chapter 3 demonstrates the coupling of a three dimensional panel method with a two dimensional boundary solver for three dimensional problems. The method takes the assumption that the boundary layer growth in the spanwise direction is negligible and takes into consideration the interaction term between different strips and blades.

Chapter 4 presents in details the improved wake alignment model which aligns the vortex wake sheet with local flow velocity. The validity of the wake model is firstly confirmed within a bare duct case. Then the present panel method with the improved wake model is applied in two cases of ducted propellers. The effects of viscosity are not involved at this stage. The overall forces, i.e., the thrust and torque predicted by the present method are correlated with experimental measurement, a hybrid method also developed by the Ocean Engineering Group at UT Austin which is also introduced by Tian et al. (2015). The method couples a potential flow based vortex lattice method (VLM) with an axisymmetric swirl RANS solver and full blown RANS simulations. The pressure distribution on the blades and duct are also investigated for future cavitation flow simulation.

Chapter 5 shows the validation of the coupling of the lower order panel method with a two dimensional boundary layer solver through different cases of bare ducts and ducted propellers. An improved extension scheme has been introduced into bare ducts with blunt trailing edge or ducted propellers with non-zero trailing edge duct such that the coupling method could be applied to account for the recirculation zone in the vicinity of the blunt trailing edge.

Chapter 6 summarizes the work of this thesis and puts forward recommendations for future work.

Chapter 2 Two Dimensional Viscous/Inviscid Interactive Method

In this chapter, a summary would be made on the 2-D viscous/inviscid interactive method, as also introduced by Yu (2012) and Purohit (2013). The method couples a two dimensional perturbation potential based panel method with a two dimensional integral boundary layer solver to resolve the viscous flow around two dimensional geometries.

The chapter starts with the introduction of the 2-D lower order potential based panel method. The 2-D integral boundary layer equations are presented next. Then the wall transpiration model which connects the panel method and the boundary layer solver is introduced. Finally the coupling algorithm through the wall transpiration model is discussed.

2.1 Inviscid Formulation

2.1.1 Governing Equations

In the perturbation potential based lower order panel method used in this thesis, sources and dipoles of constant strength are assumed on each panel of the blades, duct as well as the trailing wakes.

Consider the flow field shown in Figure 2.1 where a two dimensional hydrofoil is in presence. The total velocity of the flow field is decomposed into two components: the inflow velocity and the perturbation velocity due to the presence of obstacles such as the hydrofoil, written as:

$$\boldsymbol{q} = \boldsymbol{U_{in}} + \boldsymbol{u} \tag{2.1}$$

where $\boldsymbol{q}$ is the total velocity, $\boldsymbol{U_{in}}$ is the inflow velocity and $\boldsymbol{u}$ is the perturbation velocity.

$$\boldsymbol{u} = \nabla\phi \tag{2.2}$$

where ϕ is the perturbation potential.

The perturbation velocity field is then governed by the following Laplace equation:

$$\nabla^2\phi = 0 \tag{2.3}$$

If the flow is irrotational, the total potential ϕ_{total} can also be defined by

$$\boldsymbol{q} = \nabla\phi_{total} \tag{2.4}$$

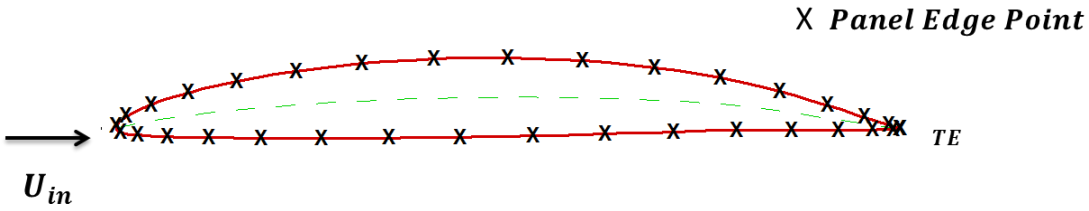

Figure 2.1 Diagram of the paneling on a 2-D hydrofoil and its wake

2.1.2 Boundary Conditions

Since the flow cannot penetrate the solid surface of the hydrofoil shown, Equation (2.5) needs to be met as the kinematic boundary condition:

$$\frac{\partial\phi}{\partial\boldsymbol{n}} = -\boldsymbol{U_{in}} \cdot \boldsymbol{n} \tag{2.5}$$

where $\boldsymbol{n}$ is the normal vector on the solid surface pointing into the flow field.

In addition there should be no effect of hydrofoil when the point of interest is far away from the hydrofoil, that is, the induced perturbation velocity there should be zero.

$$\boldsymbol{u} = \nabla\phi = \mathbf{0} \tag{2.6}$$

On the other hand, as a free vortex sheet shedding from the trailing edge of the hydrofoil, the wake is a material surface that cannot bear pressure jump. Kutta condition is here applied, implying that the velocity at the trailing edge is of finite magnitude:

$$\nabla\phi = finite \text{ at TE} \tag{2.7}$$

2.1.3 Boundary Integrated Form of Equation

By applying the Green's second identity, the Laplace equation (2.3) can be reformatted as

$$\begin{aligned}\frac{\phi_p}{2} = \iint_{S_B}\left[-\phi_q\frac{\partial G(p,q)}{\partial \boldsymbol{n_q}} + \frac{\partial \phi_q}{\partial \boldsymbol{n_q}}G(p,q)\right]dS \\ + \int_{S_W}\Delta\phi_w\frac{\partial G(p,q)}{\partial \boldsymbol{n_q}}dS\end{aligned} \tag{2.8}$$

S_B, S_W : the solid surface of the hydrofoil and the surface of the trailing edge wake.

p, q : control point and variable point on the boundary.

$\boldsymbol{n_q}$: vector at the point q directing into the flow field.

$G(p,q)$ is the Green's function which has the form of $\frac{\ln(r(p,q))}{2\pi}$ in two dimensional problems and the form of $-\frac{1}{4\pi r(p,q)}$ in three dimensional problems. Here $r(p,q)$ is the distance between the points p and q.

The physical meaning of equation (2.8) is that the perturbation potential at a point p is attributed by the potentials induced by sources of strength $\frac{\partial \phi_q}{\partial \boldsymbol{n_q}}$ and dipoles of strength ϕ_q on the hydrofoil surface and dipoles of strength $\Delta\phi_w$ on the trailing edge wake.

2.1.4 Discretized Form of Equation

Assume that the hydrofoil in Figure 2.1 is discretized into N straight panels and its trailing edge wake into N_W panels by certain spacing law. The boundary integrated equation (2.8) can thus be discretized into the following form:

$$\sum_{j=1}^{N} D_{ij}\phi_j = \sum_{j=1}^{N} S_{ij}\left(\frac{\partial \phi}{\partial \boldsymbol{n}}\right)_j - W_i \Delta\phi_W \tag{2.9}$$

D_{ij} : dipole influence coefficient of panel j on control point i

S_{ij} : source influence coefficient of panel j on control point i

W_i : dipole influence coefficient of the trailing edge wake on control point i

For 2-D steady state problems, equation (2.6) leads to the modified Morino-Kutta condition proposed by Lee (1987).

$$\Delta\phi_W = \phi_W^+ - \phi_W^- + \boldsymbol{U}_\infty \cdot \boldsymbol{r_{TE}} \tag{2.10}$$

$\boldsymbol{U}_\infty$: inflow velocity locally at the trailing edge of the hydrofoil

$\boldsymbol{r_{TE}}$: vector from the control point of (-) panel to the (+) panel at the trailing edge

The term $\boldsymbol{U}_\infty \cdot \boldsymbol{r_{TE}}$ is negligible as long as the solid surface is sufficiently discretized and a small angle of attack is in presence.

By substituting (2.10) into (2.9) and neglecting the term of $\boldsymbol{U}_\infty \cdot \boldsymbol{r_{TE}}$, (2.9) can be organized into the following discretized equation:

$$\sum_{j=1}^{N} A_{ij}\phi_j = \sum_{j=1}^{N} S_{ij}\left(\frac{\partial\phi}{\partial\boldsymbol{n}}\right)_j \tag{2.11}$$

In which the effects of the wake have been included through updating the dipole influence coefficient by the hydrofoil from D_{ij} to A_{ij}.

2.2 Viscous Formulation

A 2-D wall transpiration model is applied in order to include the effects of viscosity. The lower order panel method is coupled with a 2-D integral boundary layer solver through the term of edge velocity.

2.2.1 2-D Wall Transpiration Model

As shown in Figure 2.2, blowing sources which induce normal velocity on the surfaces are added into the inviscid formulation of the panel method. The surrounding flow is pushed away from the solid surface such that the boundary layer can be simulated.

The blowing sources should be granted with proper strength so that the edge velocity U_e at $y = y_e$ is the same as that in the viscous flow. By applying the steady Bernoulli Equation and the boundary layer theory, it can then be deduced that the pressure at the point W' is the same as that at the point W in the viscous flow. That is, the equivalent inviscid flow shares the same pressure distribution with the real viscous flow.

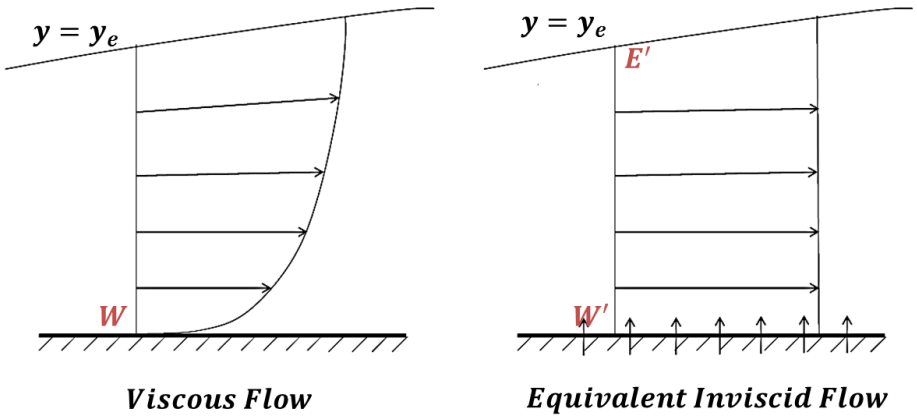

Figure 2.2 Diagram for wall transpiration model, adjusted from Figure 2.1 of Yu (2012)

2.2.2 Expression of Edge Velocity

By taking into account the effects of blowing sources, (2.11) is updated into

$$\sum_{j=1}^{N} A_{ij}\phi_j^{vis} = \sum_{j=1}^{N} S_{ij}\left(\frac{\partial \phi}{\partial \boldsymbol{n}}\right)_j + \sum_{j=1}^{N+N_W} B_{ij}\sigma_j \qquad (2.12)$$

B_{ij} : analogous to S_{ij}, which is the the source influence coefficient on control point i by panel j of the foil and wake.

σ_j : unknown strength of blowing source on panel j.

ϕ_j^{vis} : viscous potential which is the expression of perturbation potential after taking into consideration the effects of blowing sources

The blowing source is directly associated with the boundary layer parameters displacement thickness and edge velocity as follows:

$$\sigma = \frac{\partial(U_{vis}\delta^*)}{\partial s} = \frac{\partial m}{\partial s} \tag{2.13}$$

U_{vis}: edge velocity or viscous velocity

δ^* : displacement thickness

m : mass defect due to the boundary layer

Equation (2.12) can be formed into a matrix form as

$$\boldsymbol{A\phi^{vis}} = \boldsymbol{S}(\frac{\boldsymbol{\partial\phi}}{\boldsymbol{\partial n}}) + \boldsymbol{B\sigma} \tag{2.14}$$

where

$$\begin{aligned} \boldsymbol{A} &= [A_{ij}] \\ \boldsymbol{S} &= [S_{ij}] \\ \boldsymbol{B} &= [B_{ij}] \\ \boldsymbol{\phi^{vis}} &= [\phi_j^{vis}] \\ \frac{\boldsymbol{\partial\phi}}{\boldsymbol{\partial n}} &= \left[\left(\frac{\partial\phi}{\partial n}\right)_j\right] \\ \boldsymbol{\sigma} &= [\sigma_j] \end{aligned} \tag{2.15}$$

Therefore:

$$\boldsymbol{\phi^{vis} = A^{-1}S(\frac{\partial \phi}{\partial n}) + A^{-1}B\sigma} \tag{2.16}$$

The total potential in the case of viscous flow should be the sum of the inflow potential and the viscous perturbation potential:

$$\begin{aligned} \boldsymbol{\phi_{total}^{vis}} &= \boldsymbol{\phi_{in} + \phi^{vis}} \\ &= \boldsymbol{\phi_{in} + A^{-1}S\left(\frac{\partial \phi}{\partial n}\right) + A^{-1}B\sigma} \\ &= \boldsymbol{\phi_{in} + \phi^{inv} + A^{-1}B\sigma} \\ &= \boldsymbol{\phi_{total}^{inv} + A^{-1}B\sigma} \\ &= \boldsymbol{\phi_{total}^{inv} + H\sigma} \end{aligned} \tag{2.17}$$

Where $\boldsymbol{H = A^{-1}B}$. It can be seen that the viscous total potential can be obtained by adding the induced potential by the blowing sources $\boldsymbol{H\sigma}$ to the inviscid total potential.

Differentiating the viscous total potential along the streamwise direction of the hydrofoil will give the viscous velocity or edge velocity.

$$\begin{aligned} \boldsymbol{U^{vis}} &= \frac{\partial \boldsymbol{\phi_{total}^{vis}}}{\partial s} \\ &= \frac{\partial \boldsymbol{\phi_{total}^{inv}}}{\partial s} + \frac{\partial \boldsymbol{H}}{\partial s}\boldsymbol{\sigma} \\ &= \boldsymbol{U^{inv} + C\sigma} \end{aligned} \tag{2.18}$$

Where

$$\boldsymbol{C} = \frac{\partial}{\partial s}(\boldsymbol{H}) = \frac{\partial}{\partial s}(\boldsymbol{A^{-1}B}) \tag{2.19}$$

(2.18) states that the viscous velocity $\boldsymbol{U^{vis}}$ is the sum of the inviscid velocity $\boldsymbol{U^{inv}}$ and the induced velocity by the blowing sources $\boldsymbol{C\sigma}$. It should be noted that the inflow potential $\boldsymbol{\phi_{in}}$ does not exist in the case of rotational inflows. Even though the derivation of (2.18) uses the inflow potential $\boldsymbol{\phi_{in}}$, it is still general and valid for cases with or without the inflow potential. This is because (2.16) is an expression in terms of velocity instead of potential as mentioned by Yu (2012).

The potential as well as velocity on the trailing vortex wake can be derived in a similar way. Firstly the viscous perturbation on the wake can be obtained as the sum of the influence of sources and dipoles on the hydrofoil and the blowing sources on the hydrofoil and the wake.

$$\phi_i^{w,vis} = \sum_j^N A_{ij}^w \phi_j^{vis} + \sum_j^N S_{ij}^w \left(\frac{\partial \phi}{\partial n}\right)_j + \sum_{j=1}^{N+N_W} B_{ij}^w \sigma_j \tag{2.20}$$

Where A_{ij}^w is the dipole influence coefficient on the control point i of the wake by the panel j on the hydrofoil; S_{ij}^w is the source influence coefficient on the control point i on the wake by the panel j on the hydrofoil; B_{ij}^w is the source influence coefficient on the control point i on the wake by the panel j on the hydrofoil or on the wake.

Again, (2.20) can be rewritten in a matrix form as follows:

$$\boldsymbol{\phi^{w,vis} = A^{w}\phi^{vis} + S^{w}\left(\frac{\partial \phi}{\partial n}\right) + B^{w}\sigma} \tag{2.21}$$

$$\begin{gathered}
\boldsymbol{A^{w}} = \left[A_{ij}^{w}\right] \\
\boldsymbol{S^{w}} = \left[S_{ij}^{w}\right] \\
\boldsymbol{B^{w}} = \left[B_{ij}^{w}\right] \\
\boldsymbol{\phi^{vis}} = \left[\phi_{j}^{vis}\right] \\
\boldsymbol{\frac{\partial \phi}{\partial n}} = \left[\left(\frac{\partial \phi}{\partial n}\right)_{j}\right] \\
\boldsymbol{\sigma} = [\sigma_{j}]
\end{gathered} \tag{2.22}$$

The total viscous potential on the wake can be derived as:

$$\begin{aligned}
\boldsymbol{\phi_{total}^{w,vis}} &= \boldsymbol{\phi_{in} + \phi^{w,vis}} \\
&= \boldsymbol{\phi_{in} + A^{w}\phi^{vis} + S^{w}\left(\frac{\partial \phi}{\partial n}\right) + B^{w}\sigma} \\
&= \boldsymbol{\phi_{in} + A^{w}A^{-1}S\left(\frac{\partial \phi}{\partial n}\right) + A^{w}A^{-1}B\sigma + S^{w}\left(\frac{\partial \phi}{\partial n}\right) + B^{w}\sigma} \\
&= \boldsymbol{\phi_{total}^{w,inv} + (A^{w}A^{-1}B + B^{w})\sigma} \\
&= \boldsymbol{\phi_{total}^{w,inv} + H^{w}\sigma}
\end{aligned} \tag{2.23}$$

The edge velocity on the wake can similarly be deduced by differentiating the total viscous potential in (2.22) in the streamwise direction:

$$\boldsymbol{U^{w,vis} = U^{w,inv} + C^{w}\sigma} \tag{2.24}$$

Where

$$\boldsymbol{C^w} = \frac{\partial}{\partial s}(\boldsymbol{H^w}) = \frac{\partial}{\partial s}(\boldsymbol{A^w A^{-1} B} + \boldsymbol{B^w}) \tag{2.25}$$

(2.18) and (2.25) can be written in a general form as

$$\boldsymbol{U^{w,vis}} = \boldsymbol{U^{w,inv}} + \boldsymbol{G\sigma} \tag{2.26}$$

Where

$$\begin{aligned} \boldsymbol{G} &= \boldsymbol{C} \qquad on\ hydrofoil \\ \boldsymbol{G} &= \boldsymbol{C^w} \qquad on\ wake \end{aligned} \tag{2.27}$$

2.3 2-D Coupling Algorithm

The inviscid panel method is coupled with a two dimensional boundary layer solver XFOIL. The 2-D integral boundary layer equations involved in XFOIL is listed and the coupling algorithm is then explained in details.

2.3.1 2-D Integral Boundary Layer Equations

- **Momentum Equation**

$$\frac{\partial \theta}{\partial s} + (2 + H)\frac{\theta}{U_e}\frac{dU_e}{ds} = \frac{C_f}{2} \tag{2.28}$$

- **Kinetic Energy Equation**

$$\theta\frac{dH^*}{ds} + H^*(1 - H)\frac{\theta}{U_e}\frac{dU_e}{ds} = 2C_D - H^*\frac{C_f}{2} \tag{2.29}$$

- **Closure**

  Closure for laminar flow

$$\frac{d\tilde{n}}{ds} = \frac{d\tilde{n}(H_k)}{dR_{e\theta}} \frac{R_{e\theta}(H_k, \theta)}{ds} \tag{2.30}$$

  Closure for turbulent flow

$$\frac{\delta}{C_\tau}\frac{dC_\tau}{ds} = 5.6\left[C_{\tau_{EQ}}^{\frac{1}{2}} - C_\tau^{\frac{1}{2}}\right] + 2\delta\left\{\frac{4}{3\delta^*}\left[\frac{C_f}{2} - \left(\frac{H_k - 1}{6.7H_k}\right)^2\right] - \frac{1}{U_e}\frac{dUe}{ds}\right\} \tag{2.31}$$

2.3.2 Coupling Procedure

According to (2.24), the edge velocity is dependent on the blowing sources on the body surface and wake. On the other hand, the blow source strengths themselves are unknown. An iterative algorithm for two dimension viscous/ inviscid interactive method is proposed and its principles are presented.

Firstly the inviscid panel method is performed and the inviscid velocity U^{inv} is used as an initial guess for the edge velocity in the viscous formulation. Then the two dimensional integral boundary layer equations are solved for boundary layer parameters and the edge velocity can then be updated based on (2.24). The iteration continues until a convergence is reached. The details are shown in the following flowchart.

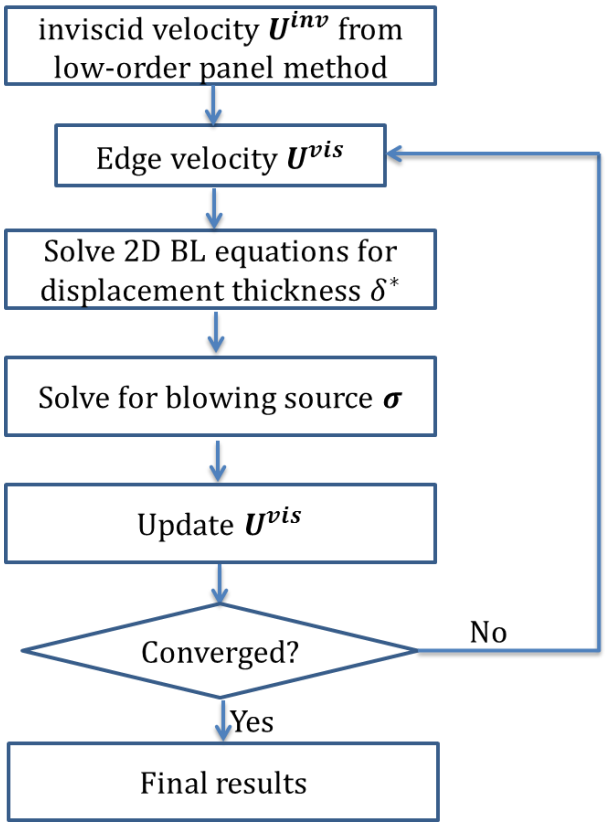

Figure 2.3 Coupling algorithm of the 2-D viscous/inviscid interactive method

Chapter 3 Three Dimensional Viscous/Inviscid Interactive Method

In this chapter, a summary of the lower order panel method for three dimensional problems, as also introduced in Yu (2012) and Purohit (2013), is provided. In order to resolve the effects of viscosity, the panel method is coupled with a two dimensional integral boundary layer solver which is also mentioned in the last chapter. Unlike in 2-D problems, in 3-D problems, it would be computationally too intensive to solve for the exact 3-D boundary layer structures through 3-D integral boundary layer equations. For a 3-D geometry like a blade, the present coupling method takes the assumption that the boundary layer growth along the spanwise direction is negligible compared to that in the chordwise direction. To take into account the three dimensional characteristics, the effects from other strips are included.

3.1 Three Dimensional Formulation

3.1.1 Edge velocity on the Body

Given a three-dimensional body such as the duct in Fig.3.1, where the duct surface is divided into N panels in the chordwise direction and the trailing edge wake is divided into N_W panels in the streamwise direction. Both the duct surface and the wake are circumferentially divided into M strips.

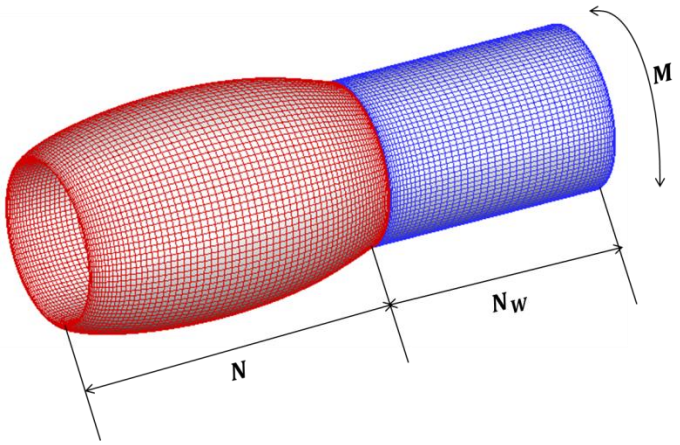

Figure 3.1 Paneling of a 3-D geometry in the viscous/inviscid interactive method

In this problem, since the interaction between different strips should be taken into consideration, the discretized equation for inviscid formulation could be written in matrix form as:

$$\begin{pmatrix} \boldsymbol{A^{11}} & \boldsymbol{A^{12}} & \cdots & \boldsymbol{A^{1M}} \\ \boldsymbol{A^{21}} & \boldsymbol{A^{22}} & \cdots & \boldsymbol{A^{2M}} \\ \vdots & \vdots & \ddots & \vdots \\ \boldsymbol{A^{M1}} & \boldsymbol{A^{M2}} & \cdots & \boldsymbol{A^{MM}} \end{pmatrix} \begin{pmatrix} \boldsymbol{\phi^{1,inv}} \\ \boldsymbol{\phi^{2,inv}} \\ \vdots \\ \boldsymbol{\phi^{M,inv}} \end{pmatrix} = \begin{pmatrix} \boldsymbol{S^{11}} & \boldsymbol{S^{12}} & \cdots & \boldsymbol{S^{1M}} \\ \boldsymbol{S^{21}} & \boldsymbol{S^{22}} & \cdots & \boldsymbol{S^{2M}} \\ \vdots & \vdots & \ddots & \vdots \\ \boldsymbol{S^{M1}} & \boldsymbol{S^{M2}} & \cdots & \boldsymbol{S^{MM}} \end{pmatrix} \begin{pmatrix} \boldsymbol{\eta^{1}} \\ \boldsymbol{\eta^{2}} \\ \vdots \\ \boldsymbol{\eta^{M}} \end{pmatrix} \tag{3.1}$$

Where $\boldsymbol{A^{PQ}}$ is a matix of size $N \times N$ which indicates the dipole influence coefficients of panels at strip Q on the control points at strip P.

$$\boldsymbol{A^{PQ}} = \left[A_{ij}^{PQ}\right] = \begin{pmatrix} A_{11}^{PQ} & A_{12}^{PQ} & \cdots & A_{1N}^{PQ} \\ A_{21}^{PQ} & A_{22}^{PQ} & \cdots & A_{2N}^{PQ} \\ \vdots & \vdots & \ddots & \vdots \\ A_{N1}^{PQ} & A_{N2}^{PQ} & \cdots & A_{NN}^{PQ} \end{pmatrix}_{N\times N} \tag{3.2}$$

A_{ij}^{PQ} is the dipole influence coefficient of panel j at strip Q on control point i of strip P.

$\boldsymbol{\phi^{Q,inv}}$ is a vector of size $N \times 1$ indicating the inviscid perturbation potential at strip Q.

$$\boldsymbol{\phi^{Q,inv}} = \left[\phi_j^{Q,inv}\right] = \begin{pmatrix} \phi_1^{Q,inv} \\ \phi_2^{Q,inv} \\ \vdots \\ \phi_N^{Q,inv} \end{pmatrix}_{N\times 1} \tag{3.3}$$

$\phi_j^{Q,inv}$ is the inviscid perturbation potential at panel j of strip Q.

$\boldsymbol{S^{PQ}}$ is a matrix of size $N \times N$ and includes the source influence coefficients of panels at strip Q on the control points at strip P.

$$\boldsymbol{S^{PQ}} = \left[S_{ij}^{PQ}\right] = \begin{pmatrix} S_{11}^{PQ} & S_{12}^{PQ} & \cdots & S_{1N}^{PQ} \\ S_{21}^{PQ} & S_{22}^{PQ} & \cdots & S_{2N}^{PQ} \\ \vdots & \vdots & \ddots & \vdots \\ S_{N1}^{PQ} & S_{N2}^{PQ} & \cdots & S_{NN}^{PQ} \end{pmatrix}_{N\times N} \tag{3.4}$$

S_{ij}^{PQ} is the source influence coefficient of panel j of strip Q on control point i of strip P.

$\boldsymbol{\eta^{Q}}$ is a vector of size $N \times 1$ including the source strength at the strip Q.

$$\boldsymbol{\eta^{Q}} = \left[\eta_j^{Q}\right] = \begin{pmatrix} \eta_1^{Q} \\ \eta_2^{Q} \\ \vdots \\ \eta_N^{Q} \end{pmatrix}_{N\times 1} \tag{3.5}$$

η_j^Q is the source strength at panel j of strip Q.

The discretized form of viscous formulation can be derived in a similar manner as used in Chapter 2, that is, by placing blowing sources of proper strength on the body surface and on the wake.

$$\begin{pmatrix} \boldsymbol{A^{11}} & \boldsymbol{A^{12}} & \cdots & \boldsymbol{A^{1M}} \\ \boldsymbol{A^{21}} & \boldsymbol{A^{22}} & \cdots & \boldsymbol{A^{2M}} \\ \vdots & \vdots & \ddots & \vdots \\ \boldsymbol{A^{M1}} & \boldsymbol{A^{M2}} & \cdots & \boldsymbol{A^{MM}} \end{pmatrix} \begin{pmatrix} \boldsymbol{\phi^{1,vis}} \\ \boldsymbol{\phi^{2,vis}} \\ \vdots \\ \boldsymbol{\phi^{M,vis}} \end{pmatrix}$$

$$= \begin{pmatrix} \boldsymbol{S^{11}} & \boldsymbol{S^{12}} & \cdots & \boldsymbol{S^{1M}} \\ \boldsymbol{S^{21}} & \boldsymbol{S^{22}} & \cdots & \boldsymbol{S^{2M}} \\ \vdots & \vdots & \ddots & \vdots \\ \boldsymbol{S^{M1}} & \boldsymbol{S^{M2}} & \cdots & \boldsymbol{S^{MM}} \end{pmatrix} \begin{pmatrix} \boldsymbol{\eta^{1}} \\ \boldsymbol{\eta^{2}} \\ \vdots \\ \boldsymbol{\eta^{M}} \end{pmatrix} \tag{3.6}$$

$$+ \begin{pmatrix} \boldsymbol{B^{11}} & \boldsymbol{B^{12}} & \cdots & \boldsymbol{B^{1M}} \\ \boldsymbol{B^{21}} & \boldsymbol{B^{22}} & \cdots & \boldsymbol{B^{2M}} \\ \vdots & \vdots & \ddots & \vdots \\ \boldsymbol{B^{M1}} & \boldsymbol{B^{M2}} & \cdots & \boldsymbol{B^{MM}} \end{pmatrix} \begin{pmatrix} \boldsymbol{\sigma^{1}} \\ \boldsymbol{\sigma^{2}} \\ \vdots \\ \boldsymbol{\sigma^{M}} \end{pmatrix}$$

Similar to $\boldsymbol{S^{PQ}}, \boldsymbol{B^{PQ}}$ is a matrix of size $N \times (N + N_W)$ and includes the blowing source influence coefficients of panels at strip Q on the control points at strip P.

$$\boldsymbol{B^{PQ}} = \left[B_{ij}^{PQ}\right] = \begin{pmatrix} B_{11}^{PQ} & B_{12}^{PQ} & \cdots & B_{1(N+N_W)}^{PQ} \\ B_{21}^{PQ} & B_{22}^{PQ} & \cdots & B_{2(N+N_W)}^{PQ} \\ \vdots & \vdots & \ddots & \vdots \\ B_{N1}^{PQ} & B_{N2}^{PQ} & \cdots & B_{N(N+N_W)}^{PQ} \end{pmatrix}_{N\times(N+N_W)} \tag{3.7}$$

B_{ij}^{PQ} is the source influence coefficient of panel j of strip Q on control point i of strip P.

$\boldsymbol{\sigma^{Q}}$ is a vector of size $(N + N_W) \times 1$ including the source strength at the strip Q.

$$\boldsymbol{\sigma^{Q}} = \left[\sigma_j^Q\right] = \begin{pmatrix} \sigma_1^Q \\ \sigma_2^Q \\ \vdots \\ \sigma_{N+N_w}^Q \end{pmatrix}_{(N+N_W)\times 1} \tag{3.8}$$

σ_j^Q is the source strength at panel j of strip Q.

By looking at Equations (32) and (37), the viscous formulation can be related to the inviscid formulation as follows:

$$\begin{pmatrix} \boldsymbol{A^{11}} & \boldsymbol{A^{12}} & \cdots & \boldsymbol{A^{1M}} \\ \boldsymbol{A^{21}} & \boldsymbol{A^{22}} & \cdots & \boldsymbol{A^{2M}} \\ \vdots & \vdots & \ddots & \vdots \\ \boldsymbol{A^{M1}} & \boldsymbol{A^{M2}} & \cdots & \boldsymbol{A^{MM}} \end{pmatrix} \begin{pmatrix} \boldsymbol{\phi^{1,vis}} \\ \boldsymbol{\phi^{2,vis}} \\ \vdots \\ \boldsymbol{\phi^{M,vis}} \end{pmatrix}$$

$$= \begin{pmatrix} \boldsymbol{A^{11}} & \boldsymbol{A^{12}} & \cdots & \boldsymbol{A^{1M}} \\ \boldsymbol{A^{21}} & \boldsymbol{A^{22}} & \cdots & \boldsymbol{A^{2M}} \\ \vdots & \vdots & \ddots & \vdots \\ \boldsymbol{A^{M1}} & \boldsymbol{A^{M2}} & \cdots & \boldsymbol{A^{MM}} \end{pmatrix} \begin{pmatrix} \boldsymbol{\phi^{1,inv}} \\ \boldsymbol{\phi^{2,inv}} \\ \vdots \\ \boldsymbol{\phi^{M,inv}} \end{pmatrix} \tag{3.9}$$

$$+ \begin{pmatrix} \boldsymbol{B^{11}} & \boldsymbol{B^{12}} & \cdots & \boldsymbol{B^{1M}} \\ \boldsymbol{B^{21}} & \boldsymbol{B^{22}} & \cdots & \boldsymbol{B^{2M}} \\ \vdots & \vdots & \ddots & \vdots \\ \boldsymbol{B^{M1}} & \boldsymbol{B^{M2}} & \cdots & \boldsymbol{B^{MM}} \end{pmatrix} \begin{pmatrix} \boldsymbol{\sigma^{1}} \\ \boldsymbol{\sigma^{2}} \\ \vdots \\ \boldsymbol{\sigma^{M}} \end{pmatrix}$$

Along a specific strip *L*, the following equations can be deduced:

$$\sum_{\boldsymbol{m=1}}^{\boldsymbol{M}} \boldsymbol{A^{Lm}}\, \boldsymbol{\phi^{m,vis}} = \sum_{\boldsymbol{m=1}}^{\boldsymbol{M}} \boldsymbol{A^{Lm}}\, \boldsymbol{\phi^{m,inv}} + \sum_{\boldsymbol{m=1}}^{\boldsymbol{M}} \boldsymbol{B^{Lm}}\, \boldsymbol{\sigma^{m}} \tag{3.10}$$

$$\boldsymbol{A^{LL}\phi^{L,vis}} = \boldsymbol{A^{LL}\phi^{L,inv}} + \sum_{\boldsymbol{m=1,m\neq L}}^{\boldsymbol{M}} \boldsymbol{A^{Lm}}\,(\boldsymbol{\phi^{m,inv}} - \boldsymbol{\phi^{m,vis}}) + \sum_{\boldsymbol{m=1}}^{\boldsymbol{M}} \boldsymbol{B^{Lm}}\, \boldsymbol{\sigma^{m}} \tag{3.11}$$

$$\begin{aligned} \boldsymbol{\phi^{L,vis}} = \boldsymbol{\phi^{L,inv}} &+ \sum_{\boldsymbol{m=1,m\neq L}}^{\boldsymbol{M}} (\boldsymbol{A^{LL}})^{-1} \boldsymbol{A^{Lm}}\,(\boldsymbol{\phi^{m,inv}} - \boldsymbol{\phi^{m,vis}}) \\ &+ \sum_{\boldsymbol{m=1}}^{\boldsymbol{M}} (\boldsymbol{A^{LL}})^{-1} \boldsymbol{B^{Lm}}\, \boldsymbol{\sigma^{m}} \end{aligned} \tag{3.12}$$

$$\begin{aligned}\boldsymbol{\phi}_{\boldsymbol{total}}^{\boldsymbol{L,vis}} &= \boldsymbol{\phi}_{\boldsymbol{in}}^{\boldsymbol{L}} + \boldsymbol{\phi}^{\boldsymbol{L,vis}} \\ &= \boldsymbol{\phi}_{\boldsymbol{in}}^{\boldsymbol{L}} + \boldsymbol{\phi}^{\boldsymbol{L,inv}} \\ &+ \sum_{\boldsymbol{m=1,m\neq L}}^{\boldsymbol{M}} (\boldsymbol{A}^{\boldsymbol{LL}})^{-\boldsymbol{1}} \boldsymbol{A}^{\boldsymbol{Lm}} (\boldsymbol{\phi}^{\boldsymbol{m,inv}} - \boldsymbol{\phi}^{\boldsymbol{m,vis}}) \\ &+ \sum_{\boldsymbol{m=1}}^{\boldsymbol{M}} (\boldsymbol{A}^{\boldsymbol{LL}})^{-\boldsymbol{1}} \boldsymbol{B}^{\boldsymbol{Lm}} \boldsymbol{\sigma}^{\boldsymbol{m}}\end{aligned} \tag{3.13}$$

Let $\boldsymbol{J}^{\boldsymbol{Lm}} = (\boldsymbol{A}^{\boldsymbol{LL}})^{-\boldsymbol{1}} \boldsymbol{A}^{\boldsymbol{Lm}}, \boldsymbol{H}^{\boldsymbol{Lm}} = (\boldsymbol{A}^{\boldsymbol{LL}})^{-\boldsymbol{1}} \boldsymbol{B}^{\boldsymbol{Lm}}$, we then have

$$\begin{aligned}\boldsymbol{\phi}_{\boldsymbol{total}}^{\boldsymbol{L,vis}} = \boldsymbol{\phi}_{\boldsymbol{in}}^{\boldsymbol{L}} + \boldsymbol{\phi}^{\boldsymbol{L,inv}} + \sum_{\boldsymbol{m=1,m\neq L}}^{\boldsymbol{M}} \boldsymbol{J}^{\boldsymbol{Lm}} (\boldsymbol{\phi}^{\boldsymbol{m,inv}} - \boldsymbol{\phi}^{\boldsymbol{m,vis}}) \\ + \sum_{\boldsymbol{m=1}}^{\boldsymbol{M}} \boldsymbol{H}^{\boldsymbol{Lm}} \boldsymbol{\sigma}^{\boldsymbol{m}}\end{aligned} \tag{3.14}$$

The term $\sum_{\boldsymbol{m=1,m\neq L}}^{\boldsymbol{M}} \boldsymbol{J}^{\boldsymbol{Lm}} (\boldsymbol{\phi}^{\boldsymbol{m,inv}} - \boldsymbol{\phi}^{\boldsymbol{m,vis}})$ stands for the effects of interaction between strips. It can be seen that the viscous total potential can be obtained by adding the induced potential by the blowing sources and the interaction term of viscous potential between strips to the inviscid total potential. Differentiating the viscous total potential along the streamwise direction of the body will give the viscous velocity or edge velocity.

$$\begin{aligned}\boldsymbol{U}^{\boldsymbol{L,vis}} = \boldsymbol{U}^{\boldsymbol{L,inv}} + \sum_{\boldsymbol{m=1,m\neq L}}^{\boldsymbol{M}} \boldsymbol{D}^{\boldsymbol{L}} \boldsymbol{J}^{\boldsymbol{Lm}} (\boldsymbol{\phi}^{\boldsymbol{m,inv}} - \boldsymbol{\phi}^{\boldsymbol{m,vis}}) \\ + \sum_{\boldsymbol{m=1}}^{\boldsymbol{M}} \boldsymbol{D}^{\boldsymbol{L}} \boldsymbol{H}^{\boldsymbol{Lm}} \boldsymbol{\sigma}^{\boldsymbol{m}}\end{aligned} \tag{3.15}$$

Where $\boldsymbol{D^L}$ represents the differentiation matrix along the streamwise direction of strip *L*.

Let $\boldsymbol{C^{Lm} = D^L J^{Lm}, K^{Lm} = D^L H^{Lm}}$

$$\boldsymbol{U^{L,vis} = U^{L,inv} + \sum_{m=1,m\neq L}^{M} K^{Lm}\left(\phi^{m,inv} - \phi^{m,vis}\right) + \sum_{m=1}^{M} C^{Lm}\sigma^{m}} \tag{3.16}$$

The viscous potential on the wake can be obtained by summing the induced potential by the source and dipole on the body, the dipole on the wake and the blowing source on the boy as well as wake

3.1.2 Edge velocity on the wake

The viscous perturbation potential on the trailing edge wake is induced by the dipoles and sources on the body, the blowing sources on the body and wake, which, for a wake strip *L*, can be expressed as:

$$\boldsymbol{\phi_w^{L,vis} = \sum_{m=1}^{M} A_w^{Lm}\phi^{m,vis} + \sum_{m=1}^{M} S_w^{Lm}\eta^{m} + \sum_{m=1}^{M} B_w^{Lm}\sigma^{m}} \tag{3.17}$$

In addition, the total viscous potential on the wake strip L is expressed as

$$\begin{aligned}\boldsymbol{\phi}_{\boldsymbol{w,total}}^{\boldsymbol{L,vis}} &= \boldsymbol{\phi}_{\boldsymbol{w,in}}^{\boldsymbol{L}} + \boldsymbol{\phi}_{\boldsymbol{w}}^{\boldsymbol{L,vis}} \\ &= \boldsymbol{\phi}_{\boldsymbol{w,in}}^{\boldsymbol{L}} + \sum_{m=1}^{M} \boldsymbol{A}_{\boldsymbol{w}}^{\boldsymbol{Lm}} \boldsymbol{\phi}^{\boldsymbol{m,vis}} \\ &+ \sum_{m=1}^{M} \boldsymbol{S}_{\boldsymbol{w}}^{\boldsymbol{Lm}} \boldsymbol{\eta}^{\mathbf{m}} + \sum_{m=1}^{M} \boldsymbol{B}_{\boldsymbol{w}}^{\boldsymbol{Lm}} \boldsymbol{\sigma}^{\boldsymbol{m}}\end{aligned} \tag{3.18}$$

Accordingly the edge velocity on the wake can be expressed as the differentiation of the total viscous potential in the streamwise direction:

$$\begin{aligned}\boldsymbol{U}_{\boldsymbol{w}}^{\boldsymbol{L,vis}} &= \boldsymbol{U}_{\boldsymbol{w,in}}^{\boldsymbol{L}} + \sum_{m=1}^{M} \boldsymbol{D}^{\boldsymbol{L}} \boldsymbol{A}_{\boldsymbol{w}}^{\boldsymbol{Lm}} \boldsymbol{\phi}^{\boldsymbol{m,vis}} \\ &+ \sum_{m=1}^{M} \boldsymbol{D}^{\boldsymbol{L}} \boldsymbol{S}_{\boldsymbol{w}}^{\boldsymbol{Lm}} \boldsymbol{\eta}^{\mathbf{m}} + \sum_{m=1}^{M} \boldsymbol{D}^{\boldsymbol{L}} \boldsymbol{B}_{\boldsymbol{w}}^{\boldsymbol{Lm}} \boldsymbol{\sigma}^{\boldsymbol{m}}\end{aligned} \tag{3.19}$$

By substituting Equation (43) into (50), we can have

$$\begin{aligned}\boldsymbol{U}_{\boldsymbol{w}}^{\boldsymbol{L,vis}} = \boldsymbol{U}_{\boldsymbol{w,in}}^{\boldsymbol{L}} &+ \sum_{m=1}^{M} \boldsymbol{D}^{\boldsymbol{L}} \boldsymbol{A}_{\boldsymbol{w}}^{\boldsymbol{Lm}} \left[\boldsymbol{\phi}^{\boldsymbol{m,inv}} + \sum_{\boldsymbol{l=1, l\neq m}}^{\boldsymbol{M}} \left(\boldsymbol{A}^{\boldsymbol{ll}}\right)^{\boldsymbol{-1}} \boldsymbol{A}^{\boldsymbol{ml}} \left(\boldsymbol{\phi}^{\boldsymbol{l,inv}} \right.\right. \\ &\left.\left. - \boldsymbol{\phi}^{\boldsymbol{l,vis}}\right) + \sum_{\boldsymbol{l=1}}^{\boldsymbol{M}} (\boldsymbol{A}^{\boldsymbol{mm}})^{\boldsymbol{-1}} \boldsymbol{B}^{\boldsymbol{ml}} \boldsymbol{\sigma}^{\boldsymbol{l}} \right] + \sum_{m=1}^{M} \boldsymbol{D}^{\boldsymbol{L}} \boldsymbol{S}_{\boldsymbol{w}}^{\boldsymbol{Lm}} \boldsymbol{\eta}^{\mathbf{m}} \\ &+ \sum_{m=1}^{M} \boldsymbol{D}^{\boldsymbol{L}} \boldsymbol{B}_{\boldsymbol{w}}^{\boldsymbol{Lm}} \boldsymbol{\sigma}^{\boldsymbol{m}}\end{aligned} \tag{3.20}$$

3.2 Coupling Procedure

Unlike the coupling procedure in the 2-D problem which is quite straightforward, the coupling algorithm is performed in an iterative manner because of the interactive effects between different strips.

The iterative algorithm is introduced in details as following:

STEP 1: solve for the inviscid velocity as the initial guess of the edge velocity.

STEP 2: calculate the displacement thickness δ^* from the edge velocity distribution on each strip through the two dimensional boundary solver equations.

STEP 3: calculate the blowing source strength σ with the edge velocity and displacement thickness on each strip.

STEP 4: update the edge velocity with the calculated blow source strength.

STEP 5: go to STEP 6 if the converged solution is achieved at each strip. Otherwise go back to STEP 2.

STEP 6: update the viscous potential on the body and wake at all strips.

STEP 7: update the edge velocity at all strips by taking into account the interaction terms between strips and bodies.

STEP 8: continue to STEP 9 if a convergence of edge velocity is obtained. Otherwise return to STEP 1 for new iterations.

STEP 9: save the solutions and exit the iteration process.

Chapter 4 Wake Alignment Scheme

The free vortex sheets shedding from the trailing edge of a propeller blade are material surfaces, which have to be aligned with the local flow velocity. A lot of researches have been carried out on the alignment scheme of the trailing wake sheet since a reasonable representation of the wake is of crucial significance for the calculation of induced velocities on the blade surface and hence the overall loading on the propeller.

In this chapter, the full wake alignment scheme presented by Tian and Kinnas (2012) is improved by taking into account the additional effects of singularities on the duct as well as the duct wake. The basic algorithm of the scheme will be introduced. Since the wake geometry continues to be updated in this scheme, it is important to repanel the duct, which will also be addressed. After that the reliability of the full wake alignment model will firstly be validated through the case of a bare duct subjected to uniform inflow. Correlation of flow velocity would be made at several selected field points between the lower order panel method and axisymmetric RANS simulations. It should be noted that the effects of viscosity is not included at this stage.

The improved wake alignment scheme is then applied into two more challenging cases: a ducted propeller with round blade tip and a ducted propeller with square blade tip. In these two cases, the panel method with two different wake models: PSF-2 type scheme and the improved full wake alignment scheme would be correlated with experimental measurements, a VLM/RANS coupling method to be introduced later in this chapter and full blown RANS simulations conducted in commercial CFD packages.

4.1 PSF-2 Type Alignment Scheme

The PSF-2 wake model was originally developed by Kerwin (1981) and then extended by Greeley et al. (1982). In this model the trailing vortex wake is composed by the parts of a transition wake and an ultimate wake. The detailed procedure of PSF-2 alignment is presented as follows.

At the first step, the trailing vortex lines at the most inner and outer end of the transition region are aligned with the computed flow. The trailing vortex lines in between are determined through interpolation. The axial and tangential locations of the vortex lines are computed with the induced velocity by the propeller. On the other hand, the radial location of the vortex lines is dependent on the contraction of the transition wake at the tip and the radius of the ultimate wake and the roll-up of the wake is suppressed. The ultimate wake pitch is calculated by the method by Loukakis (1971) where the ultimate wake is assumed to extend infinitely upstream and downstream.

4.2 Full Wake Alignment

4.2.1 Basic Algorithm

A summary of the work on full wake alignment model of Tian and Kinnas (2012) will be presented in this part. In the model of full wake alignment, the corner points of the wake panels are aligned with the local flow velocity. Consider a field point under cylindrical coordinate system with x_{i-1}, θ_{i-1} and r_{i-1} being its axial, tangential and

radial coordinates and let $\Delta\theta$ be the parameter related to grid size in the streamwise direction and hence the size of time step for iteration.

By aligning the wake with the inflow, the coordinate of the consequent point can be calculated as:

$$\begin{aligned} x_i &= x_{i-1} + \frac{RJ_s\Delta\theta}{\pi} \\ r_i &= r_{i-1} \\ \theta_i &= \theta_{i-1} + \Delta\theta \end{aligned} \tag{32}$$

Where R is the radius of the propeller, J_s is the advance ratio of the propeller.

In the local Cartesian system on the segment relating the $(i-1)$th and the consequent ith point, the direction of the effective inflow can be derived as:

$$\boldsymbol{s}_i = \frac{\Delta \boldsymbol{s}_i}{|\Delta \boldsymbol{s}_i|} \tag{33}$$

Where $\Delta\boldsymbol{s_i}$ is the segment between the $(i-1)$th and ith point. It can be expressed in the local Cartesian system as:

$$\Delta \boldsymbol{s_i} = \begin{pmatrix} RJ_s\Delta\theta/\pi \\ r_{i-1}[\cos(\theta_{i-1}+\Delta\theta) - \cos\theta_{i-1}] \\ r_{i-1}[\sin(\theta_{i-1}+\Delta\theta) - \sin\theta_{i-1}] \end{pmatrix} \tag{34}$$

Let the averaged perturbation velocity expressed as

$$\widehat{\boldsymbol{u}}_i = \frac{1}{2}(\boldsymbol{u}_i + \boldsymbol{u}_{i+1}) \tag{35}$$

It can be decomposed into two velocity components: the velocity component along segment $\hat{u}_{i,s}$ and the velocity component normal to the segment $\hat{u}_{i,n}$.

$$\hat{u}_{i,s} = \hat{\boldsymbol{u}}_i \cdot \boldsymbol{s}_i$$
$$\hat{u}_{i,n} = \hat{\boldsymbol{u}}_i - \hat{u}_{i,s} \cdot \boldsymbol{s}_i \tag{36}$$

By defining $\Delta t^* = |\Delta \boldsymbol{s}_i|/(\hat{u}_{i,s}\Delta\theta/\omega_{prop} + |\boldsymbol{s}_i|)$ and $\beta = \Delta t/\Delta t^*$ we can finally derive the algorithm for full wake alignment in the problem of marine propellers.

$$\begin{aligned} \boldsymbol{x}_i^{n+1} &= \hat{\boldsymbol{u}}_{i,n}\Delta t + \left(1 - \frac{\Delta t}{\Delta t_i^*}\right)\boldsymbol{x}_i^n + \frac{\Delta t}{\Delta t_i^*}(\boldsymbol{x}_{i-1}^n + \Delta \boldsymbol{s}_i) \\ &= \beta \hat{\boldsymbol{u}}_{i,n}\Delta t_i^* + (1-\beta)\boldsymbol{x}_i^n + \beta(\boldsymbol{x}_{i-1}^n + \Delta \boldsymbol{s}_i) \end{aligned} \tag{37}$$

Where $\boldsymbol{x}_i^n$ stands for the coordinate of the ith point at the nth time step

In the problem of steady analysis, the alignment scheme continues updating the geometry of the wake without solving for the perturbation potential until the criterion of convergence is met or the maximum number of iterations is reached. The dipole influence coefficients by the trailing wake are then reevaluated. If the repaneling of duct, as will be introduced shortly, is involved, the source and dipole influence coefficients by the duct also need to be recomputed. Once the reevaluation of the influence coefficient is finished, the perturbation potentials on the blades, the duct and the wake are solved for. This process will continue until the convergence of wake shape and force performance, normally thrust and torque is achieved.

4.2.2 Repaneling of the Duct

In the improved full wake alignment scheme, the wake geometry is updated within each iteration. The procedure of repaneling the duct is to ensure that the duct panel

is aligned with the updated wake after a converged wake shape is achieved at each iteration. As aforementioned, besides the influence coefficients due to the wake, the influence coefficients due to the duct need also to be reevaluated because of the duct repaneling procedure.

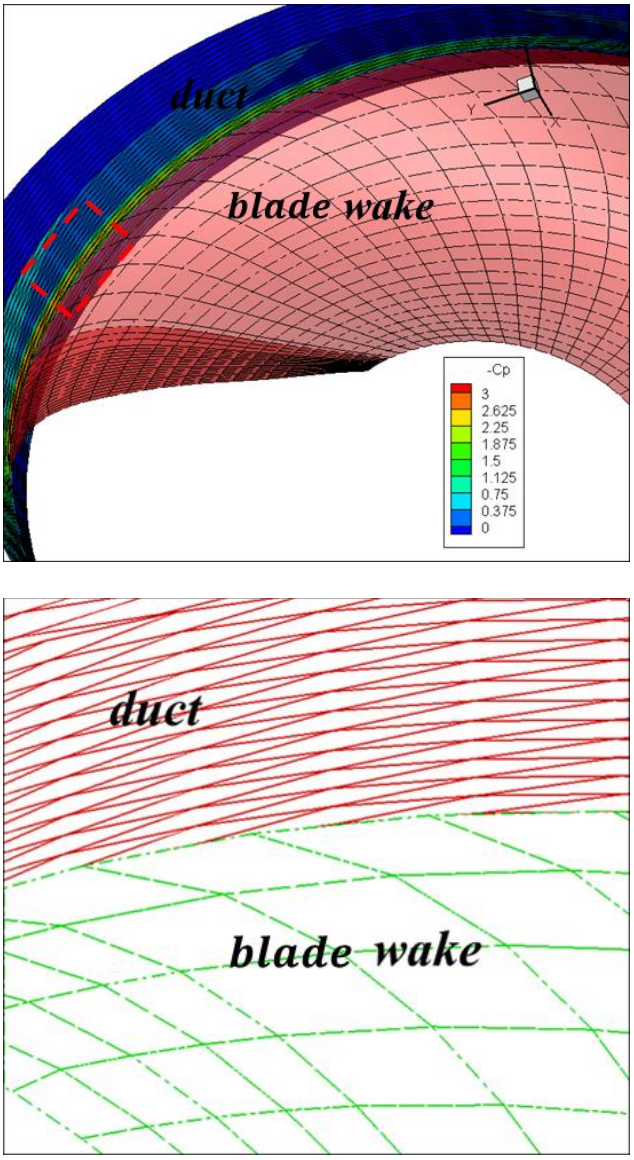

Figure 4.1 Global (upper) and local (lower) view of the repaneling of duct in the procedure of full wake alignment. The blade wake is at the same pitch with the duct panels, but the panel nodes do not match.

Further improvement related to duct repaneling can be achieved by collapsing the duct panel nodes with the nodes along the blade wake tips, as can be observed in Figure 4.2. It may further help to improve that efficiency of the present panel method, especially in terms of stability of results.

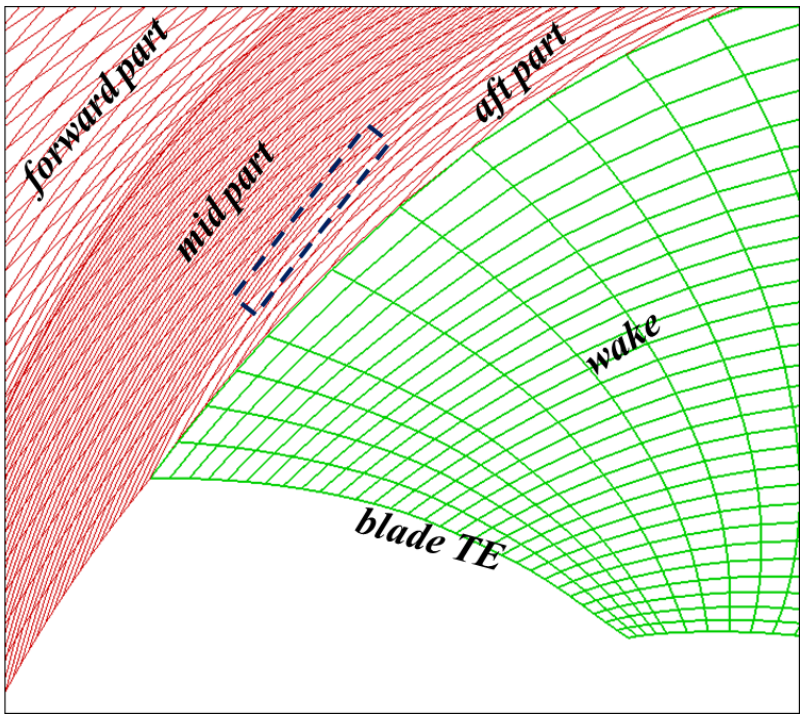

Figure 4.2 Demonstration of collapsing the duct panel nodes with the nodes along the blade wake tips. Note that the panel nodes on the duct and blade wake match.

This procedure, however, requires some more careful treatments. Firstly, the paneling in the mid part of the duct normally needs to follow the blade panel distribution in which cosine spacing is usually applied for better resolution of the blade leading edge and trailing edge. Thus there will be an abrupt transition of panel size from the last panel of the mid part to the first panel to the aft part of the duct. Besides since the panel size in the aft part of the duct is largely decided by the blade wake, there might be panels of

large size near the trailing edge of the duct, causing some problem of satisfying the iterative Kutta condition within the present panel method.

4.2.3 Treatment of Panel Penetration

In the improved full wake alignment scheme, the radial component of the local velocity within the wake is not constrained to zero for more physical representation of the wake geometry. However in some cases this might lead to the penetration of the wake panels on the pressure side or even the suction side of the duct, resulting into unrealistic results and crashing of the code. To avoid this situation, the part of the wake which penetrates the duct is cut off with the duct inner surface through cubic spline interpolation along the duct inner surface. Further interpolation is required to reallocate the locations of the corner points of the wake panels.

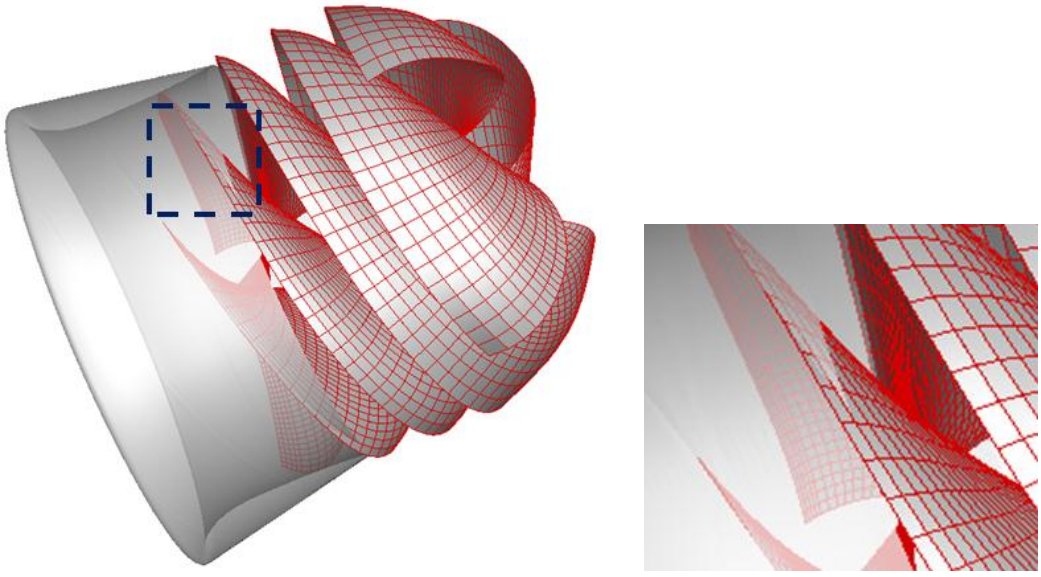

Figure 4.3 Penetration of wake panels on the duct inner surface even the outer surface at some locations

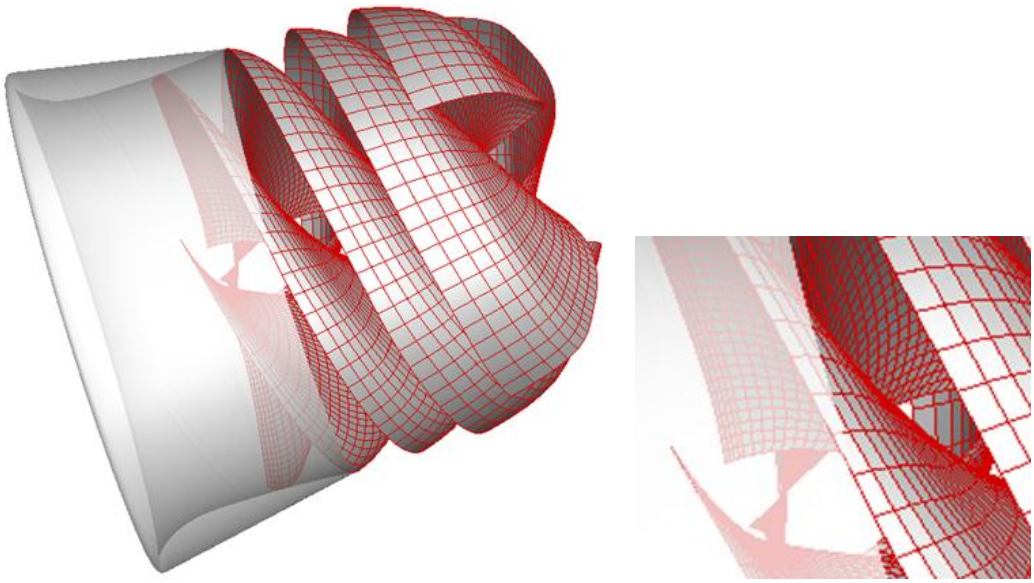

Figure 4.4 The paneling of the wake after resolving the problem of panel penetration

4.3 Flow Field inside the Duct

Before applying the improved full wake alignment scheme to more complicated problems, it is important to ensure that the evaluation of additional effects of the singularities on the duct and its trailing wake is correctly added into the scheme. The validation is carried out in the problem of a bare duct subjected to uniform inflow as shown in Figure 4.5. The duct shape was adjusted to avoid separation when operating without the propeller. The flow velocity induced by the duct is evaluated at points with fixed axial coordinate but different radial coordinates.

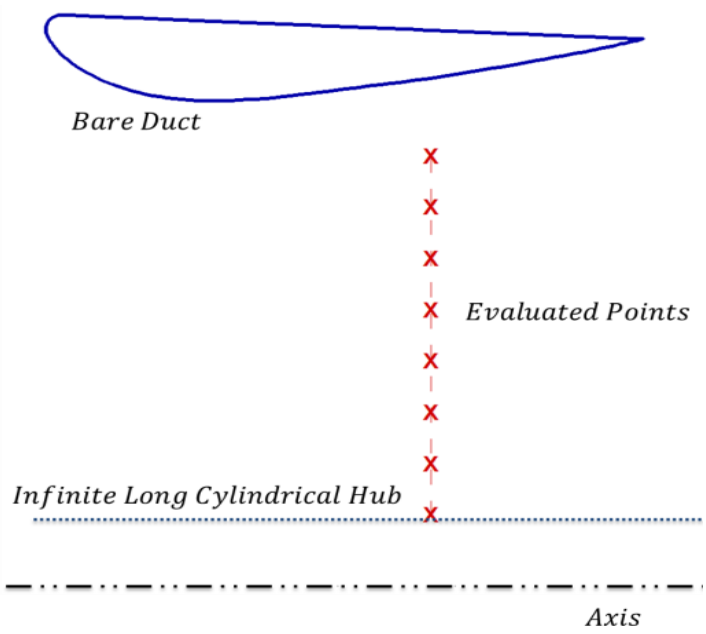

Figure 4.5 Demonstration of the problem of a bare duct subjected to uniform inflow and the points selected for evaluation

The velocity computed by the present panel method at the space points shown in Figure 4.5 are correlated with that from RANS axisymmetric simulation. It should be noted that the effects of viscosity is involved in the RANS simulation, while it is not in the panel method. Good correlation has been observed at different locations.

On the other hand, it is also important to ensure that the panel method with full wake alignment is grid independent. In Figure 4.7, the calculated velocity at the selected points by the panel method with different panel numbers is shown. The number of chordwise panels is varied while the number of circumferential panels is maintained the same. As expected, the results from different paneling conditions collapse into each other and it is convincing that the improved full wake alignment can be applied to more challenging cases such as ducted propellers.

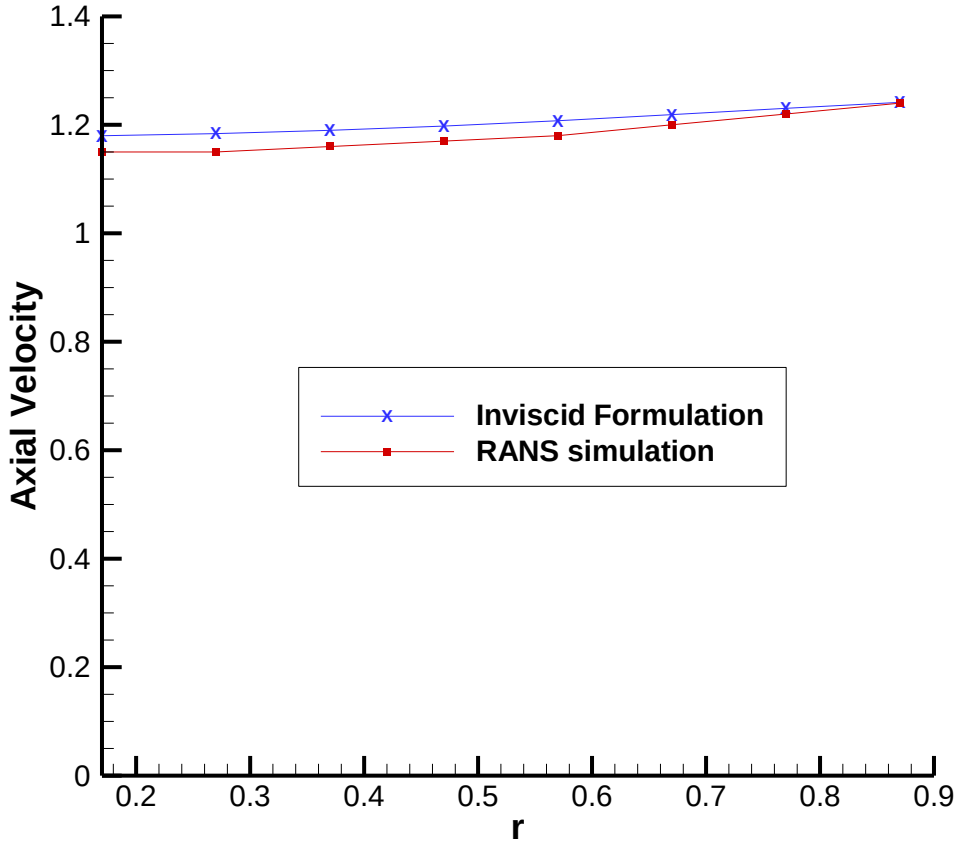

Figure 4.6 The correlation of the axial velocity of the flow at selected points between panel method and RANS axisymmetric Simulation

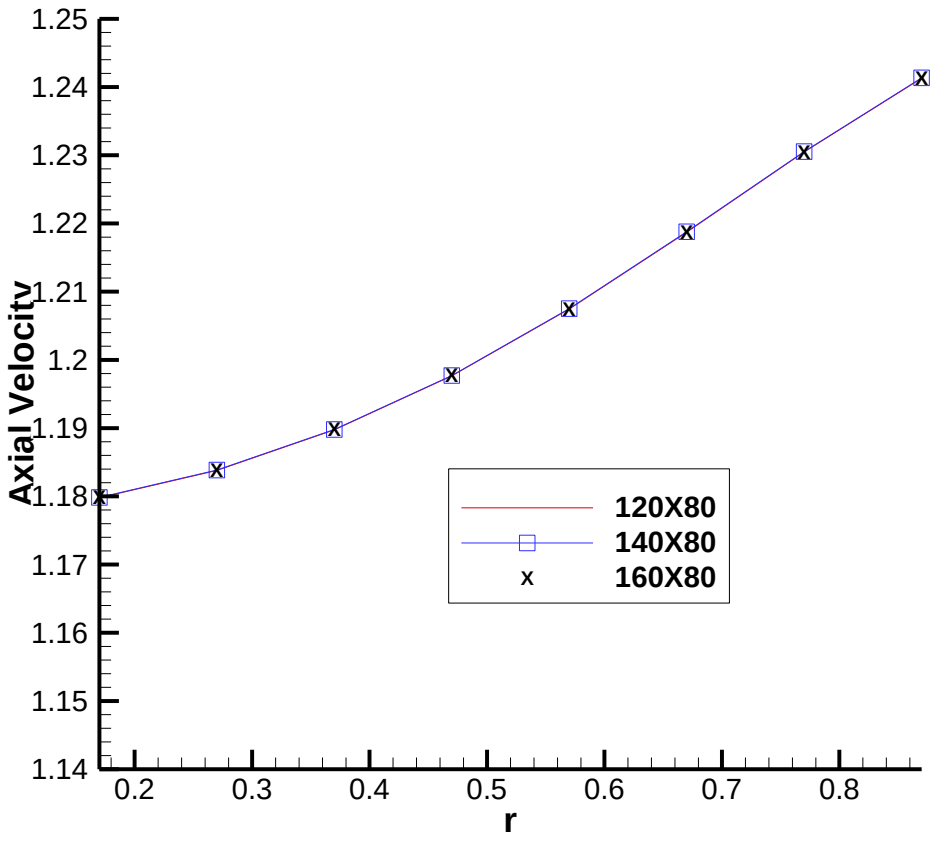

Figure 4.7 Convergence study on the panel method with respect to the evaluated axial velocity

4.4 Ducted Propeller with Round Blade Tip and Sharp Trailing Edge Duct

In this part, the present lower order panel method would be applied to the case of ducted propeller with round blade tip and a sharp trailing edge duct. Two different wake alignment models will be involved: PSF-2 type wake model and full wake alignment scheme which has already been introduced in details.

At the same time, a hybrid method developed by the Ocean Engineering Group that couples an axisymmetric swirl RANS solver with a potential flow solver applied for the same case. In addition, full blown RANS simulations will be performed with sufficient spatial resolution in ANSYS Fluent and Star-CCM+.

The overall force performance predicted by the lower order panel method will be correlated with that from the RANS/VLM coupling method, the full blown RANS simulation as well as experimental data. Furthermore, the pressure distribution on the blade and duct surface is of equal significance and detailed correlations will be carried out among these methods.

The geometry of the ducted propeller and the 2-D section of its duct are indicated in Figure 4.8. It is a 4 bladed propeller with round blade tip and bounded within a sharp trailing edge duct. The design advance ratio J_s of this propeller is around 0.40. A 0.5%Rgap between the blade tip and the duct inner surface is in presence.

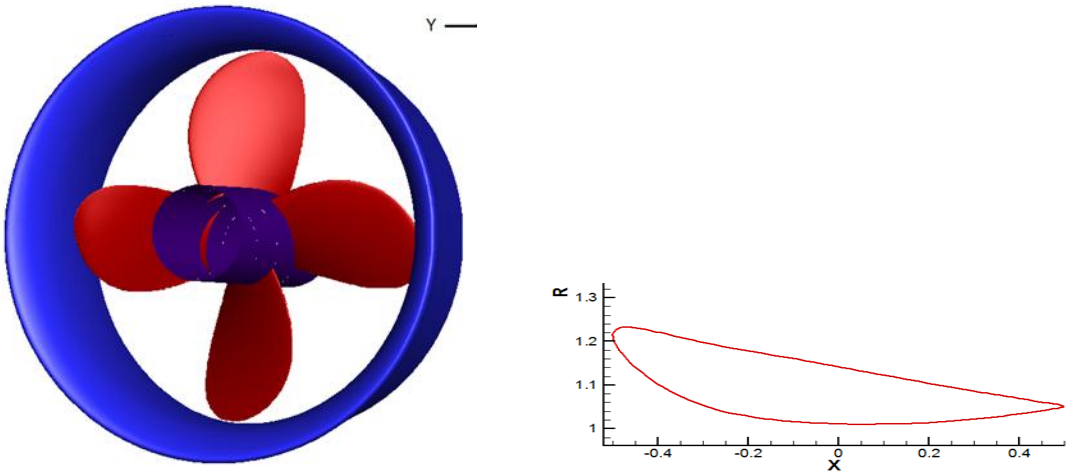

Figure 4.8 The three dimensional geometry of the round tip ducted propeller and the two dimensional section of the sharp trailing edge duct

4.4.1 Lower Order Panel Method

For the lower order panel method, 80×20 (chordwise×spanwise) and 200×80 (chordwise×circumferential) panels are used to respectively represent the blade and duct surface. Two wake models, PSF-2 wake model and full wake alignment (FWA) scheme, are adopted. For all advance ratios, PSF-2 scheme trimmed the blade wakes at 2R downstream with an ultimate wake disk, while the full wake alignment scheme models blades wakes of one revolution. It respectively takes about 30 minutes and 3 minutes for full wake alignment and PSF-2 wake model to complete the run on a single core of Intel Xeon 2.54 GHz CPU. The wake geometry generated by the two models at J_s =0.3, 0.4 and 0.5 are shown in Figure 4.9- Figure 4.14.

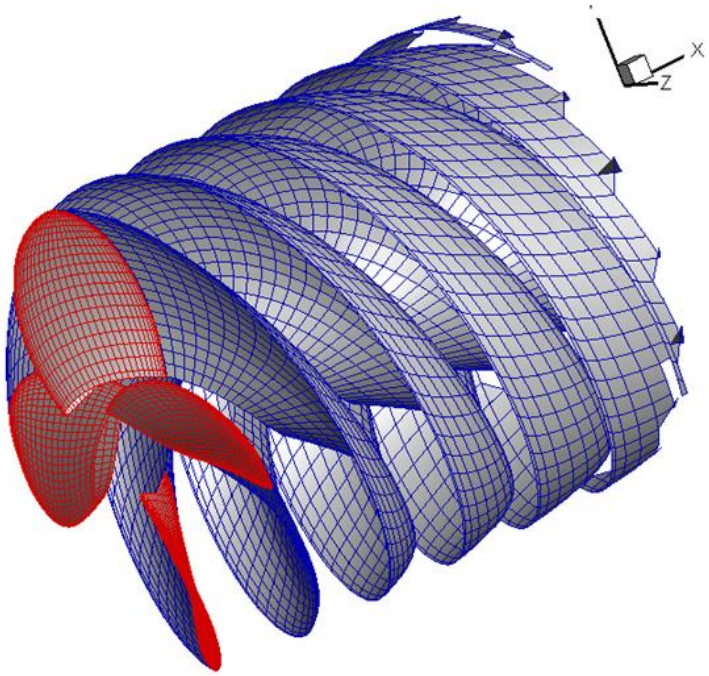

Figure 4.9 Wake geometry generated from PSF-2 wake model at J_s=0.30

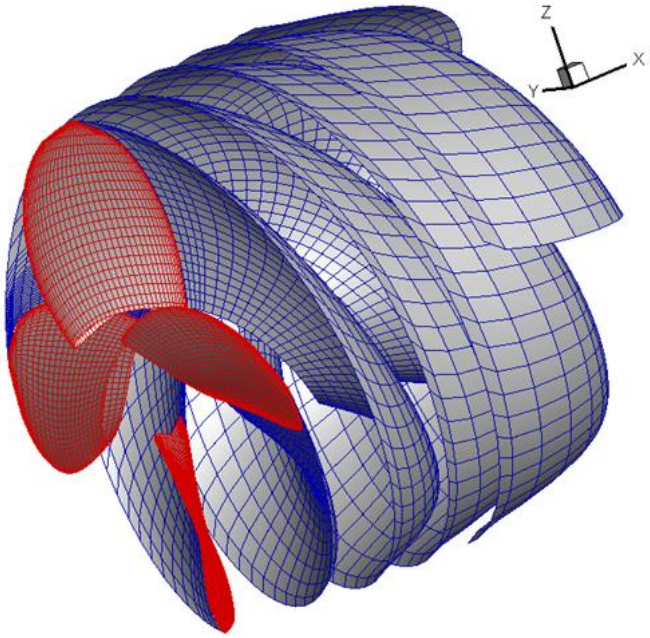

Figure 4.10 Wake geometry generated from full wake alignment scheme at J_s=0.30

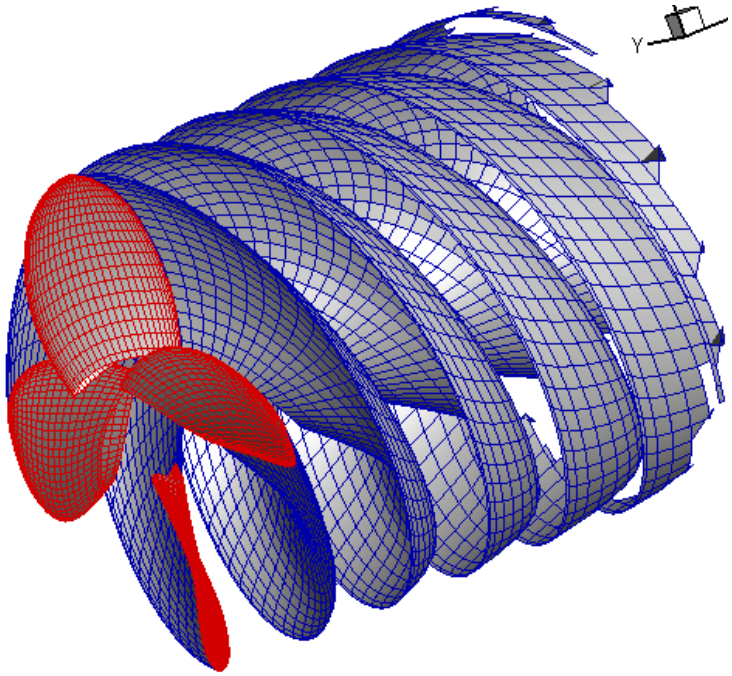

Figure 4.11 Wake geometry generated from PSF-2 wake model at J_s=0.40

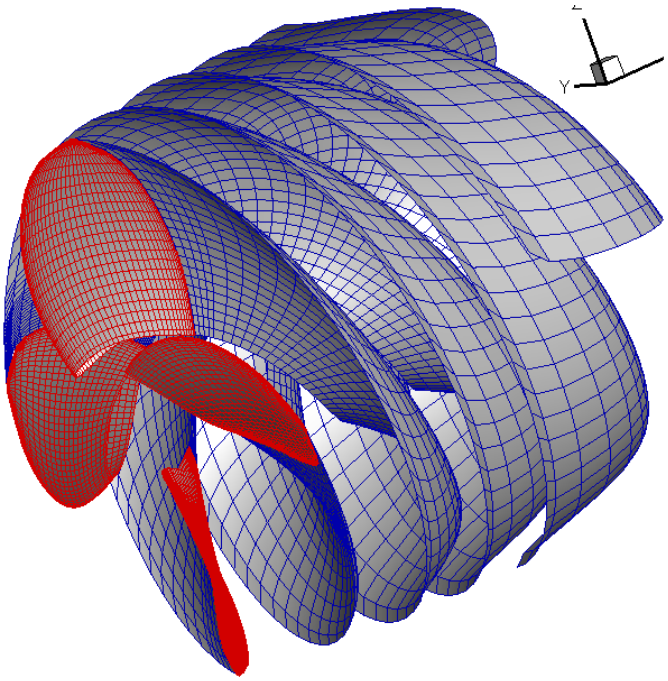

Figure 4.12 Wake geometry generated from full wake alignment scheme at J_s=0.40

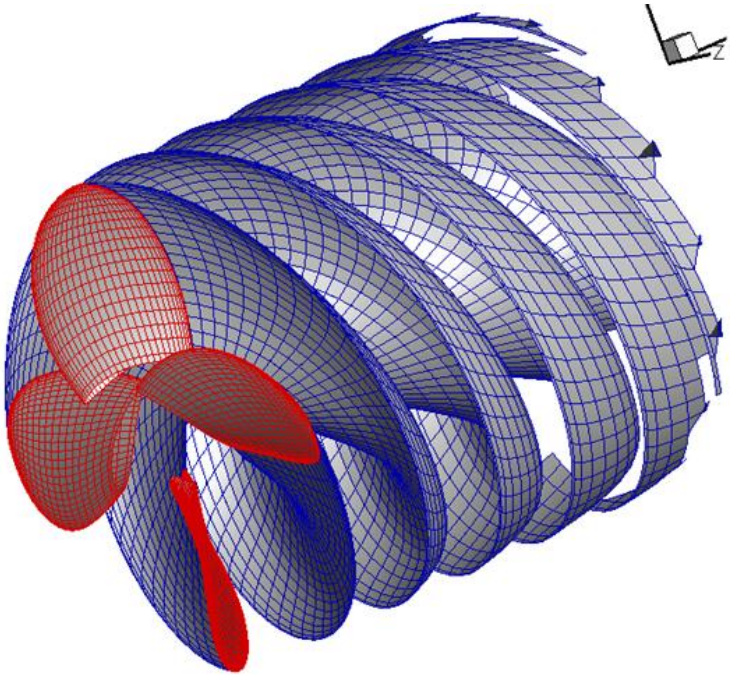

Figure 4.13 Wake geometry generated from PSF-2 wake model at J_s=0.50

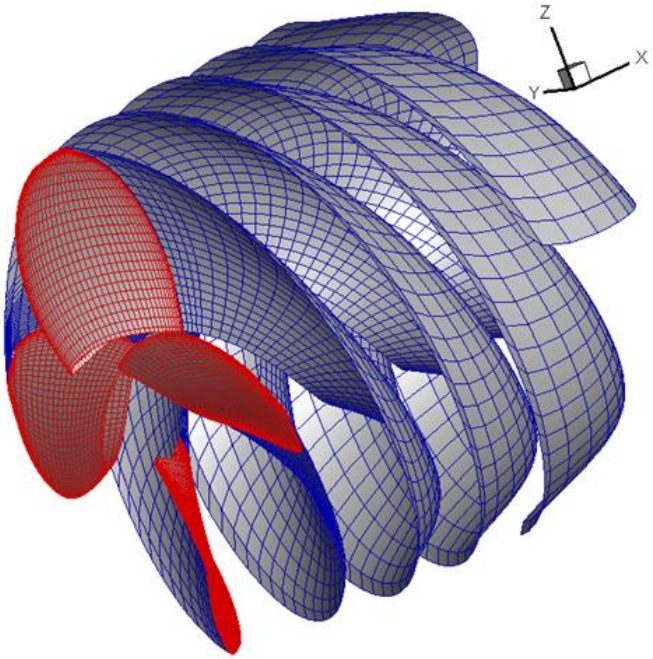

Figure 4.14 Wake geometry generated from full wake alignment scheme at J_s=0.50

Clearly at low advance ratios, the characteristics of roll-up can be observed from the wake sheet generated by the full wake alignment scheme. On the other hand, PSF-2 wake model does not predict the contraction of the transition wake radius. The contraction rate of the transition wake is a user input parameter in PSF-2 alignment model and it is set to zero since this parameter differs from case to case.

As will be seen shortly in the figure of force comparison, at low advance ratios, whether contraction of the wake radius has been correctly predicted (Full Wake Alignment) or not (PSF-2 type scheme) will significantly affect the predicted total performance of the propeller.

4.4.2 RANS/VLM Coupling Method

The RANS-VLM coupling method, developed by the Ocean Engineering Group at the University of Texas at Austin, couples a potential flow based vortex-lattice method (VLM) with an axisymmetric-swirl RANS solver. The iterative algorithm of the coupling method is as follows. As the first step, the VLM solver is executed to produce the data of pressure and area within the flow field, which is then used for calculation of time-averaged body force. The body force is added as source term into the momentum equation of the axisymmetric-swirl RANS solver. The gridding in the RANS solver is usually much denser than that in the VLM solver. A robust scheme has been developed by Kinnas et al (2012) for the interpolation of body force when imported into the RANS simulation.

A propeller induced velocity is calculated by the VLM solver at the first step and a total velocity is subsequently extracted from the RANS simulation. Afterwards an effective wake is calculated by subtracting then propeller induced velocity from the total velocity. This effective wake is then used as the inflow for the next iteration. The iterations continue until convergence of force performance is achieved.

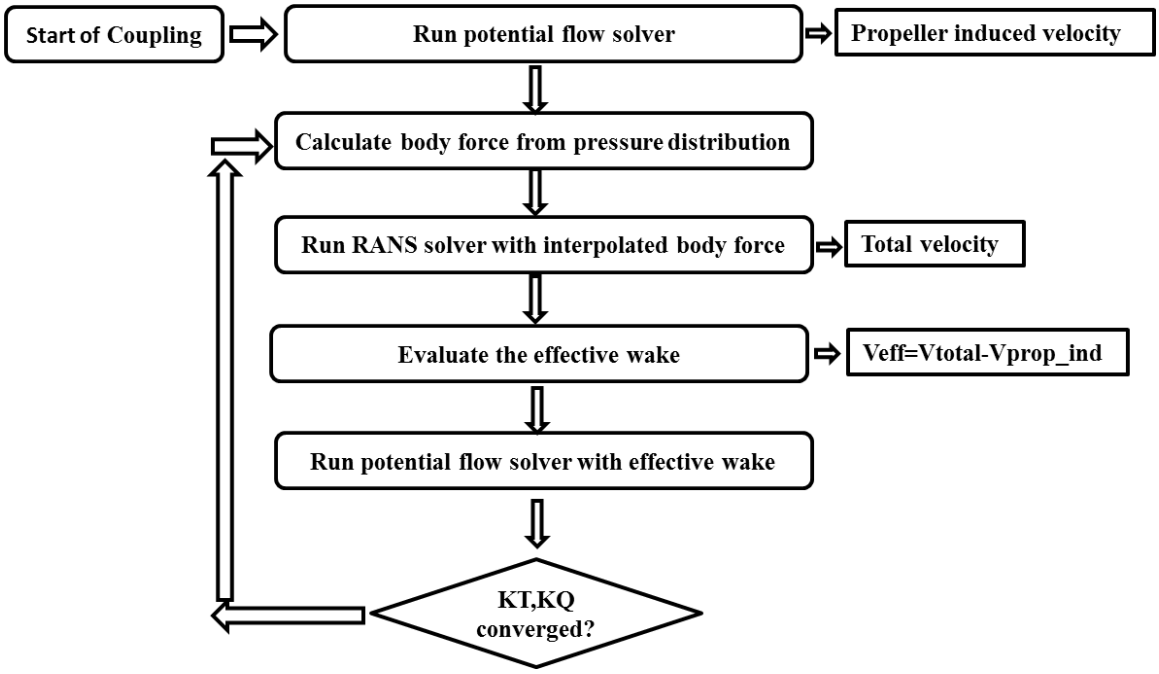

Figure 4.15 Flowchart for the iterative RANS-VLM coupling method

Shown in Figure 4.16 is the geometry and gridding of ducted propeller in the potential flow solver. Image model has been adopted for the duct and the inner surface of the duct is only used for analysis. 20×18 (chordwise $\times$ spanwise) panels is used to represent the key blade. The other blades have the same paneling as that on the key blade.

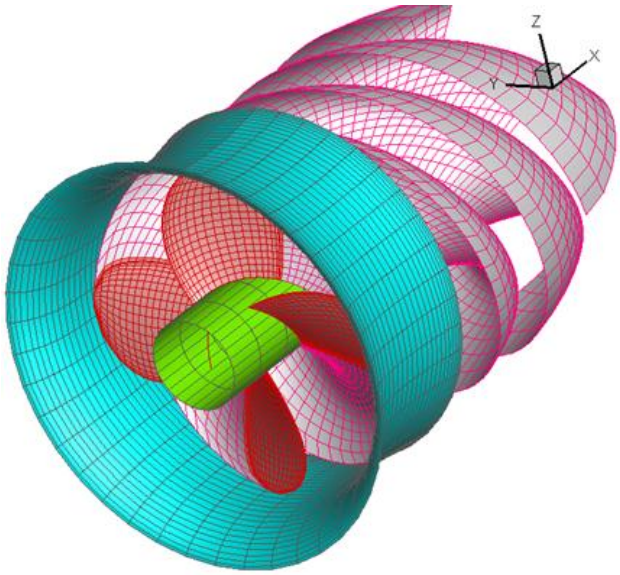

Figure 4.16 Geometry and paneling of the ducted propeller in potential flow solver

Figure 4.17 shows the axial component of the effective wake UXE from the final iteration. Since the inflow velocity far upstream is 1.0m/s, it can be clearly observed the inflow is accelerated by the duct.

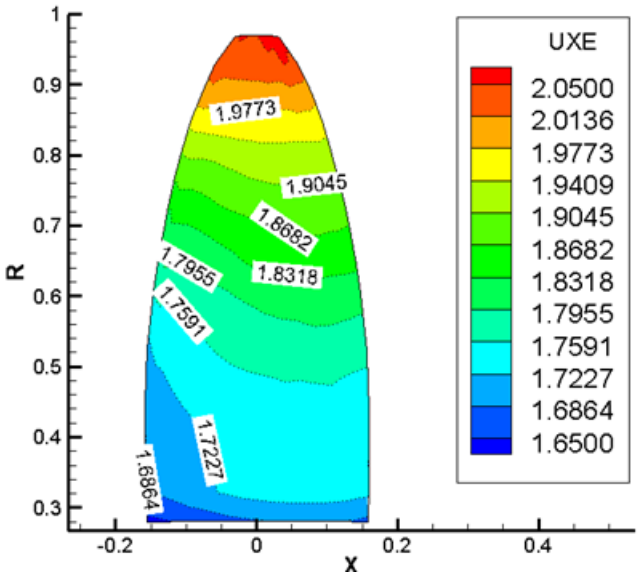

Figure 4.17 Contour of the axial component of the effective wake at final iteration

The body force calculated with the data of areas and pressures from the potential flow solver is added into the momentum equation as a source term. To ensure an accurate interpolation of body force in RANS solver, the gridding in the RANS solver is generally much denser than that in the potential flow solver.

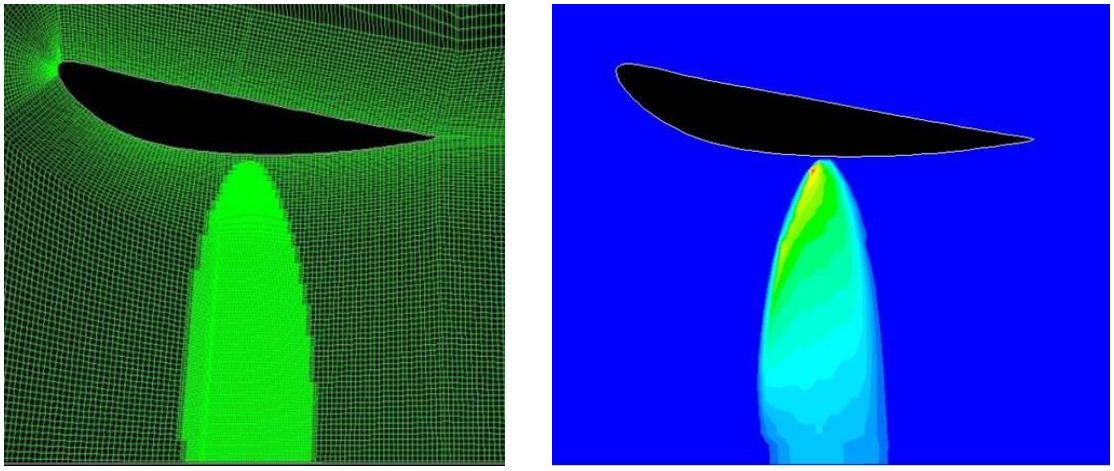

Figure 4.18 Gridding and the interpolated body force in the RANS solver

4.4.3 Full Blown RANS simulation

The full blown RANS simulation are performed within ANSYS Fluent as well as Star-CCM+ in which periodic interfaces have been applied such that for the present propeller only a quarter of the whole fluid domain is necessary for further simulation. In addition, to better resolve the boundary layer structures on the blades and duct, structured meshing model has been adopted. The same gridding model has been used for the trailing wake of the blades and duct in order to reduce the possible artificial diffusivity. Shown in Figure 4.19 is the fluid domain as well as the boundary conditions used in Star-CCM+.

Figure 4.20 presents the gridding on the duct and blade and a good resolution of the leading edges of the blades and duct can be well identified.

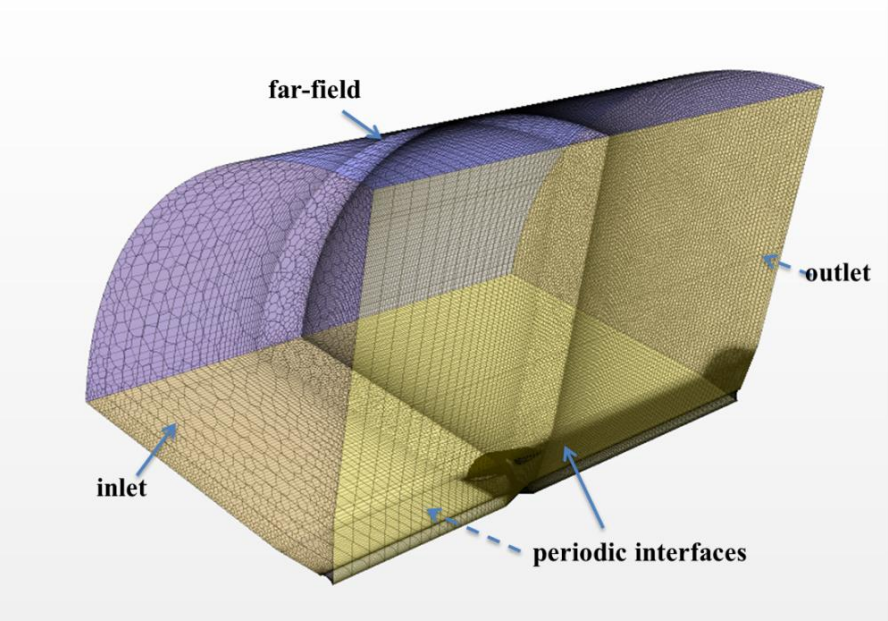

Figure 4.19 The fluid domain and boundary conditions used in the RANS simulation

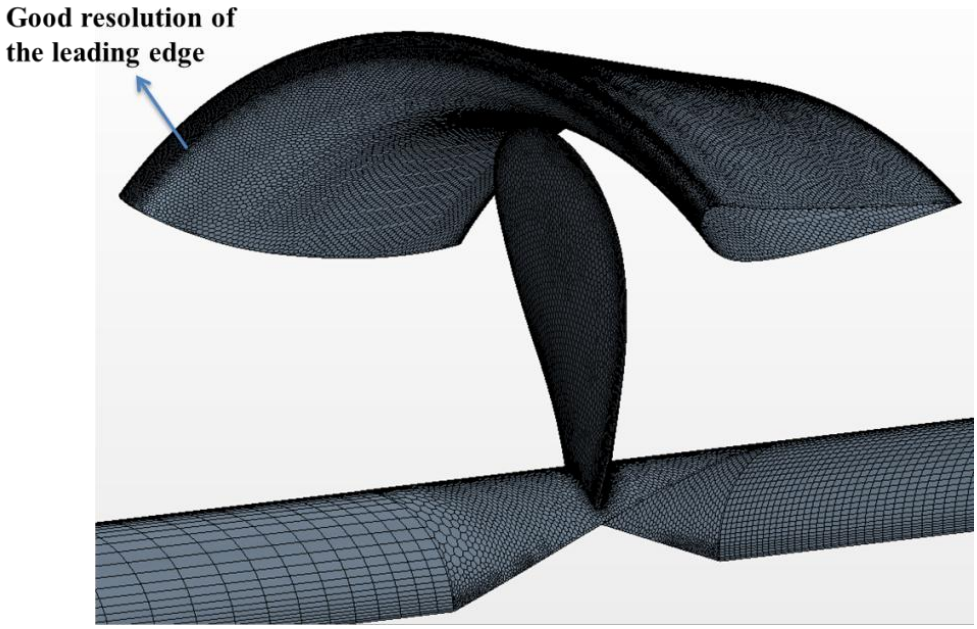

Figure 4.20 The gridding of blades and duct in the RANS simulation

As also listed in the Table 4.1, *k-ω* SST turbulence model is adopted. QUICK scheme is used for the spatial discretization and SIMPLEC scheme for the pressure correction. Over 5 million polyhedral cells are used to simulate a quarter of the domain with periodic boundary condition. It takes over 30 hours on 32 Intel Xeon 2.54 GHz CPUs for the residuals converged to 1.0E-6.

Cell number	Over 5 million
Reynolds number	1.03E+6
Turbulence Model	*k- ω* SST
Pressure Correction Scheme	*SIMPLEC*
Spatial discretization	*QUICK*
CPU Type	Intel Xeon 2.54 GHz CPU
Total time for calculation (32 CPUs)	Over 30 hours

Table 4-1 Parameter setting in the RANS simulation

The flow characteristics have been addressed at the design loading condition J_s=0.40 within two sample sections: a plane section along the axial direction ($\theta = 0^{\circ}$) and a cylindrical section of $r/R = 0.60$. The distribution of vorticity magnitude within the two sections has been presented by the contour plots.

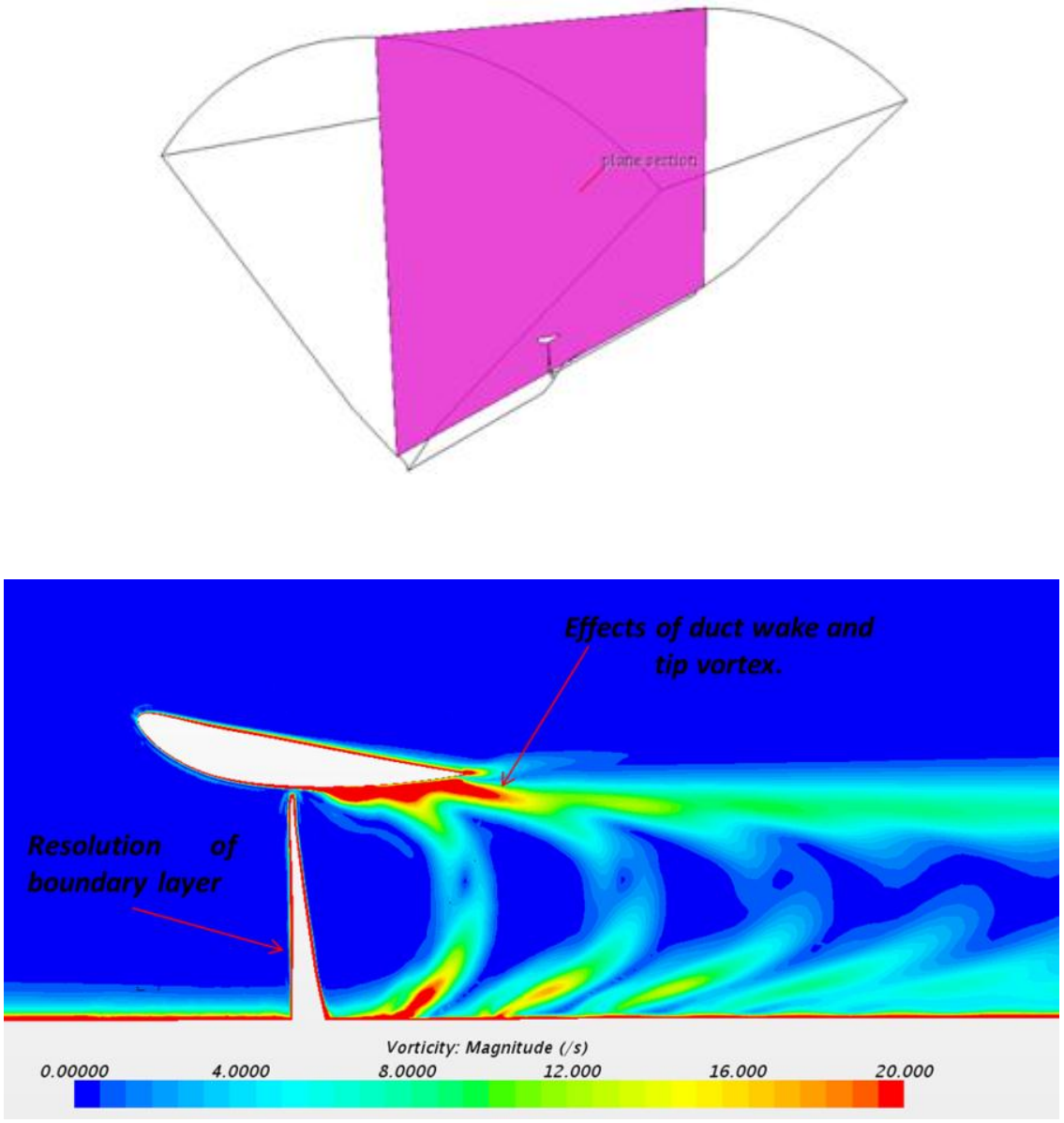

Figure 4.21 Contour of vorticity magnitude within the plane section of $\theta = 0$

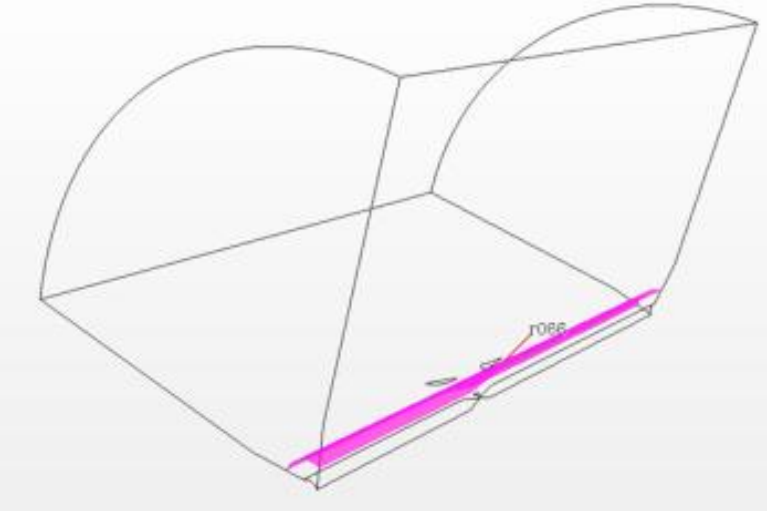

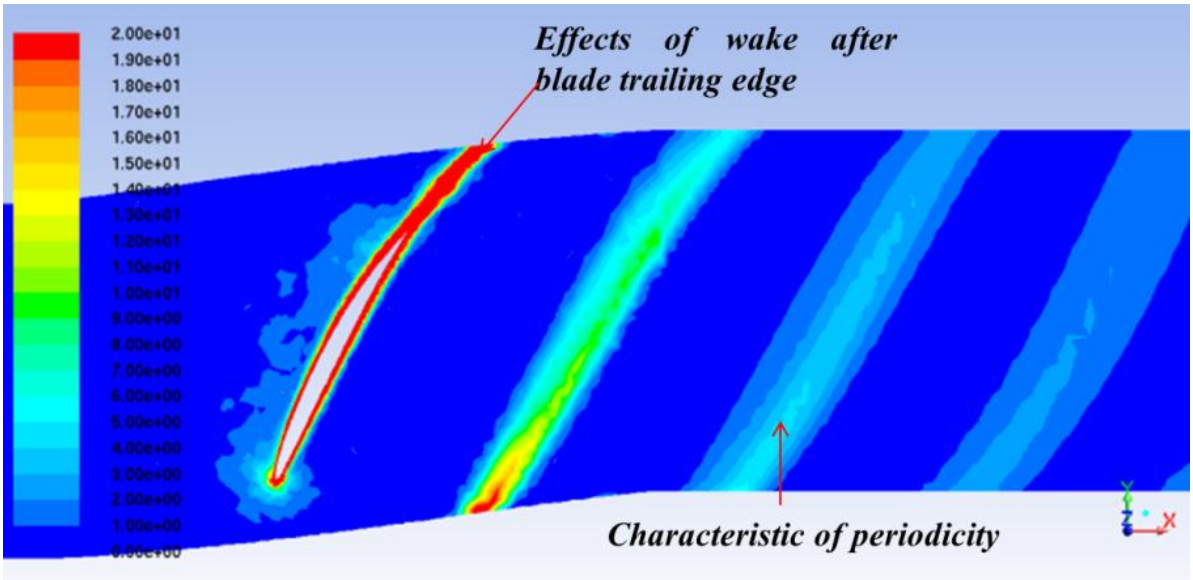

Figure 4.22 Contour of vorticity magnitude within the cylindrical section of $r/R = 0.60$

4.4.4 Correlation

4.4.4.1 Force Performance

The overall forces, i.e. thrust and torque predicted by the lower order panel method with the improved full wake alignment scheme are correlated with that from experimental measurements, the RANS/VLM coupling method and the full blown RANS simulation, as shown in Figure 4.23.

where

$$KTP = \frac{TP}{\rho n^2 D^4} \tag{38}$$

$$KQ = \frac{Q}{\rho n^2 D^5} \tag{39}$$

ρ – Fluid Density

n – Propeller Rotational Frequency (rev/s)

D – Diameter of Propeller

TP – Thrust on the Blades

Q – Torque on the Whole Propeller

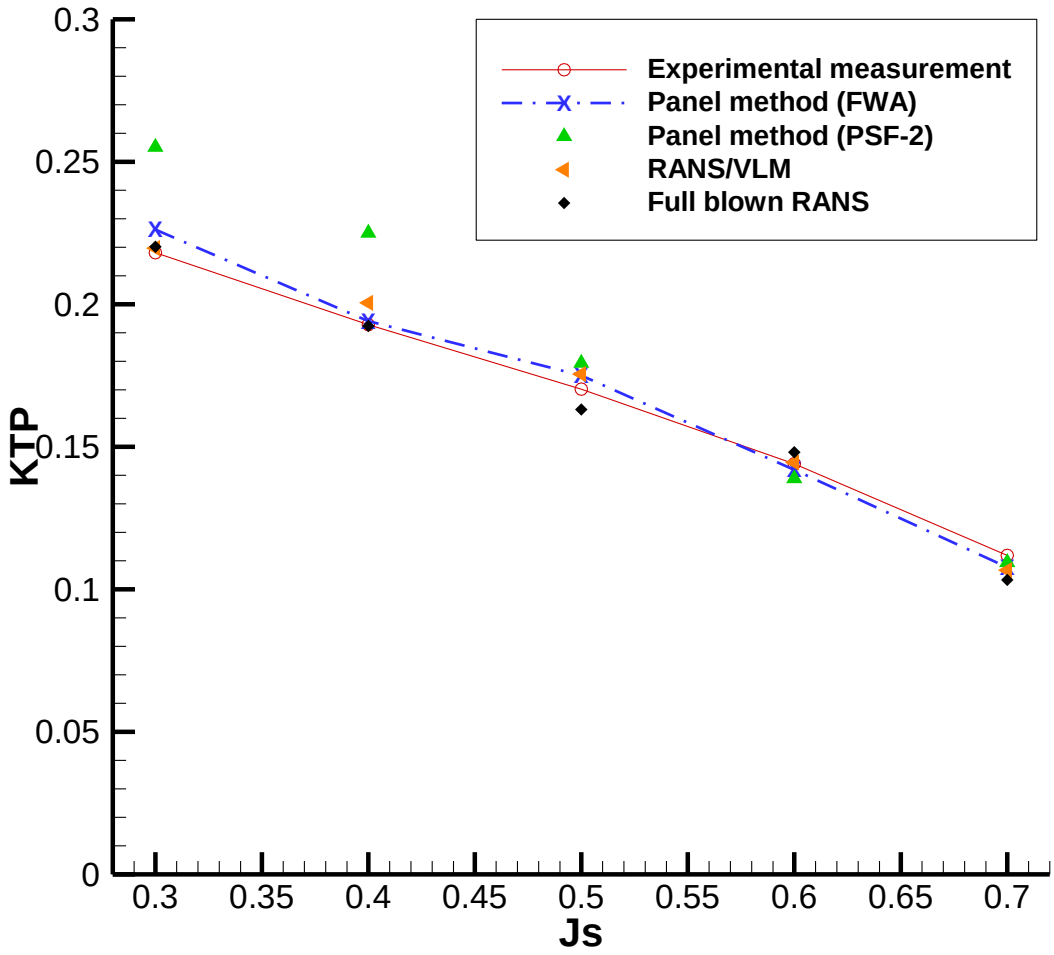

Figure 4.23 Correlation of the lower order panel method about the thrust on the blades with other methods and experimental measurements

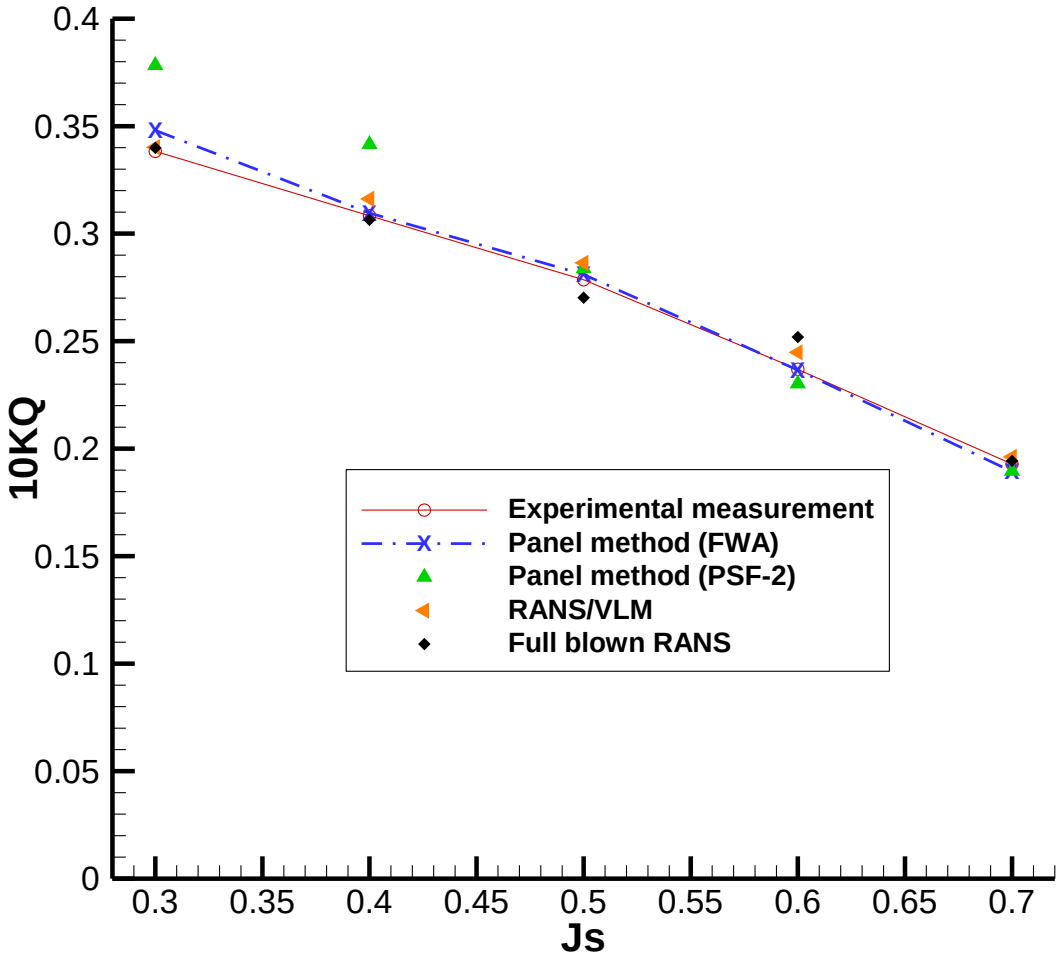

Figure 4.24 Correlation of the lower order panel method about the torque on the propeller with other methods and experimental measurements

It is found that the predicted force from the panel method with either wake model agree well with both experimental data, the full blown RANS simulations and the RANS/VLM coupling method at high advance ratios. However, as the advance ratio becomes smaller, the force predicted by the PSF-2 type scheme starts deviating from that from other methods. At the same time, the force from the full wake alignment model is still in good agreement with those predicted by the other methods.

4.4.4.2 Detailed Pressure Distribution

Figure 4.25-Figure 4.30 present the detailed correlations of pressure distribution on the propeller blades under three different loading conditions: high loading condition (Js=0.30), design loading condition (Js=0.40) and low loading condition (Js=0.50). For each loading condition, two radial blade sections, 0.65(near the mid of blades), 0.80 (close to the blade tip and duct inner surface) are selected for comparison.

The prediction of pressure distribution by full wake alignment model are in very good agreement with the full blown RANS simulation as well as the RANS/VLM coupling method at different radial sections and under different loading conditions, which is consistent with the results of the total force in Figure 4.23 and Figure 4.24

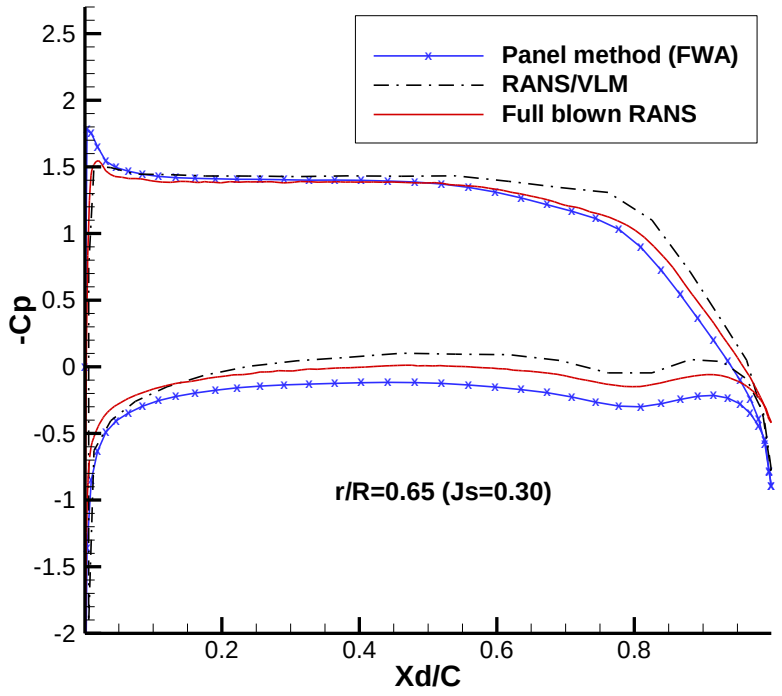

Figure 4.25 Correlation of pressure distribution at the radial section r/R=0.65 at Js=0.30

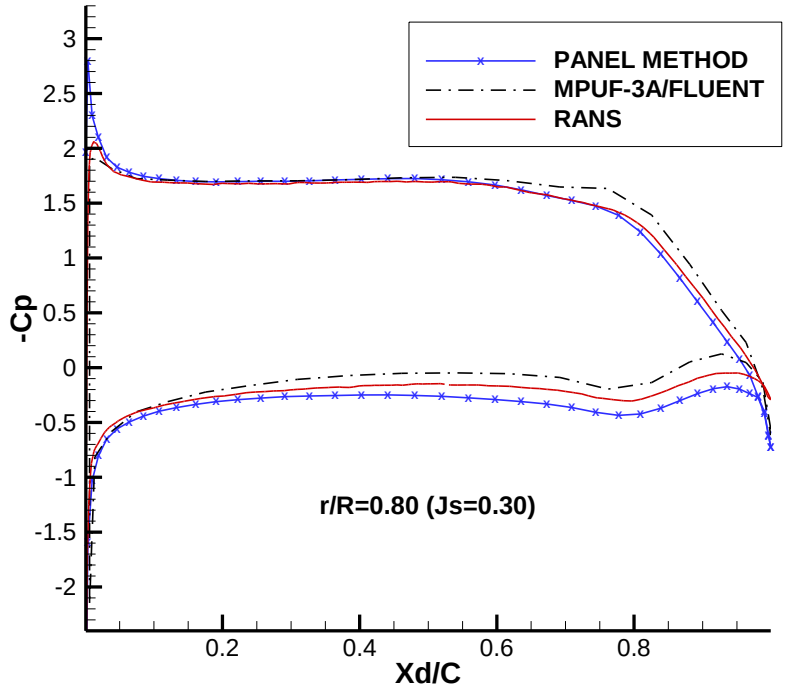

Figure 4.26 Correlation of pressure distribution at the radial section r/R=0.80 at Js=0.30

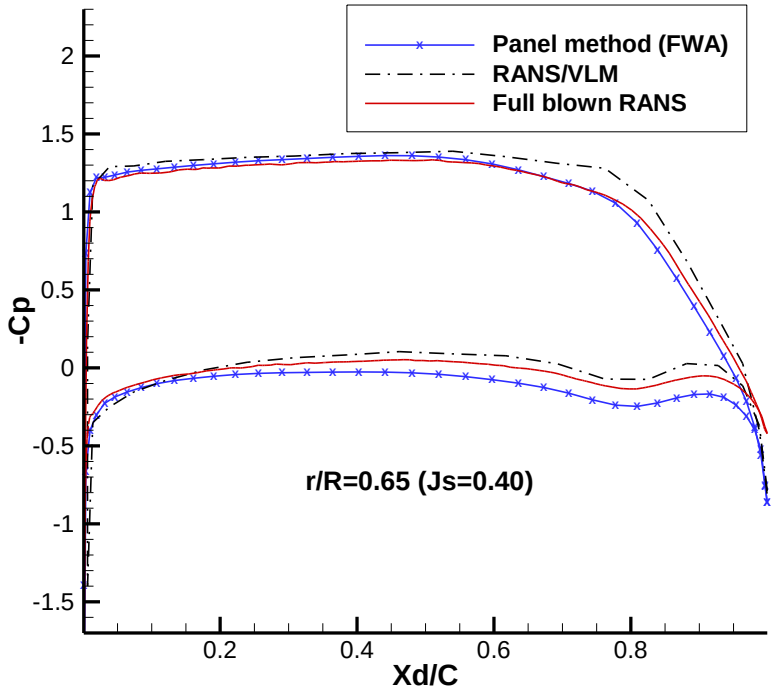

Figure 4.27 Correlation of pressure distribution at the radial section r/R=0.65 at Js=0.40

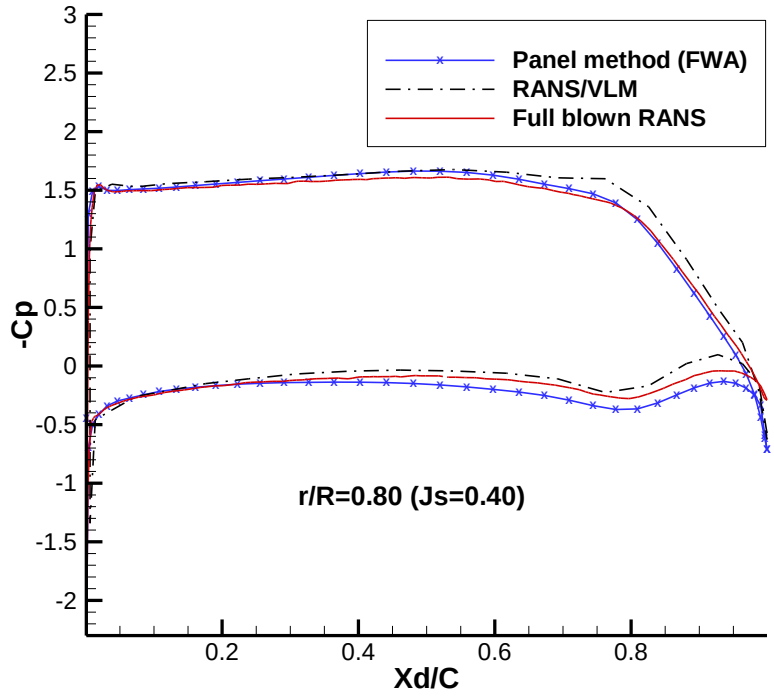

Figure 4.28 Correlation of pressure distribution at the radial section r/R=0.80 at Js=0.40

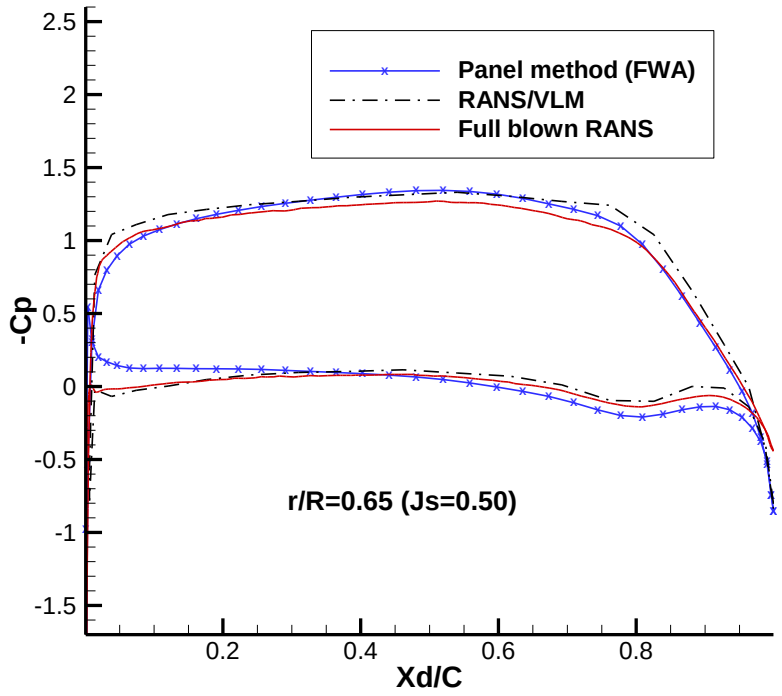

Figure 4.29 Correlation of pressure distribution at the radial section r/R=0.65 at Js=0.50

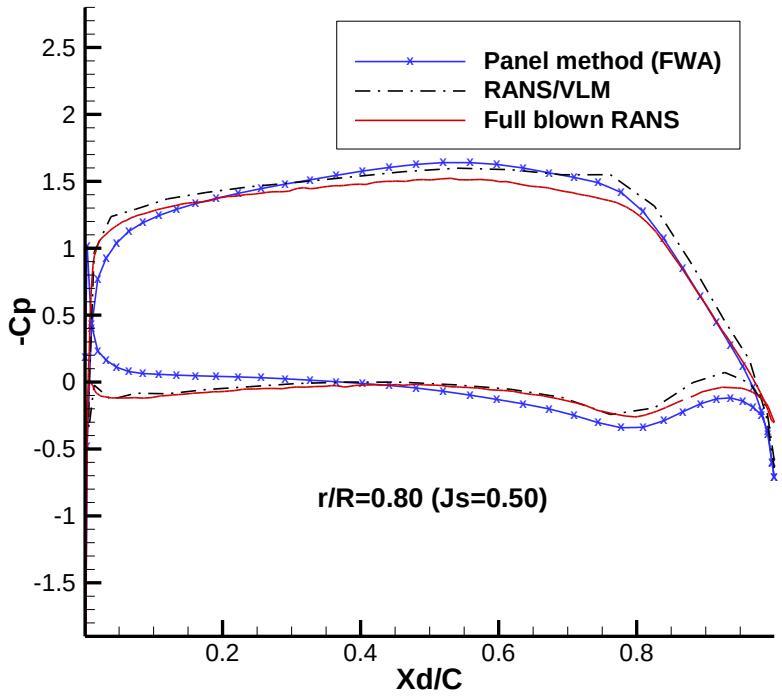

Figure 4.30 Correlation of pressure distribution at the radial section r/R=0.80 at Js=0.50

Besides the pressure distribution on the blades, it is of equal significance to evaluate the pressure distribution on the duct. In Figure 4.32, a correlation of the pressure distribution along a duct strip aligned with the pitch of the duct panels is made between the panel method with full wake alignment and full blown RANS simulation under design loading condition (Js=0.40). It should be noted that in the panel method, the evaluated points form a continuous strip. However, in order to have points fitted into the fluid domain of the full blown RANS simulation, they need to be rotated by angles dependent on the number of blades and as can be seen in Figure 4.31, the continuous strip from the panel method has to be broken into several strips. Since periodic interface has been applied, such operations are reasonable and would not affect the correctness of the pressure extracted from the full blown RANS simulations.

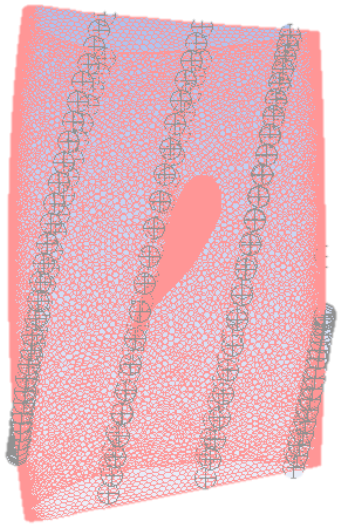

Figure 4.31 The points evaluated in the full blown RANS run after reasonable operation

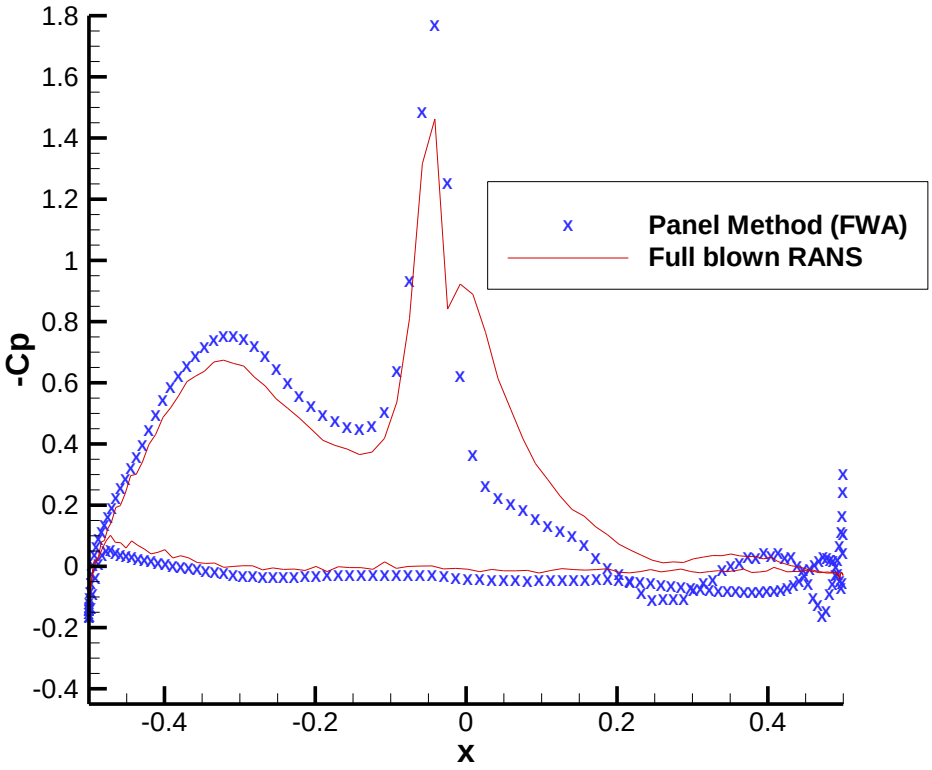

Figure 4.32 Correlation of pressure distribution along a duct strip aligned with the pitch of duct panels at *Js*=0.40

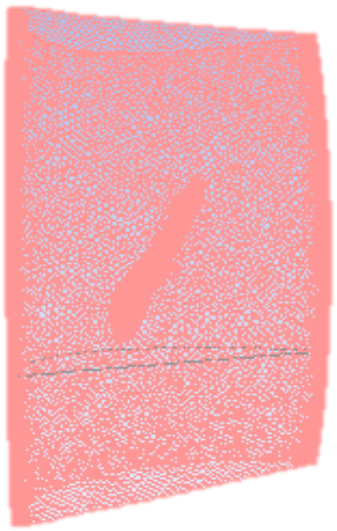

Figure 4.33 Axial strip used for correlation of pressure distribution in the axial direction

In Figure 4.34, the correlation of pressure distribution along an axial strip of the duct (Figure 4.33) is shown between the panel method with full wake alignment and the full blown RANS simulation.

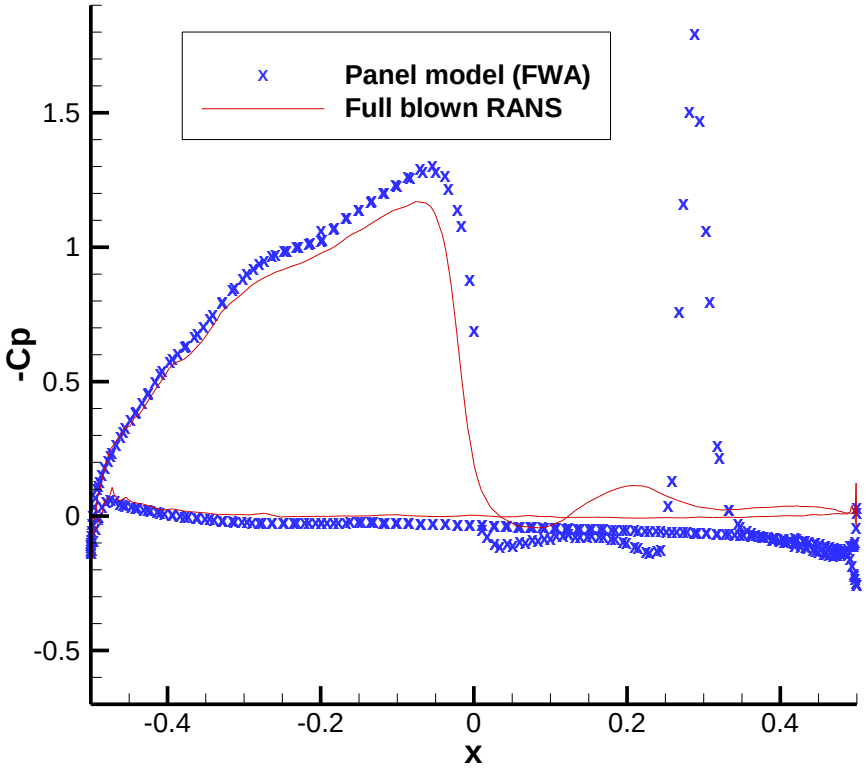

Figure 4.34 Correlation of pressure distribution along an axial strip of the duct at *Js*=0.40

Reasonable correlations have been found for most of the part in Figure 4.32 and 4.34. However the pressures from the two sides of the duct do not match well at the trailing of the duct, which needs to be addressed in future work. On the other hand, there is a pressure spike within the wake area, which might be caused by the tip vortex from other blades. In Figure 4.35-4.38, the correlations of the circumferential pressure distribution at axial location of x=-0.35 and 0.35 are shown. In addition, the circumferential distributions of potential at the same axial location are also demonstrated.

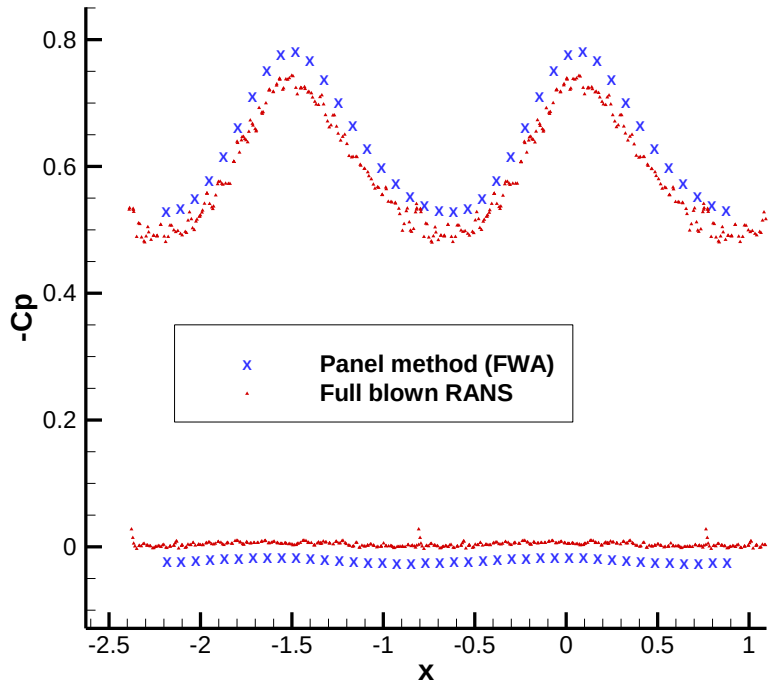

Figure 4.35 Correlation of circumferential pressure distribution at x=-0.35 under *Js*=0.40

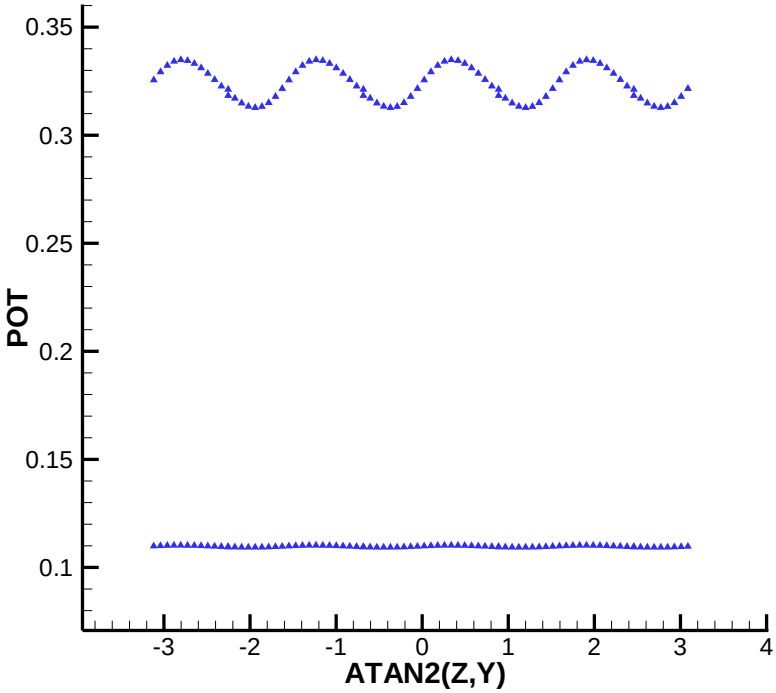

Figure 4.36 Circumferential distribution of potential from the panel method at x=-0.35 under *Js*=0.40

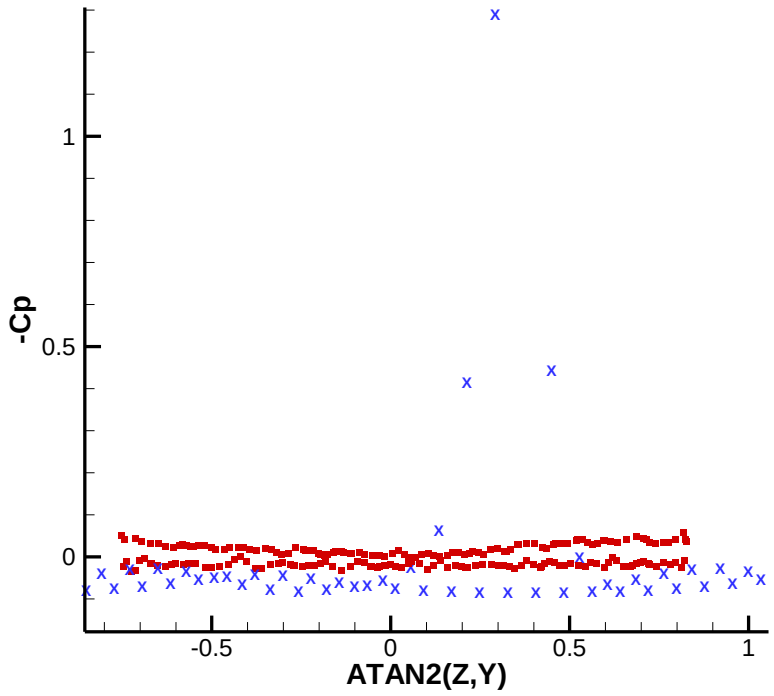

Figure 4.37 Correlation of circumferential pressure distribution at x=0.35 under *Js*=0.40

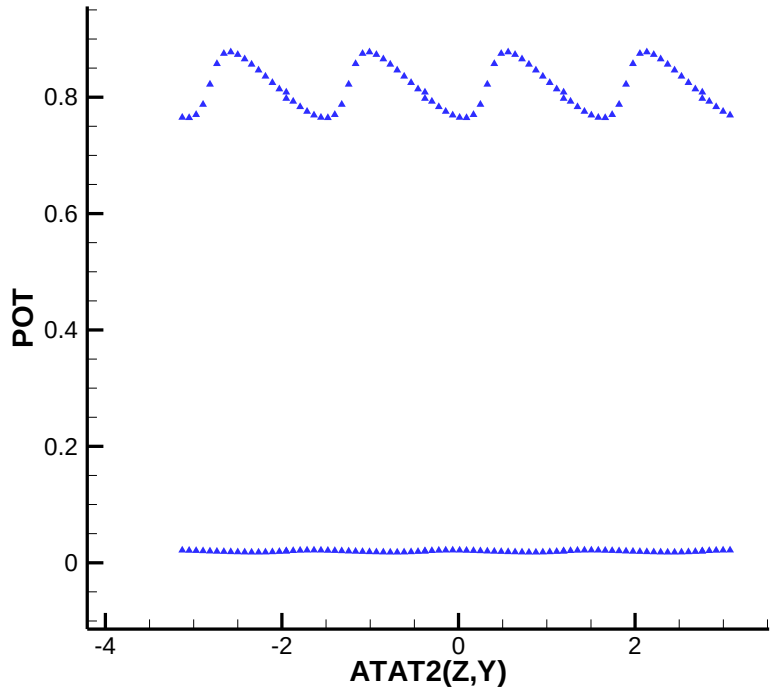

Figure 4.38 Circumferential distribution of potential from the panel method at x=0.35 under *Js*=0.40

Similar correlations of the pressure distribution along different strips are conducted under a lower loading condition *Js*=0.60. In Figure 4.39, a correlation of the pressure distribution along a duct strip aligned with the new pitch of the duct panels under *Js*=0.60 is made between the panel method with full wake alignment and full blown RANS simulation.

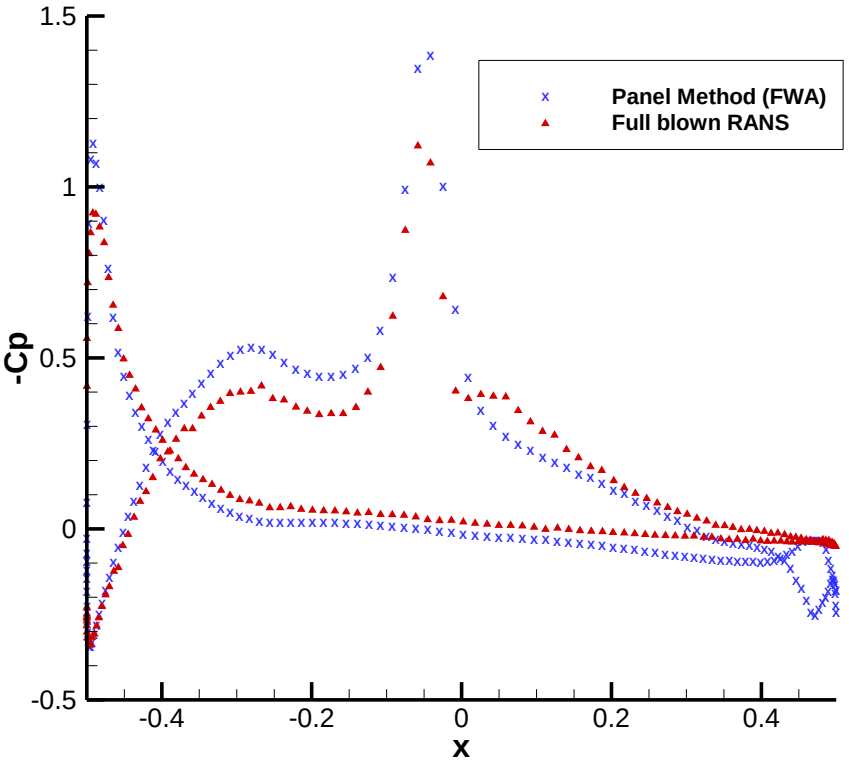

Figure 4.39 Correlation of pressure distribution along a duct strip aligned with the pitch of duct panels at *Js*=0.60

In Figure 4.40, the correlation of pressure distribution along an axial strip of the duct (Figure 4.33) is shown between the panel method with full wake alignment and the full blown RANS simulation.

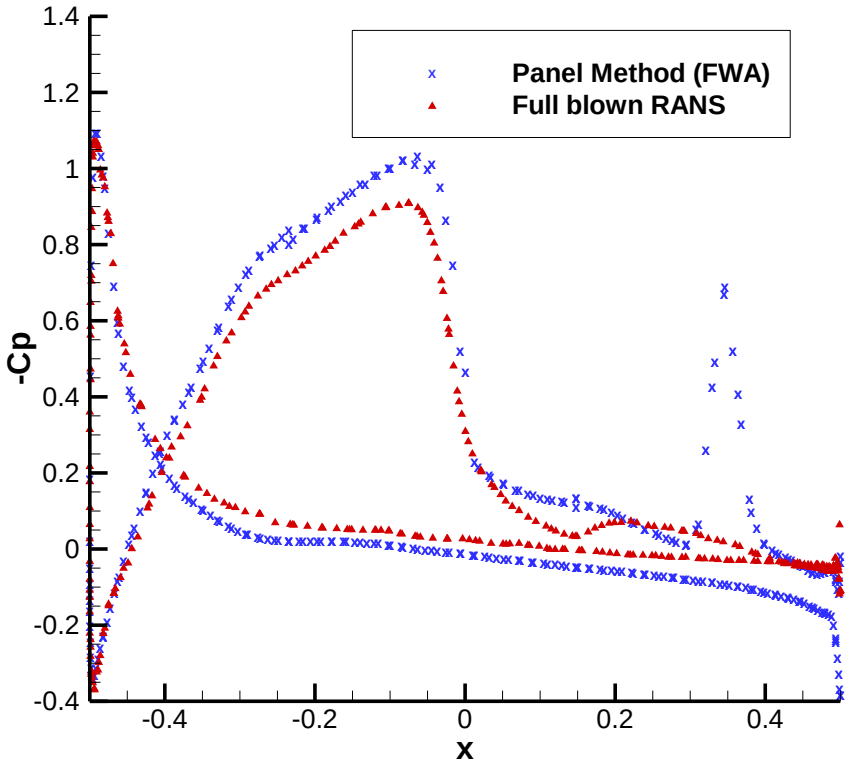

Figure 4.40 Correlation of pressure distribution along an axial strip of the duct at *Js*=0.60

In Figure 4.41 and Figure 4.38, the correlations of the circumferential pressure distribution at axial location of x=-0.35 and 0.35 are shown.

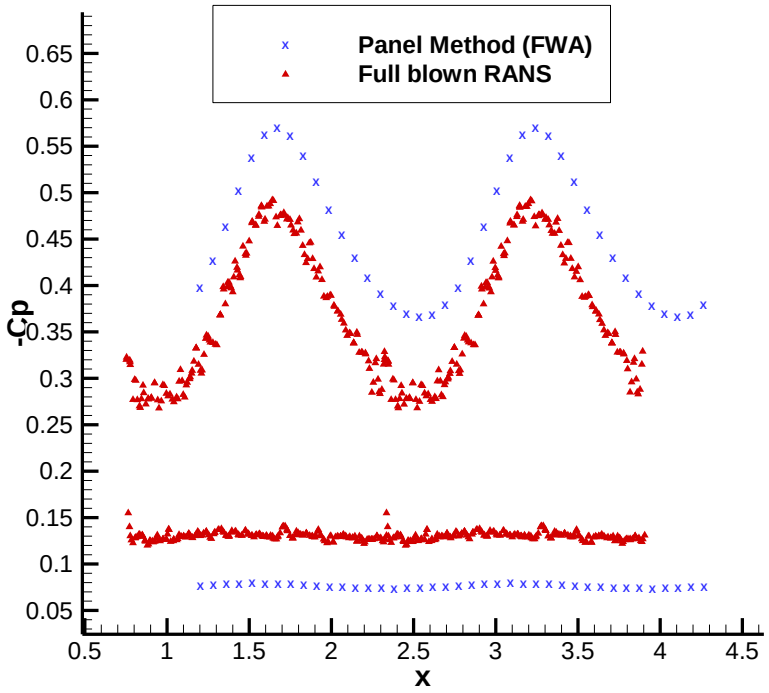

Figure 4.41 Correlation of circumferential pressure distribution at x=-0.35 under *Js*=0.60

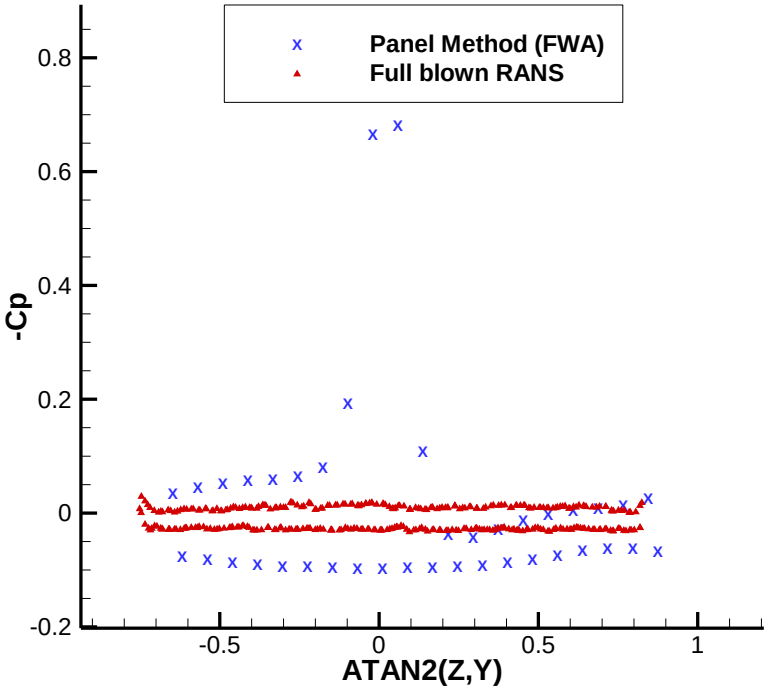

Figure 4.42 Correlation of circumferential pressure distribution at x=0.35 under *Js*=0.60

4.4.5 Comparison of Computational Efficiency

Since in the present lower order panel method, it is not necessary to grid the whole fluid domain, making the panel method much more computationally efficient than the full blown RANS simulations. In the current case, the panel method takes only about 1/60 of the CPU time, while using only one processor versus 32 processors used in the case of full blown RANS simulations. In addition, the time devoted in gridding for the full blown RANS can take several days while it is negligible for the panel method.

Method	Full blown RANS	PANEL METHOD
Cell No.	Over 5 million cells	Less than 12K panels (10 iterations for wake)
Total running time	Over 30 hours (32 CPUs)	30 minutes (1 CPU)

Table 4-2 Computation efficiency comparison between the panel method and the full blow RANS simulation

4.5 Ducted Propeller with Square Blade Tip and Sharp Trailing Edge Duct

In this part, the lower order panel method would be applied to a ducted propeller with square blade tip and a sharp trailing edge duct. Two different wake alignment models, PSF-2 type wake scheme and full wake alignment scheme will be involved.

The overall forces predicted by the present panel method will be correlated with that from the full blown RANS simulation and experimental measurements. Since the detailed pressure distribution on the blade surface is of great significance to the modeling

of cavitation flow, related correlations would be performed between the panel method, and the full blown RANS simulation.

The geometry of the ducted propeller and the 2-D section of its duct are indicated in Figure 4.43. It is a 4-blade propeller with square blade tip and bounded within a sharp trailing edge duct 19Am. The duct 19Am is modified by MARIN from duct 19A which has a blunt trailing edge that the current panel method cannot well resolve because of the recirculation region. The design advance ratio J_s of this propeller is around 0.50. No gap is included in this case.

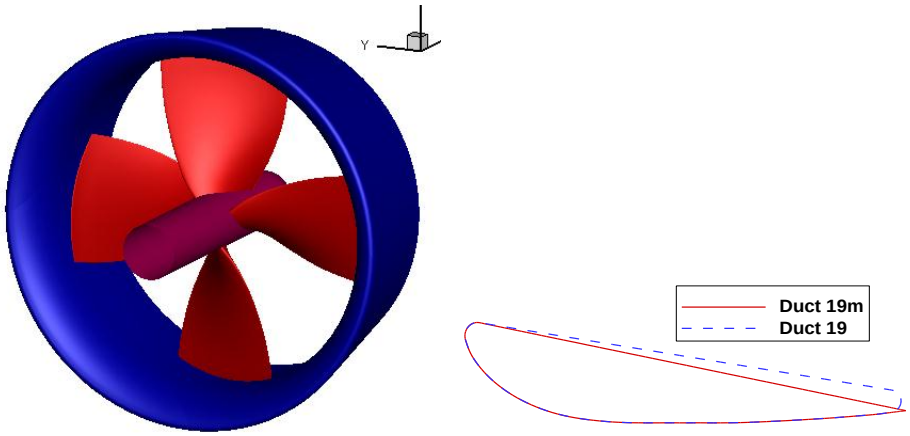

Figure 4.43 Geometry of the ducted propeller with square blade tip and the two dimension section of the sharp trailing edge duct

4.5.1 Lower Order Panel Method

For the lower order panel method, 80× 30 (chordwise×spanwise) and 200×80 (chordwise×circumferential) panels are used to resolve the blade and duct. Two wake models, PSF-2 wake model and full wake alignment (FWA) scheme, are adopted. For all advance ratios, PSF-2 scheme trimmed the blade wakes at 3R downstream with an

ultimate wake disk, while the full wake alignment scheme models blade wakes of one revolution. It takes about 30 minutes and 3 minutes for full wake alignment and PSF-2 wake model to complete the run on a single core of Intel Xeon 2.54 GHz CPU. The wake geometry from the two models at J_s =0.4, 0.5 and 0.6 are shown in Figure 4.44-4.49.

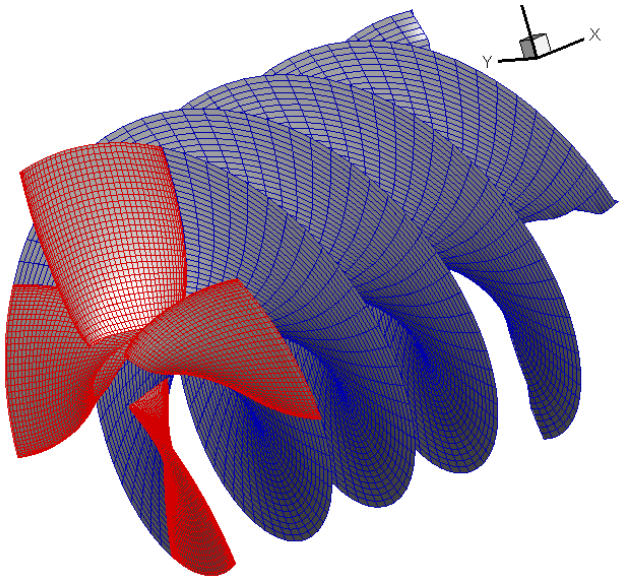

Figure 4.44 Wake geometry generated from PSF-2 wake model at J_s=0.40

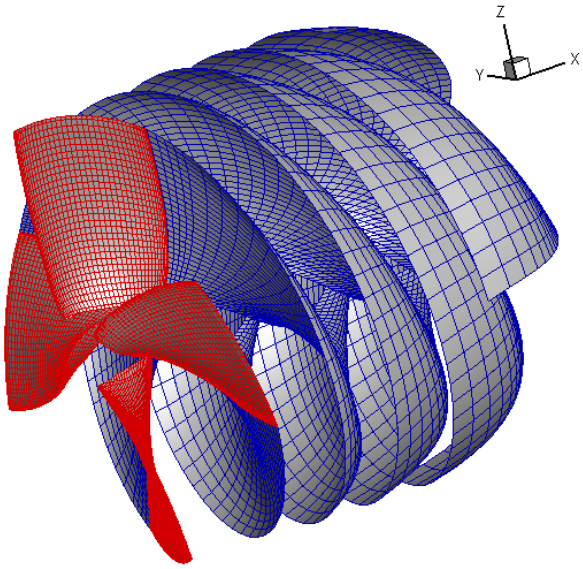

Figure 4.45 Wake geometry generated from full wake alignment scheme at J_s=0.40

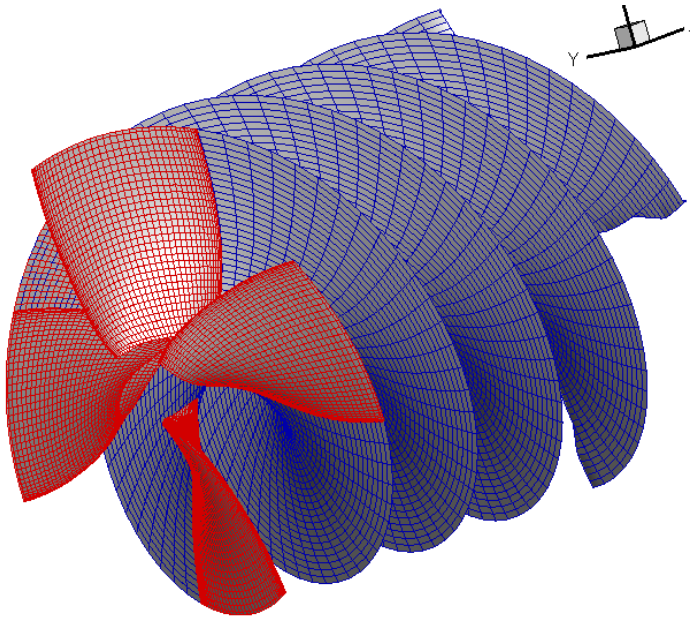

Figure 4.46 Wake geometry generated from PSF-2 wake model at J_s=0.50

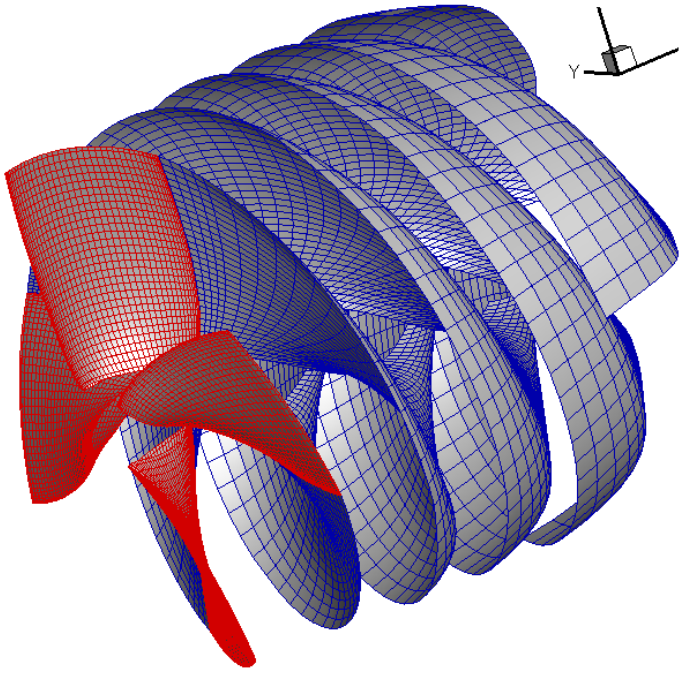

Figure 4.47 Wake geometry generated from full wake alignment scheme at J_s=0.50

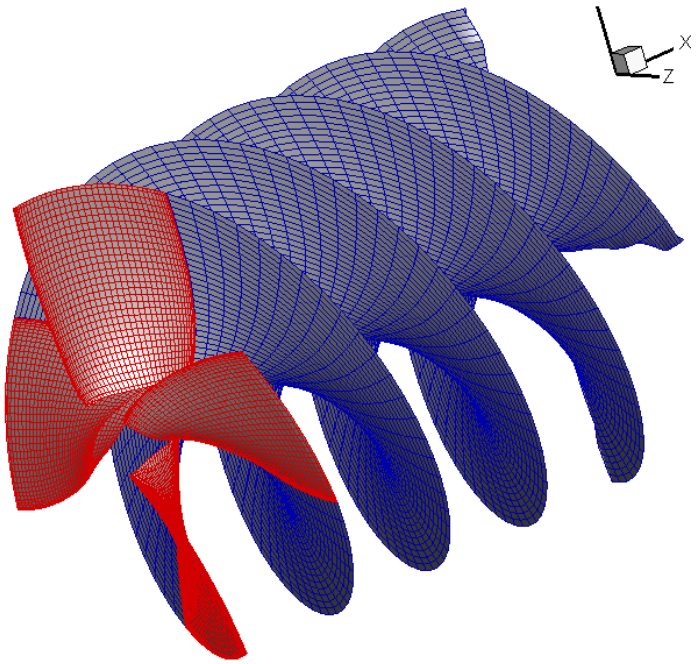

Figure 4.48 Wake geometry generated from PSF-2 wake model at J_s=0.60

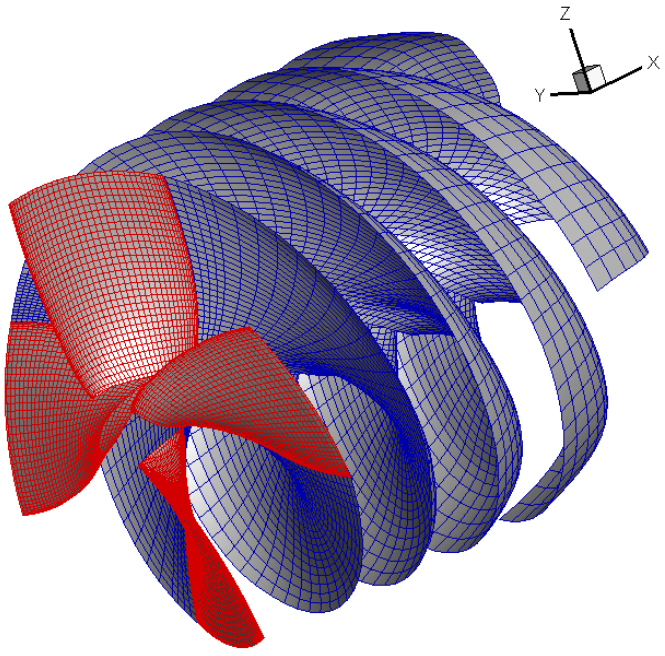

Figure 4.49 Wake geometry generated from full wake alignment scheme at J_s=0.60

At high loading, the contraction rate of the transition wake is set as zero in PSF-2 wake scheme and the model did not predict the contraction of the transition wake radius. While in full wake alignment model, the rollup of the wake sheets at low advance ratios is well predicted.

As will be shown shortly at all loading conditions, whether contraction of the wake radius has been well predicted (FWA) or not (PSF-2) plays a significant role in if an accurate prediction of force can be obtained.

4.5.2 Full Blown RANS simulation

The full blown RANS simulation are performed within ANSYS Fluent as well as Star-CCM+ in which periodic interfaces have been applied such that for the present propeller only a quarter of the whole fluid domain is necessary for further simulation. In addition, to better resolve the boundary layer structures on the blades and duct, structured meshing model has been adopted. The same gridding model has been used for the trailing wake of the blades and duct in order to reduce the possible artificial diffusivity.

As also listed in the Table 4.3, k-ω SST turbulence model is adopted. QUICK scheme is used for the spatial discretization and SIMPLEC scheme for the pressure correction. Over 6 million polyhedral cells are used to simulate a quarter of the domain with periodic boundary condition. It takes over 32 hours on 32 Intel Xeon 2.54 GHz CPUs for the residuals converged to 1.0E-6.

Cell number	Over 6 million
Reynolds number	1.0E+6
Turbulence Model	*k-ω* SST
Pressure Correction Scheme	*SIMPLEC*
Spatial discretization	*QUICK*
CPU Type	Intel Xeon 2.54 GHz CPU
Total time for calculation (32 CPUs)	Over 32 hours

Table 4-3 Parameter setting in the RANS simulation

4.5.3 Correlation

4.5.3.1 Force Performance

The overall forces, i.e. thrust and torque predicted by the lower order panel method with PSF-2 type scheme and the improved full wake alignment scheme are correlated with that from experimental measurements and the full blown RANS simulation, as shown in Figure 4.50.

It is observed that the panel method with PSF-2 type scheme always greatly overestimates the thrust and torque on the propeller. On the other hand, by applying the improved full wake alignment, the predicted forces agree well with both experimental data and full blown RANS simulations at most advance ratios. Only at very high loading will the FWA overestimates the force, even though not considerably.

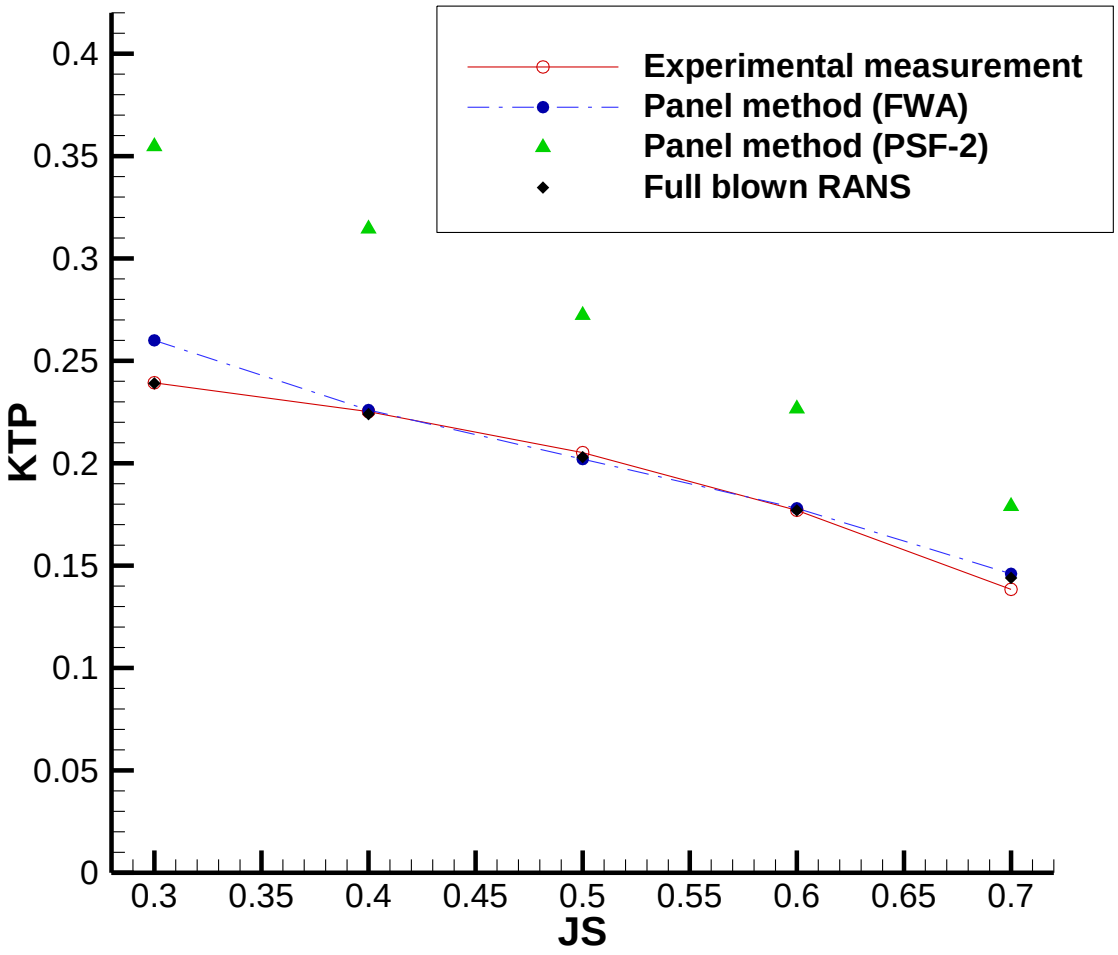

Figure 4.50 Correlation of the lower order panel method about the thrust on the blades with other methods and experimental measurements

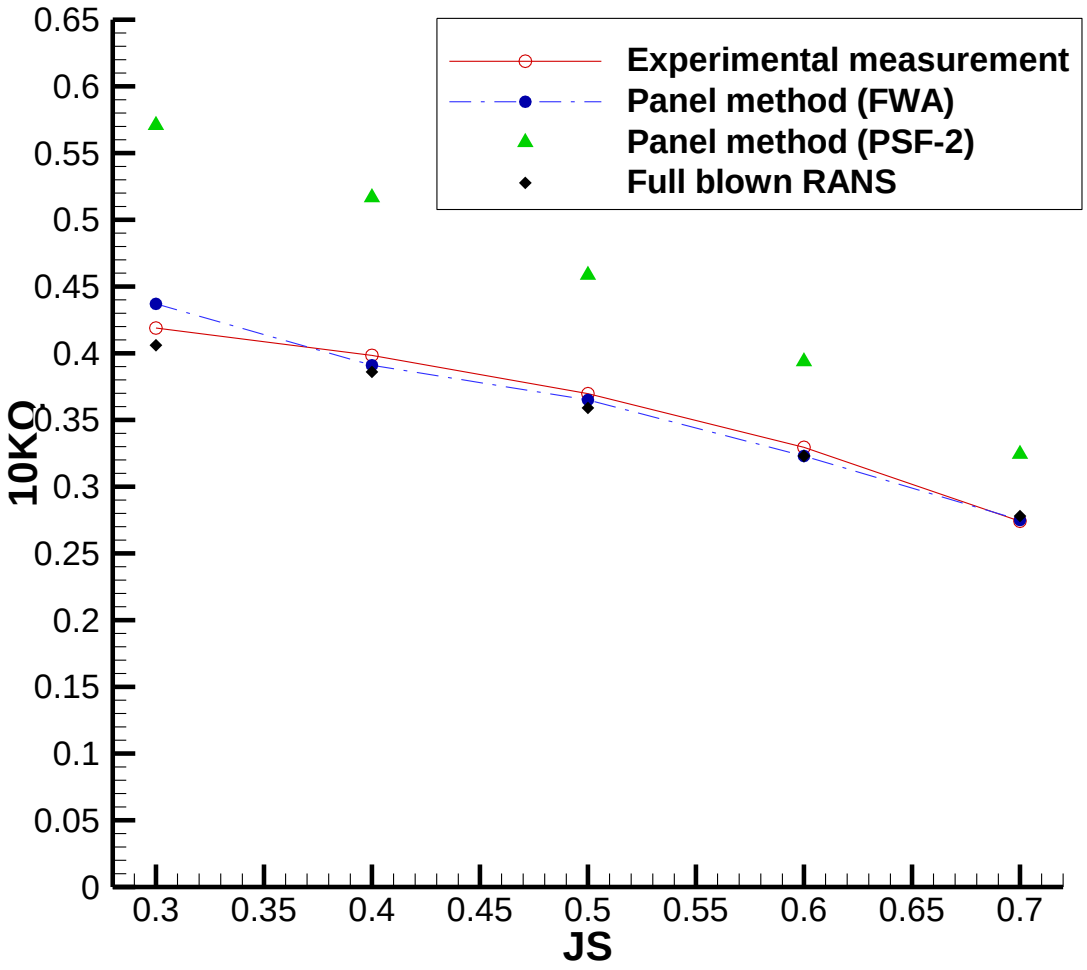

Figure 4.51 Correlation of the lower order panel method about the torque on the propeller with other methods and experimental measurements

4.5.3.2 Detailed Pressure Distribution

Figure 4.52-Figure 4.57 present the detailed correlations of pressure distribution on the propeller blades under three different loading conditions: high loading condition (*Js*=0.40), design loading condition (*Js*=0.50) and low loading condition (*Js*=0.60). For each loading condition, two radial blade sections, 0.65(near the mid of blades), 0.86 (close to the blade tip and duct inner surface) are selected for comparison.

The predictions of pressure distribution by full wake alignment model are in very good agreement with the full blown RANS simulation at different radial sections and under different loading conditions.

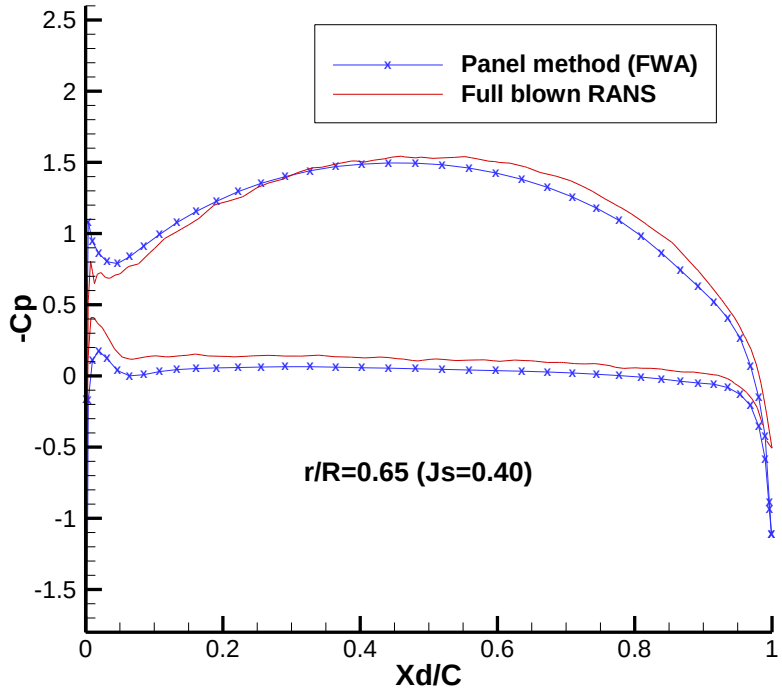

Figure 4.52 Correlation of pressure distribution at the radial section r/R=0.65 at Js=0.40

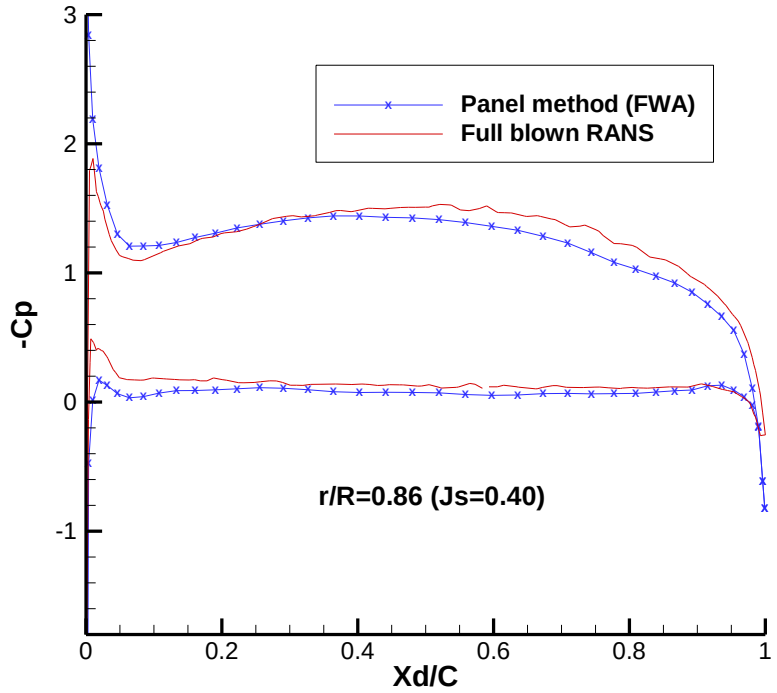

Figure 4.53 Correlation of pressure distribution at the radial section r/R=0.86 at Js=0.40

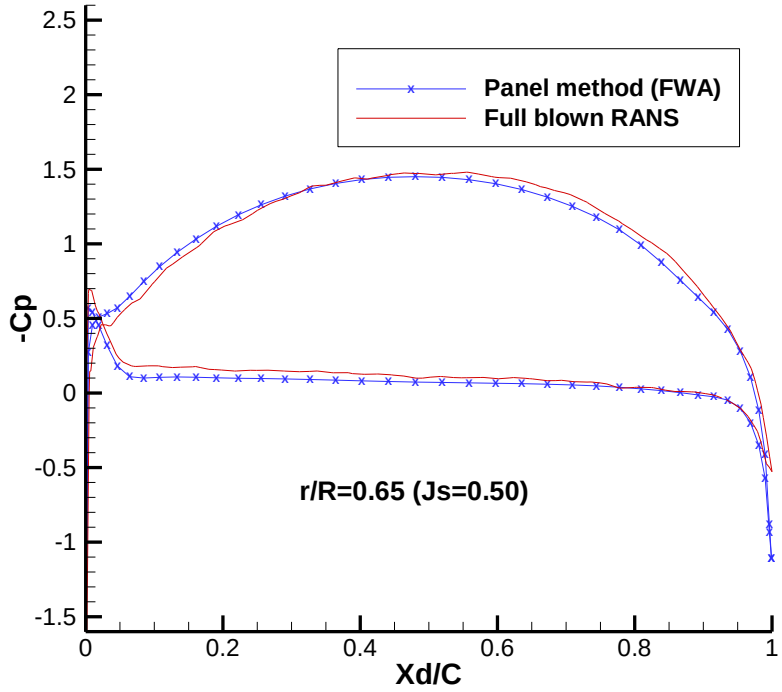

Figure 4.54 Correlation of pressure distribution at the radial section r/R=0.65 at Js=0.50

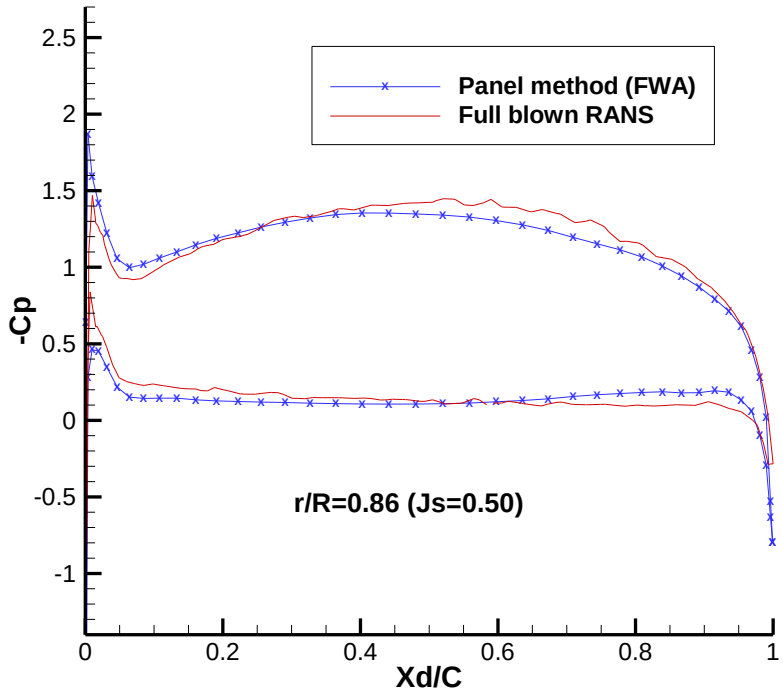

Figure 4.55 Correlation of pressure distribution at the radial section r/R=0.86 at Js=0.50

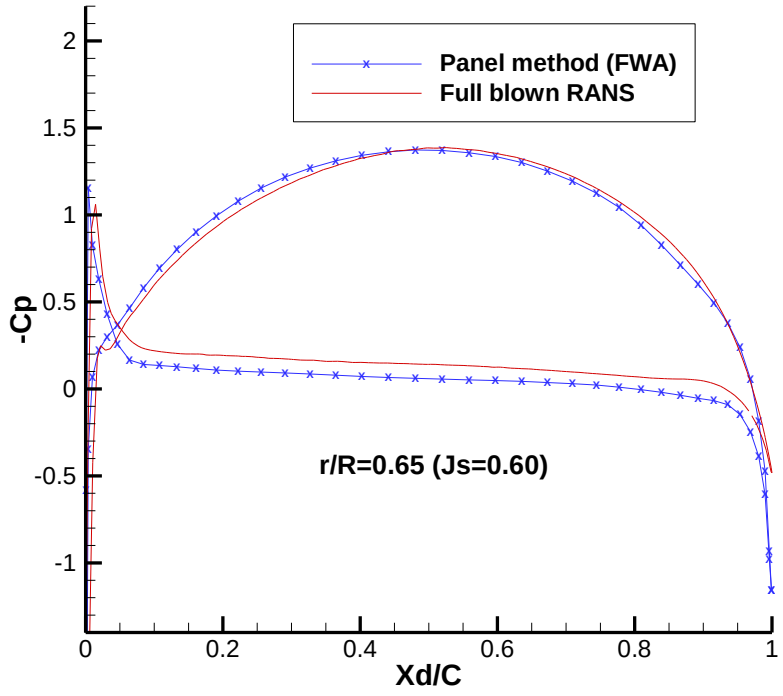

Figure 4.56 Correlation of pressure distribution at the radial section r/R=0.65 at Js=0.60

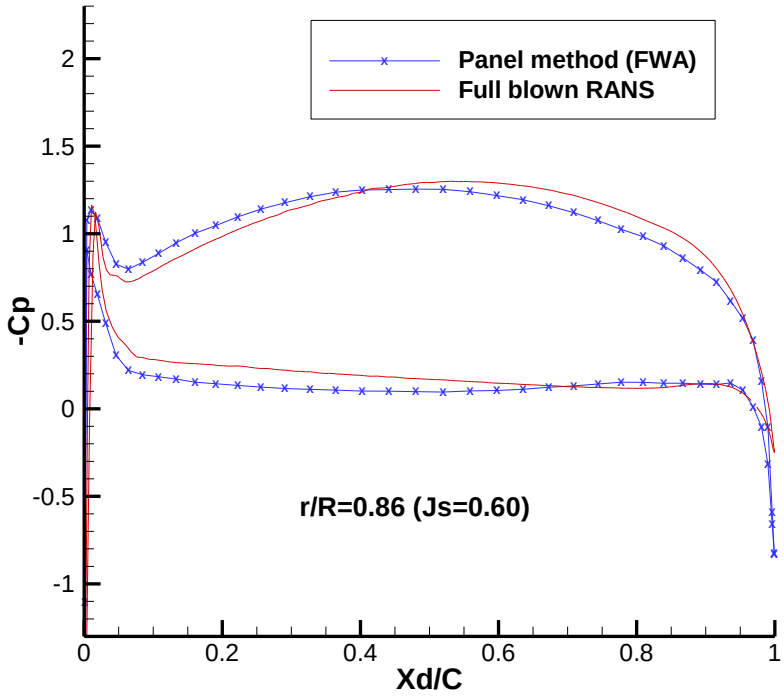

Figure 4.57 Correlation of pressure distribution at the radial section r/R=0.86 at Js=0.60

4.5.4 Comparison of Computational Efficiency

Since by applying the lower order panel method, it is not required to grid the whole fluid domain, making the panel method much more computational efficient than the full blown RANS simulations. In the current case, the panel method takes only about 1/60 of the CPU time, while using only one processor versus 32 processors used in the case of full blown RANS simulations. In addition, the time devoted in gridding for the full blown RANS can take several days while it is negligible for the panel method.

Method	Full blown RANS	PANEL METHOD
Cell No.	Over 6 million cells	Less than 12K panels (10 iterations for wake)
Total running time	Over 32 hours (32 CPUs)	30 minutes (1 CPU)

Table 4-4 Computational efficiency comparison between the panel method and the full blown RANS simulation

Chapter 5 Evaluation of Viscous Effects on Duct

So far the algorithm of resolving the effects of viscosity, though theoretically introduced within the scheme of viscous/inviscid interactive method in Chapter 2 and Chapter 3, has not been validated through actual cases yet.

In this chapter, the viscous/inviscid interactive method will be applied to the analysis of the axisymmetric flow of a long duct, the axisymmetric of a bare duct with non-zero trailing edge thickness and the three-dimensional flow around a ducted propeller with a blunt trailing edge duct. It should be noted that for the latter two cases, the recirculation zone around the blunt trailing edge of the duct cannot be well addressed by the present method. Therefore an extension scheme originally proposed by Pan (2009) has been improved to reasonably modify the blunt trailing edge to a sharp one such that further calculation can be carried out.

5.1 Long Duct

The three dimensional viscous/inviscid interactive method is applied for validation to the case of a long duct with relatively large ratio of chord length over duct radius in which the boundary layer effects is more prominent. The geometry of the long duct is shown in Figure 5.1.

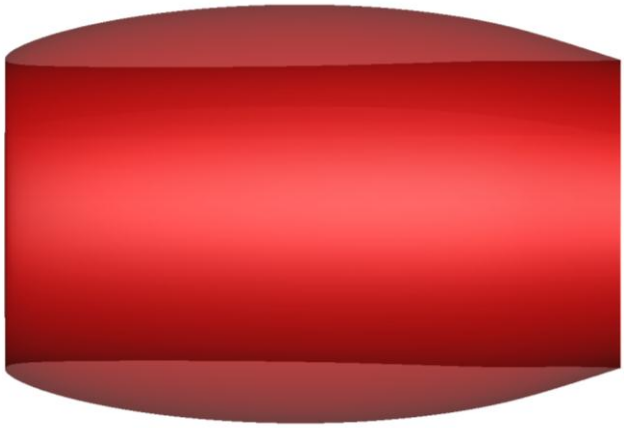

Figure 5.1 Geometry of the long duct

The discretization of the duct surface and the duct wake by applying the viscous/inviscid interactive method is shown in Figure 5.2. Structured gridding has been adopted, which has been proven to be particularly essential for resolving the wake structures.

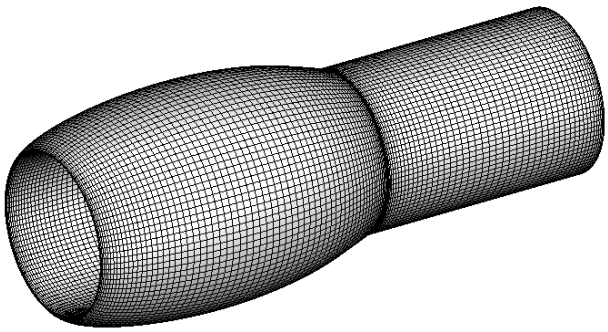

Figure 5.2 Structured gridding of the long duct in viscous/inviscid interactive method

In order to have reliable correlation of the interactive method, an axisymmetric RANS simulation with the same duct shape is performed in ANSYS Fluent. The RANS simulation uses over 150,000 hexahedral cells for the discretization of fluid domain with

its Reynolds number at 4E+6. *k-w* SST turbulence model is used. SIMPLEC scheme is applied for the pressure correction scheme and QUICK scheme is adopted for the spatial discretization. It takes about 3 hours on 8 Intel Xeon 2.54 GHz CPUs for the residuals to be lower than 1E-6. The dimension as well as the boundary conditions of the flow domain is shown in Figure 5.3.

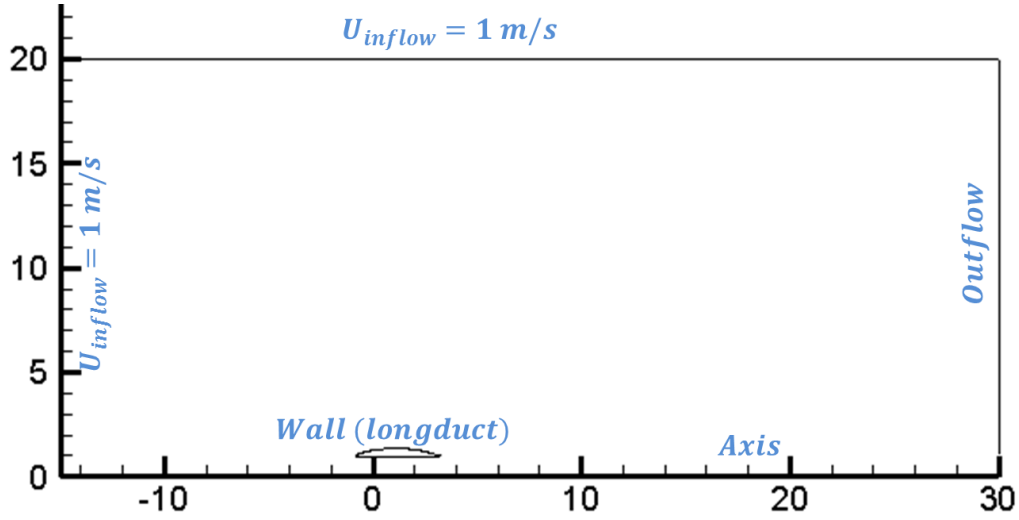

Figure 5.3 Dimension and boundary condition of the RANS simulation

In the RANS simulation, the gridding close to the long duct is of essential importance since it determines whether or not the boundary layer about the body can be well resolved. In this case, the mesh around the long duct is fine enough as the value of y^+ is under 1. Figure 5.4 shows the fine mesh around the leading edge of the duct.

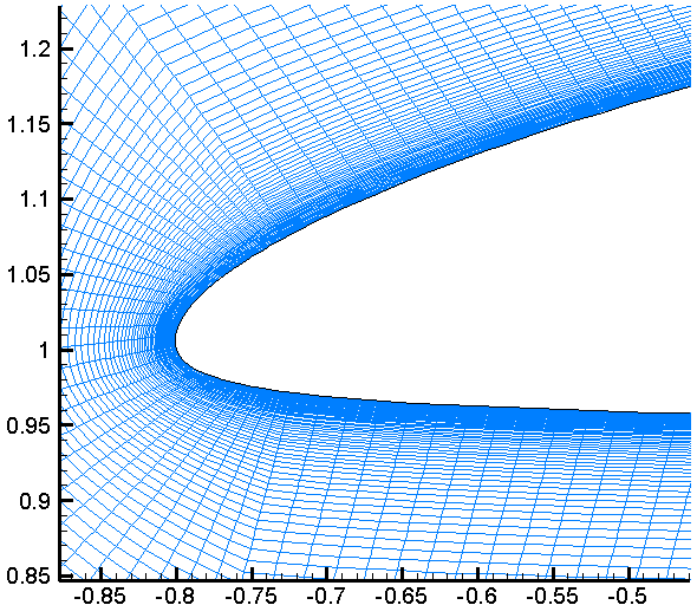

Figure 5.4 Fine mesh around the leading edge of the long duct in RANS simulation

The correlations between the viscous/inviscid interactive method and the axisymmetric RANS simulation are made on the distributions of pressure and skin friction on the duct, as shown in Figure 5.5 and Figure 5.6. An axisymmetric formulation instead of 3-D formulation has been developed and applied for this specific case.

It can be seen that the present viscous/inviscid interactive method can accurately predict the pressure distribution on the duct surface. On the other hand, it can also render relatively good prediction of the skin friction coefficient on the duct, which is an important parameter indicating how well the boundary layer is resolved.

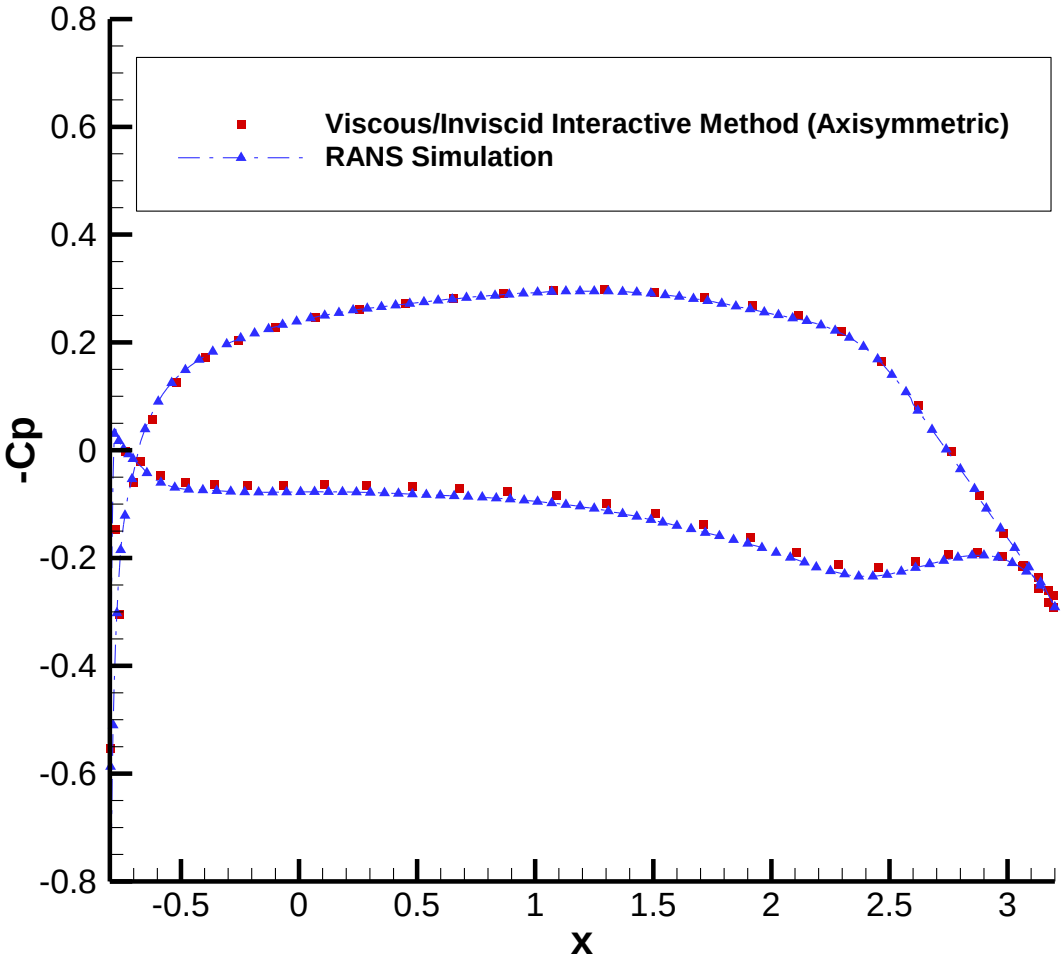

Figure 5.5 Correlation of the chordwise pressure distribution on the long duct between the axisymmetric viscous/inviscid interactive method and the RANS simulation

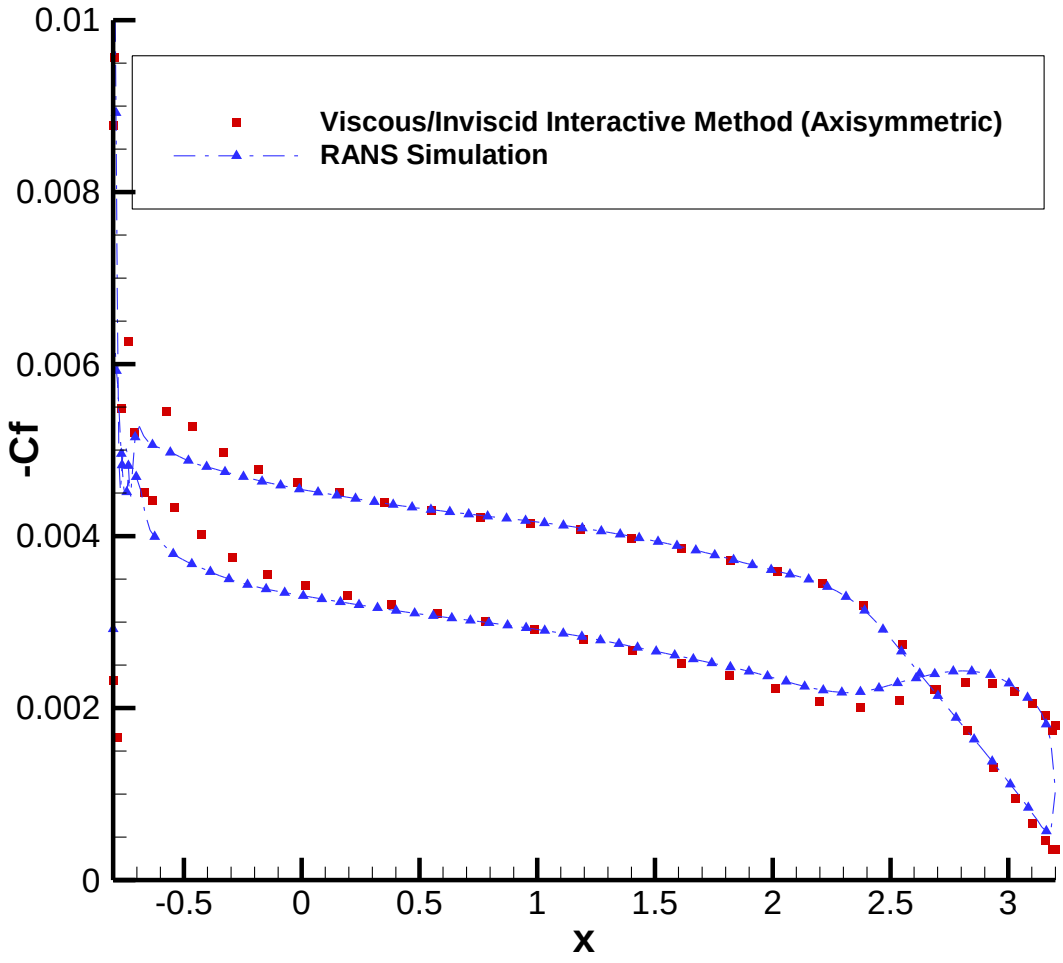

Figure 5.6 Correlation of the chordwise distribution of skin friction on the long duct between the axisymmetric viscous/inviscid interactive method and the RANS simulation

5.2 Extension Scheme

In the case of a bare duct with blunt trailing edge or a ducted propeller with a blunt trailing edge duct, there will be a considerable recirculation zone around the duct trailing edge, which cannot be well resolved by the present method. To make the method applicable, the trailing edge of the duct should be reasonably extended to a sharp one. It should also be noted that the modification is expected to applied only to the aft part of the duct, the forward part should be maintained as it is.

An extension scheme was proposed by Pan (2009) in which the trailing edge of the duct is extended linearly. The scheme was improved by Yu (2012) by using quadratic polynomials. Purohit (2013) further improved the scheme and applied it the three dimensional ducts with and without propellers. So far the location of cut planes indicating the starting point of the extension is determined arbitrarily. It is expected to have a rational criterion of determining that location. Considering that the location is an implication of the starting point of flow separation, in this chapter the skin friction C_f is used as the specific criterion, as will be seen in more details later.

5.2.1 Algorithm

In Figure 5.7 an original duct shape with blunt trailing along with its shape after extension is shown. The algorithm for the extension scheme via quadratic polynomials is subsequently explained in Figure 5.8.

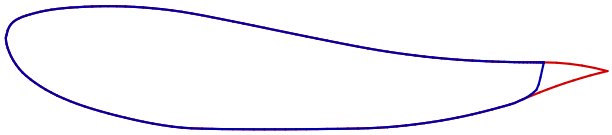

Figure 5.7 Duct with blunt trailing edge and the modified shape after extension

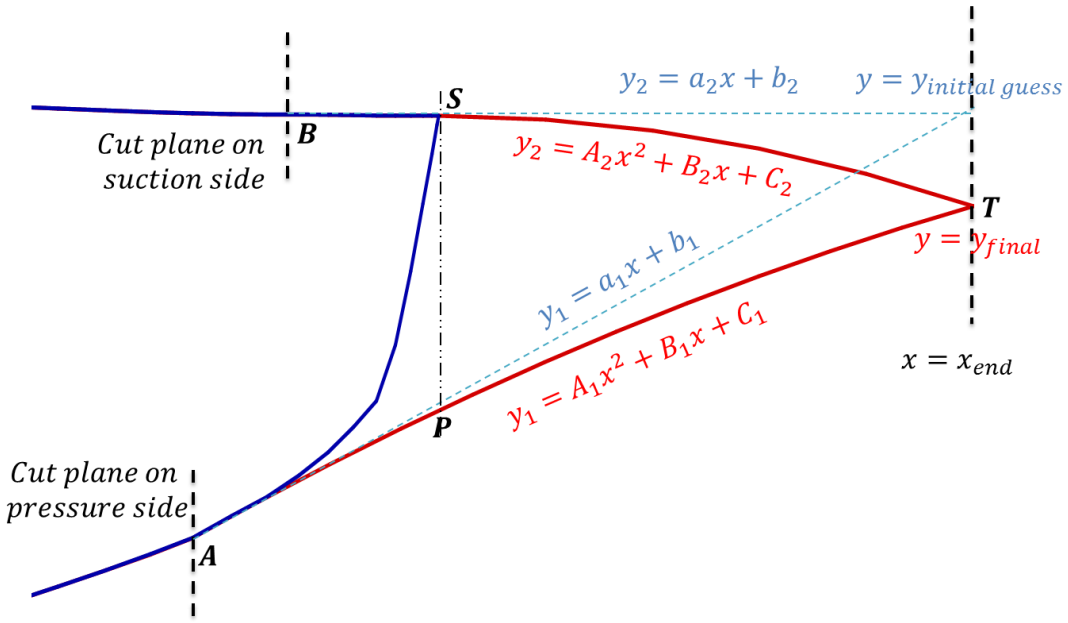

Figure 5.8 Algorithm of the extension scheme

As the first step, the locations of starting points or hereby referred as cut planes, need to be decided on both sides of the duct. Different selections of such locations would produce quite different shapes after the extension. Therefore as aforementioned, a rational criterion should be implemented. Since the skin friction is a typical implication about where the flow separation starts, the condition of $C_f = 0$ is then used as the specific criterion, where C_f stands for the skin friction coefficient. As the initial attempt, the

extension is done in a linearly way, that is, the shape after the cut planes is composed of two straight lines. A horizontal coordinate $x = x_{end}$ can be obtained at the joint point of the two straight lines. In the next iterations, the horizontal coordinate of the new trailing edge is always fixed at $x = x_{end}$, that is, only the vertical coordinate is varied to get different shapes. One a new vertical coordinate of the trailing edge is guessed, it is connected to the cut planes on both sides of the duct by using quadratic polynomials. The following conditions in Table 5.1 regarding the continuity of the geometry as well as slope should be satisfied in order to render a smooth duct shape. The iteration continues until the pressures at the points where the original trailing edge is located (here point P and S) become the same. This condition is henceforth referred as pressure equality condition and it has different standards under scenarios of bare ducts and ducted propellers. In the case of bare duct where the problem is axisymmetric, the pressures at different circumferential strips would be the same, and thus the pressure equality condition could be satisfied at any strips. While in the case of ducted propeller, the pressures at different circumferential strips would be different, the pressure equality condition is to be satisfied for the circumferential averaged pressure on the duct.

$$
\begin{aligned}
y_A &= A_1 x_A^2 + B_1 x_A + C_1 \\
\left.\frac{dy}{dx}\right|_A &= 2A_1 x_A + B_1 \\
y_B &= A_2 x_B^2 + B_2 x_B + C_2 \\
\left.\frac{dy}{dx}\right|_B &= 2A_2 x_B + B_2 \\
y_T &= A_1 x_T^2 + B_1 x_T + C_1 \\
y_T &= A_2 x_T^2 + B_2 x_T + C_2
\end{aligned}
$$

Table 5-1 Equations for continuity conditions of geometry and slope

5.3 Bare Duct with Blunt Trailing Edge

The extension scheme is applied to the bare duct shown in Figure 5.9, which has an almost horizontal suction side. In this case, the separation on the suction side is expected to start right at the original trailing. For the flow along the pressure side, a rational location for the cut plane would be determined, as will be seen shortly. Unlike the case of the long duct in previously chapter, the duct investigated here has a relatively small chord length / radius ratio, making it more challenging for the viscous-inviscid interactive method for resolve the effects of viscosity. Also as an accelerating duct, this duct shape is typical of specialized ducts practically used in the industry.

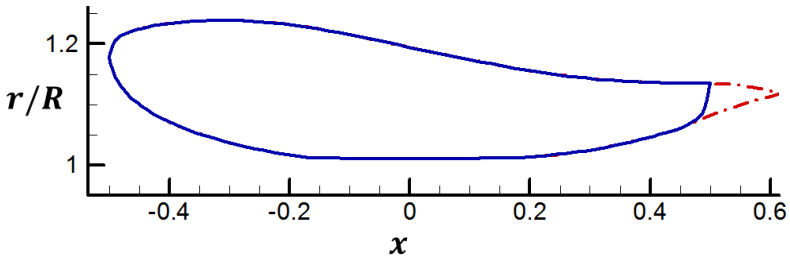

Figure 5.9 Original and modified shape of the bare duct

5.3.1 Determination of Cut Planes

The two-dimensional boundary layer solver utilized in the viscous/inviscid interactive method currently cannot satisfactorily solve the boundary layer structure when a blunt trailing edge is in presence. To determine the location of separation points ($C_f = 0$) so that the cut planes could be reasonably placed, an axisymmetric RANS simulation is performed in ANSYS Fluent. The same flow field is analyzed and the

resulted distribution of pressure and boundary layer structure parameters will be used for detailed correlation. The flow domain dimension and boundary conditions of the RANS simulation are presented in Figure 5.10.

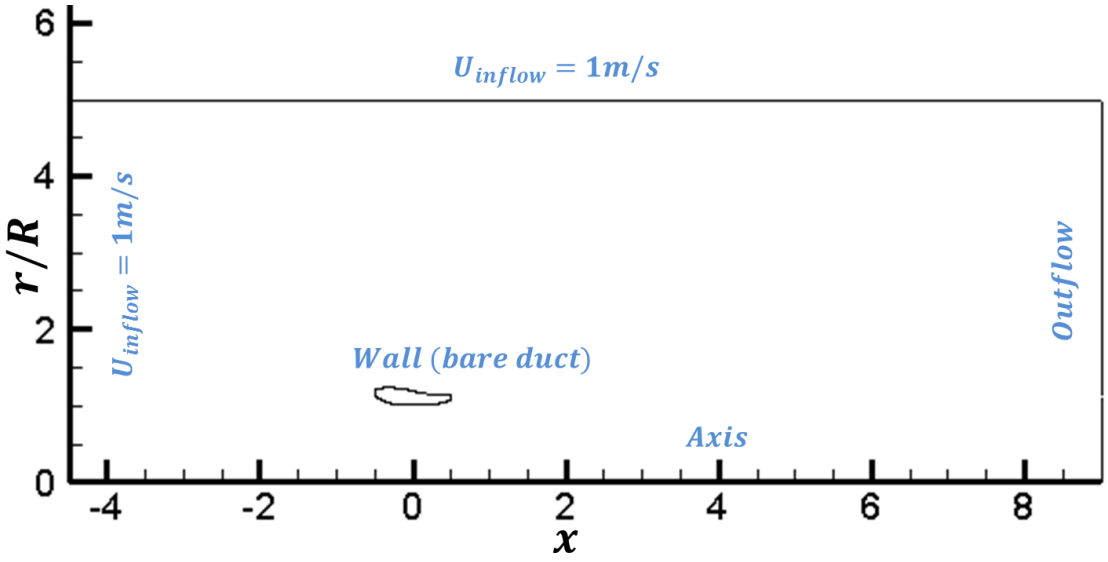

Figure 5.10 The flow domain and boundary condition of the RANS simulation

In order to capture the boundary layer structures, the mesh around the bare duct is made very fine through the enhance wall function in ANSYS Fluent, as shown in Figure 5.11. The value of wall y^+ is controlled with $O(10)$. With the presence of blunt trailing edge, the recirculation region needs also to be well meshed.

It should also be noted that the duct here is extracted from its corresponding ducted propellers. For better evaluation, the bare duct has been rotated about its leading edge so that an optimal angle of attack is achieved. The duct is rotated until there is no crossover in the plot of pressure distribution.

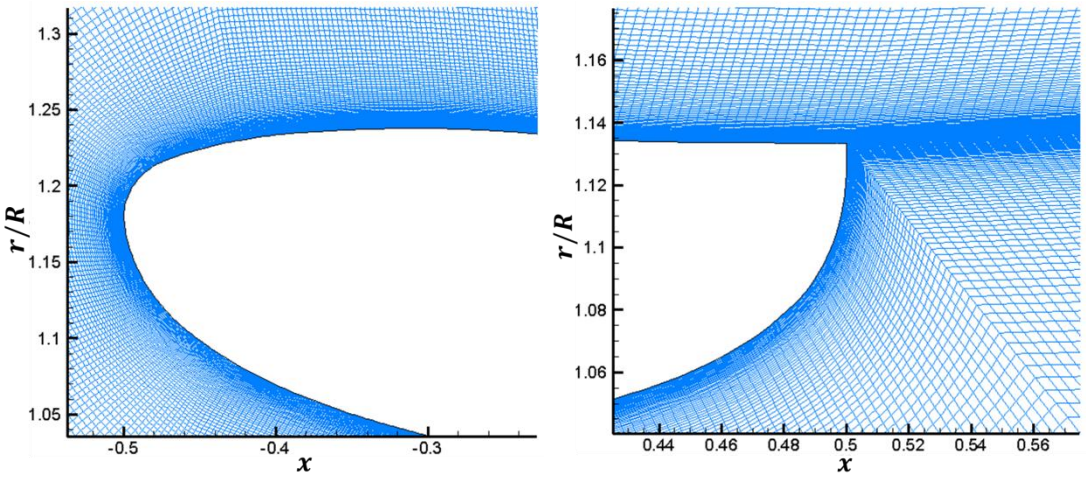

Figure 5.11 Fine gridding within the boundary layer and the recirculation zone

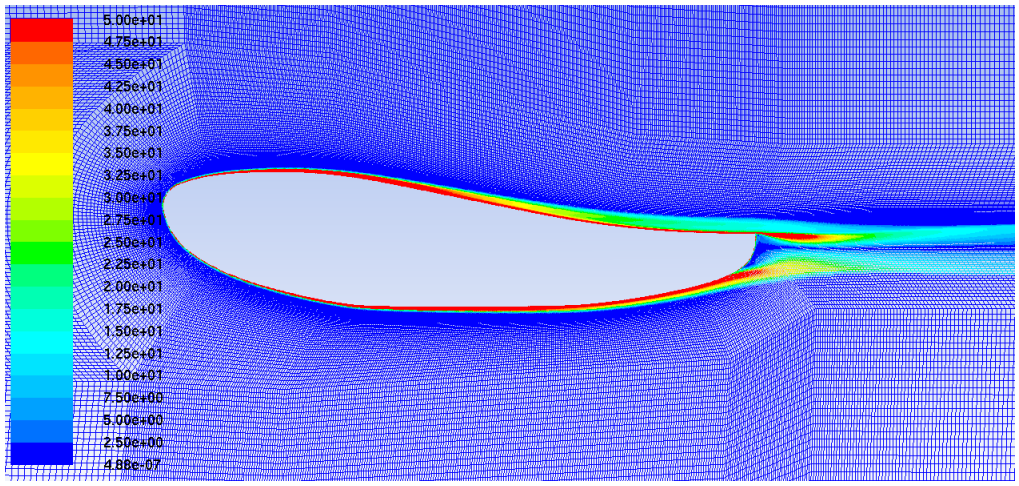

Figure 5.12 Contour of vorticity magnitude within the flow domain

The contour of vorticity magnitude from the axisymmetric RANS simulation is shown in Figure 5.12. A noticeable recirculation region is observed around the trailing edge. Since the duct has an almost horizontal suction side, the flow on this side begins separating right from the trailing edge. While on the pressure side, reversed flow is

observed from 96% duct length from the leading edge and this location is then used for the cut plane.

5.3.2 Correlation

The bare duct is modified through the present extension scheme by using the cut plane decided from the axisymmetric RANS run. The geometry and grid in the present viscous/inviscid interactive method is shown as in Figure 5.13.

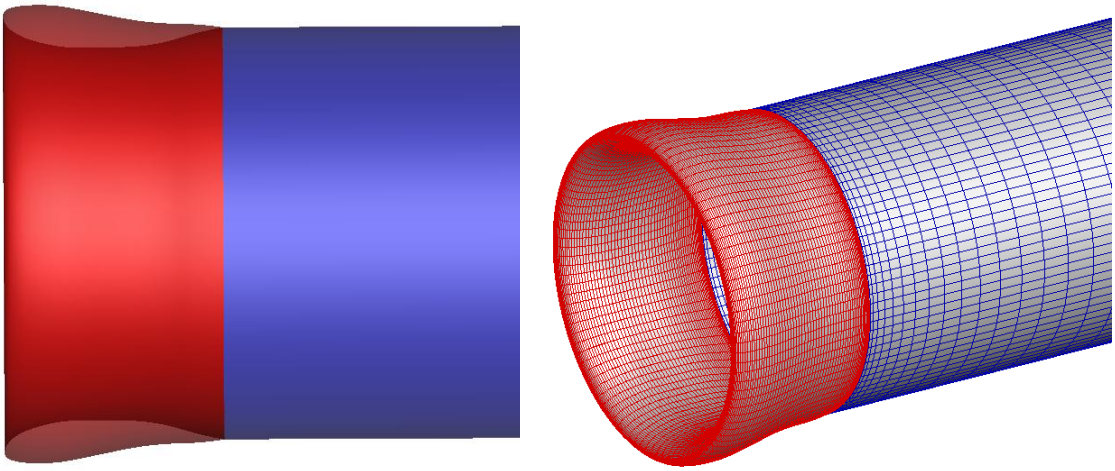

Figure 5.13 Geometry and gridding in viscous/inviscid interactive method

The circumferentially averaged pressure distribution on the duct from the viscous/inviscid interactive method is compared to that from the axisymmetric RANS simulation in Figure 5.14. In addition, the distribution of skin friction along the duct surface is also shown in Figure 5.15.

It should be noted that the axisymmetric RANS simulation adopts the original duct geometry while the viscous/inviscid interactive method uses the extended shape.

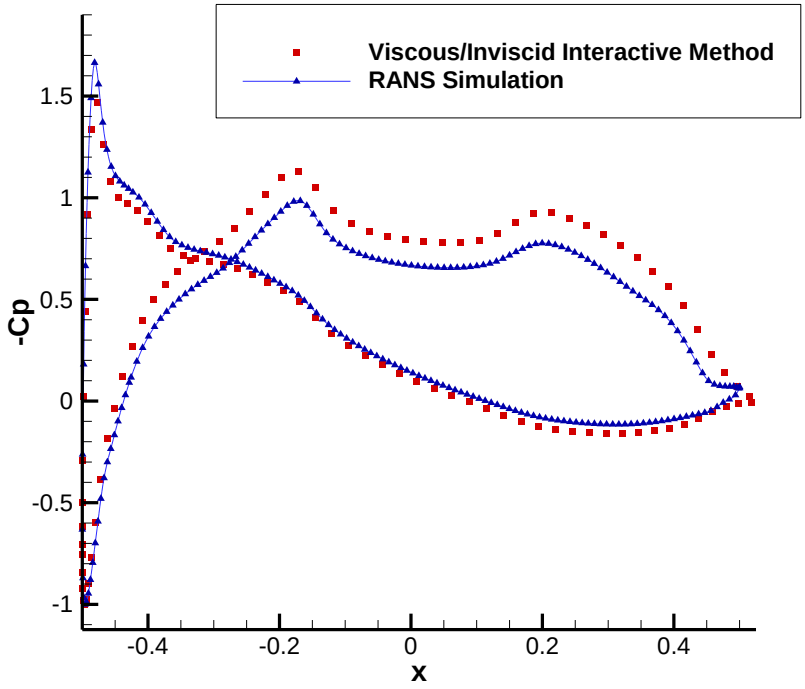

Figure 5.14 Correlation of pressure distribution

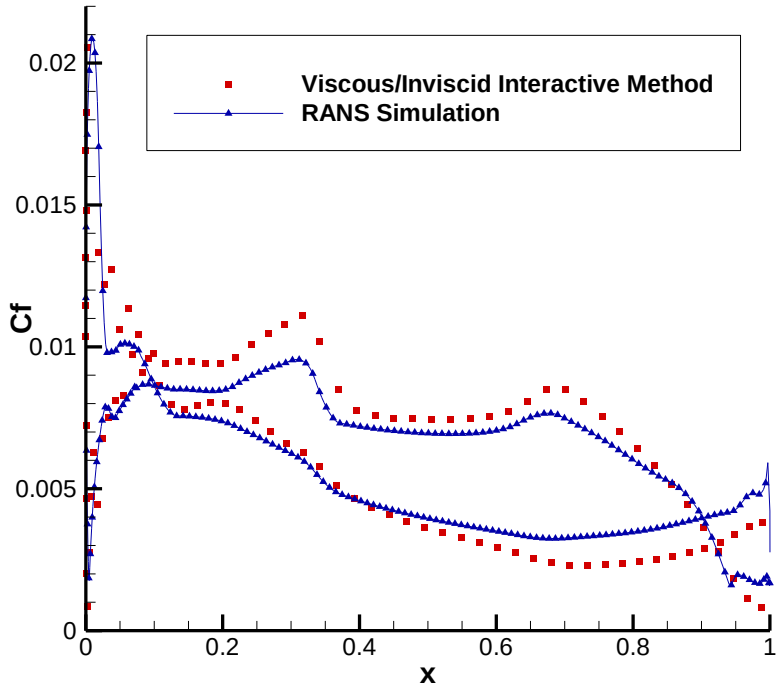

Figure 5.15 Correlation of skin friction on the duct

As can be observed, despite the challenging shape of duct, the results from the viscous/inviscid interactive method agree quite well with that from the RANS simulation. Also it is inspiring that the two-dimensional boundary layer solver performs well to extract information of the boundary layer structures. The effectiveness of the present extension scheme is also validated via this case.

5.4 Extension Scheme for Ducted Propeller with Blunt Trailing Edge Duct

A 4-blade ducted propeller from which the bare duct shape in last section is extracted is investigated in this section with the present extension scheme. An infinite long cylindrical hub is included in the study. The design advance ration of this propeller is around 0.70. The hybrid method that couples a potential Vortex-Lattice Method (VLM) solver with a RANS solver is also applied for detailed correlation. The correlation is carried out at the design advance. The 3-D geometry of the ducted propeller along with the 2-D section of its duct is shown in Figure 5.16.

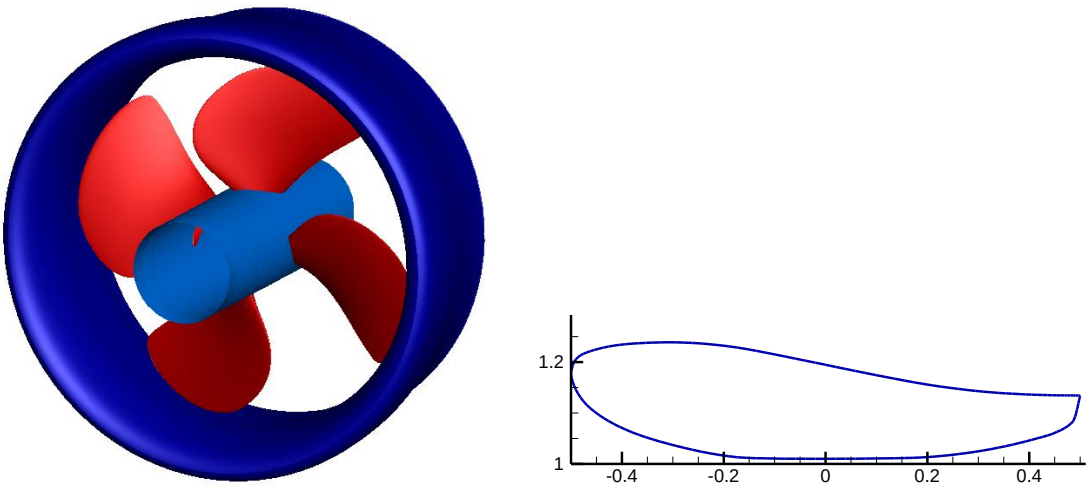

Figure 5.16 3-D geometry of the ducted propeller and the 2-D section of its duct

With a round-tip propeller in presence, the pressures at different circumferential strips would be different and the pressure equality condition of the extension scheme is to be satisfied for the circumferentially averaged pressure on the duct.

5.4.1 RANS-VLM coupling method

The body force within the blade zone of the RANS simulation is shown in Figure 5.17. As aforementioned, a reliable body force interpolation scheme has been here applied. Also shown in Figure 5.18 is the axial component of the effective wake calculated at the last iteration.

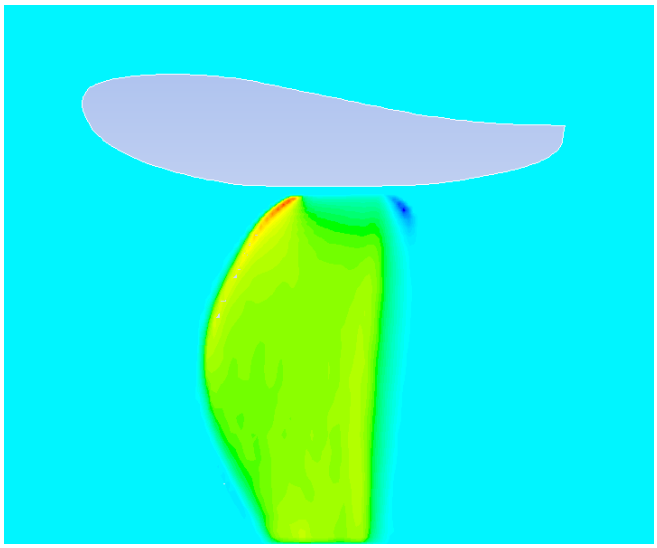

Figure 5.17 Body force within the blade zone of the RANS simulation

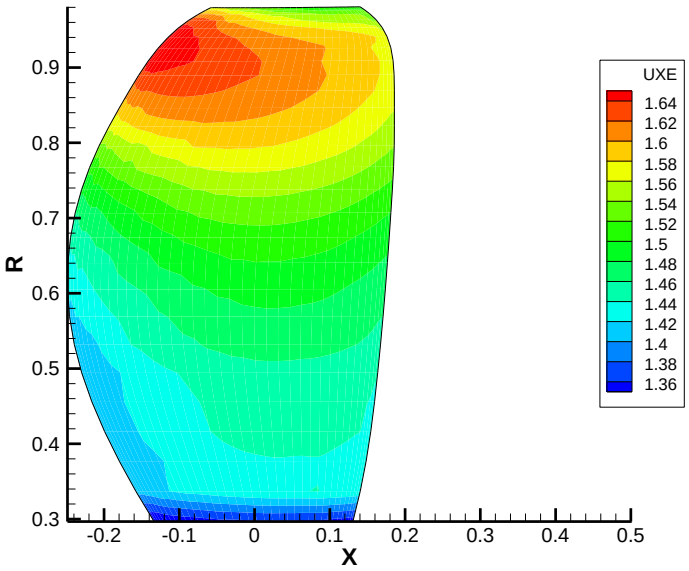

Figure 5.18 Contour of the axial velocity component of the effective wake calculated at the last iteration

The flow is found to starting separating from the pressure side of the duct from 96% duct length from the original trailing edge, which would be reasonably used as the cut plane location in the calculation of viscous/inviscid interactive method.

5.4.2 Correlations

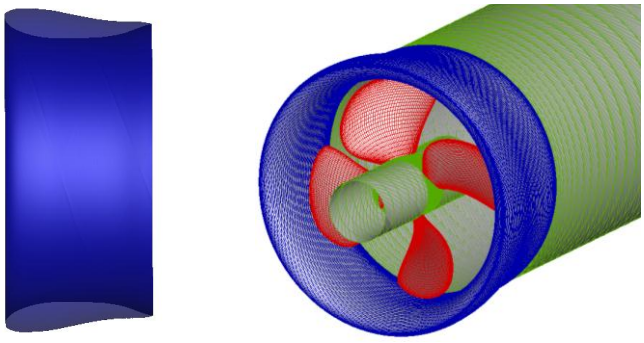

Figure 5.19 Extended duct shape and gridding of the ducted propeller in the viscous/inviscid interactive method

The duct shape in the viscous/inviscid interactive formulation is modified through the extension scheme and based on the separation point found in the RANS-VLM run above. The section of the extended duct and the paneling of the ducted propeller are shown in Figure 5.19.

The pressure calculated by the viscous/inviscid interactive method is correlated with that from the RANS/VLM coupling method. As is similar to bare duct case, the present interactive method can render fairly good prediction in terms of pressure. On the other hand, correlation of skin friction coefficient is presented in Figure 5.20, from which it is concluded that under the strong influence of the propeller, the two-dimensional boundary layer solver cannot satisfactorily resolve the boundary layer on the duct.

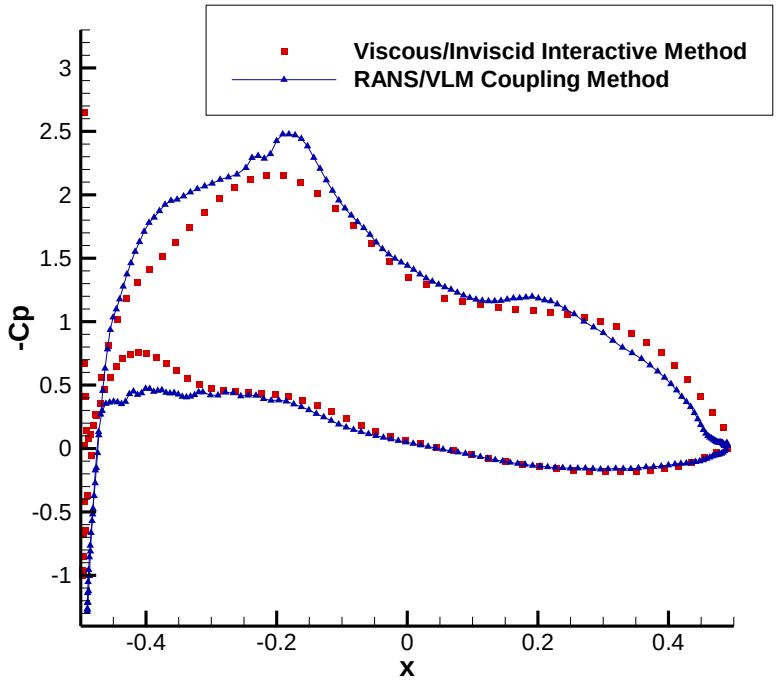

Figure 5.20 Correlation of pressure distribution on the duct between the two methods

Besides the duct, the performance of the bounded propeller needs also to be evaluated after the extension. The circulation about the blade is correlated in Figure XX. The two methods agree mainly very well except at the blade station near the hub.

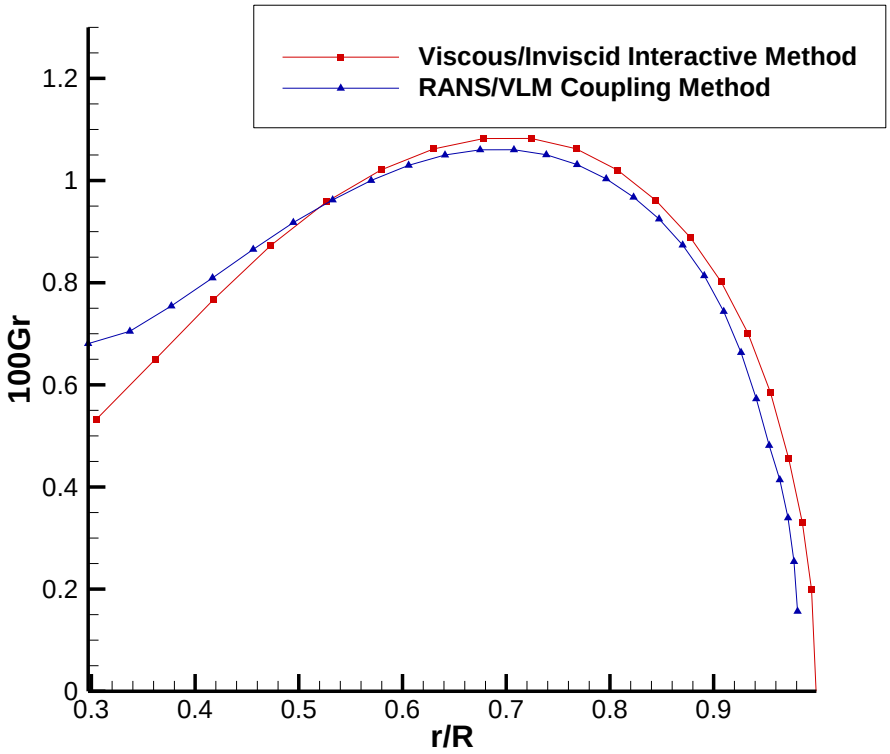

Figure 5.21 Correlation of circulation on blade

Chapter 6 Conclusions and Recommendations

6.1 Conclusions

In this thesis, an improved full wake alignment scheme has been implemented for cases of ducted propellers by aligning the trailing wake with the local velocity. The effects of the singularities on the duct and duct trailing wake, which used to be neglected, are included in the improved scheme. It has been adopted by a lower order panel method for prediction of performance of ducted propellers. It is observed the improved wake model can well represent the characteristics of roll-up at the wake tip especially under high loading conditions. It is further confirmed that at low advance ratios, whether contraction of the wake radius has been predicted (full wake alignment) or not (PSF-2 type scheme) will significantly affect the predicted overall force performance of the propeller. The predicted force from the panel method with either wake model agree well with experimental data, full blown RANS simulations and a RANS/VLM coupling method at high advance ratios. However, as the advance ratio becomes smaller, the force predicted by the PSF-2 type scheme starts deviating from that from other methods. At the same time, the force from the full wake alignment model is still in good agreement with full blown RANS simulations and experimental measurements. The detailed pressure distribution on the blades and duct surface has also been investigated the related correlations has been performed between the lower order panel method and a RANS/VLM hybrid method and full blown RANS simulation. Very good agreement has

been achieved by the full wake alignment model at several radial sections and under various loading conditions for two different types of ducted propellers.

An extension scheme has been initially proposed by Pan (2009) and subsequently developed by Yu (2012) and Purohit (2013) for reasonable modification of the aft part of bare ducts with non-zero trailing edge thickness or ducted propellers with blunt trailing edge duct. In this thesis, a major improvement has been to set up the rigorous criterion of C_f=0 for determining the cut planes or the starting points of the extension.

To involve the effects of viscosity into analysis, a viscous/inviscid interactive method has been introduced and applied to different types of flows: the axisymmetric flow of a long duct, the axisymmetric of a bare duct with non-zero trailing edge thickness and the three-dimensional flow around a ducted propeller with a blunt trailing edge duct. For the latter two cases, the recirculation zone around the blunt trailing edge of the duct cannot be well addressed by the present method. Therefore the improved extension scheme has been utilized for reasonable modification. Satisfactory agreement of the pressure distribution on the duct has been obtained between the interactive method and other methods, i.e. the axisymmetric RANS simulation and the RANS/VLM hybrid method.

6.2 Recommendations

In the improved full wake alignment scheme, the process of repaneling the duct has been involved which might cause the following problems. The paneling in the mid part of the duct normally needs to follow the blade panel distribution in which cosine spacing is

usually applied for better resolution of the blade leading edge and trailing edge. Thus there will be an abrupt transition of panel size from the last panel of the mid part to the first panel to the aft part of the duct. Also since the panel size in the aft part of the duct is largely decided by the blade wake, there might be panels of large size near the trailing edge of the duct, causing some problem of satisfying the iterative Kutta condition within the present panel method. Efforts must be made to overcome these types of numerical inaccuracies.

In the current viscous/ inviscid interactive method, only the effects of viscosity on the duct have been assumed and investigated. It is also crucial to obtain the viscous influence on the propeller blades. The current interactive formulation should also be applied to the blades so that a more reliable performance prediction of open propellers as well as ducted propellers can be achieved.

Appendix

Appendix A. Study for Duct alone with Straight and Distorted Panels

In this chapter, a study for duct alone with straight and distorted panels is presented. The duct shape from the round tip ducted propeller in Chapter 4 is adopted. The distorted panels are exported from the run where the propeller is in presence and the duct panels are aligned with the blade wakes. Since the pitch of the blade wakes decreases as the loading of the ducted propeller increases, distorted panels are obtained at the design loading condition. Such distorted panels are then loaded into the duct alone case for study of effects of duct paneling on the performance of the present panel method.

The duct propeller run is firstly executed at *Js*=0.40 with 200×80 (chordwise × circumferential) panels for resolving the duct surface. It should be noted that 80 elements in the circumferential direction would result to 20 panels between blades for a 4-bladed propellerThe duct paneling from the run of ducted propeller is shown as Figure A.1.

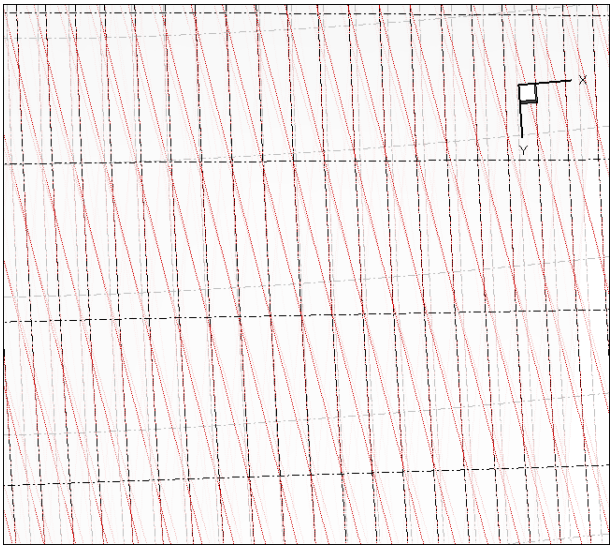

Figure A.1 Distorted panels (120×80, red dotted line) from ducted propeller run compared with straight panels (120×80, black dash dotted line)

In Figure A.2, a correlation has been made between the circumferentially averaged pressure distributions from the two duct panel types.

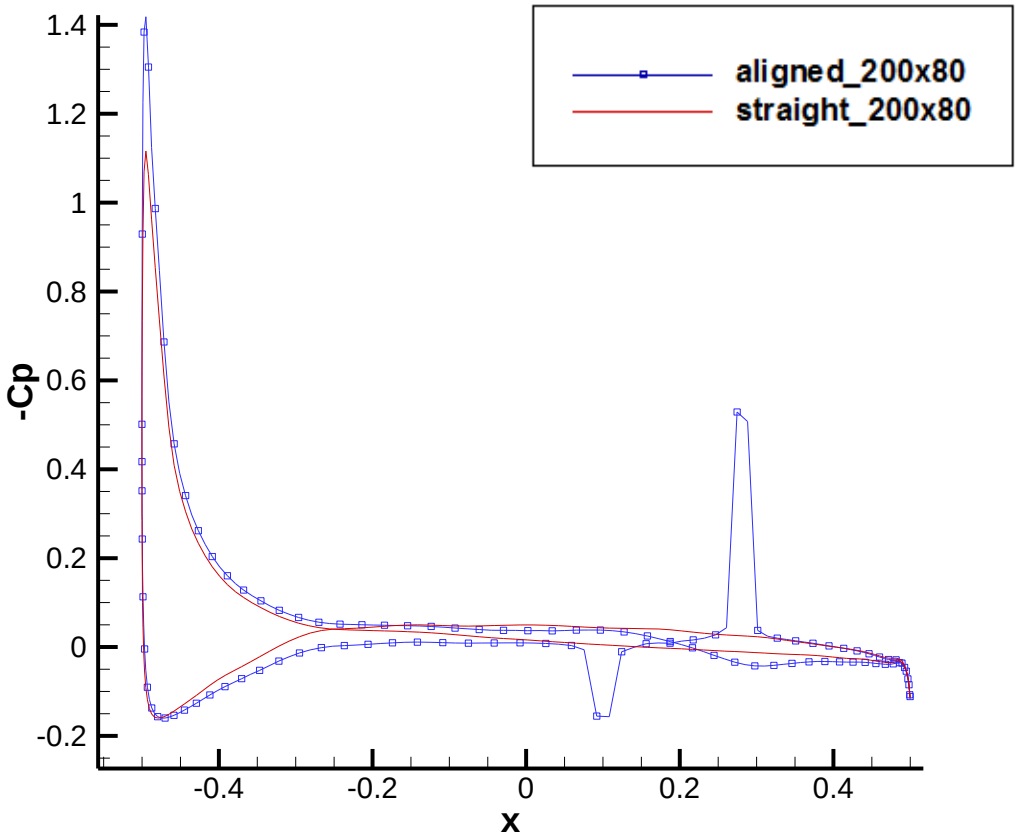

Figure A.2 Correlation of circumferentially averaged pressure distribution between straight duct panels (120×80) and distorted or aligned duct panels (120×80)

Two unreasonable pressure spikes have been observed which are assumed to be caused by not having enough panels for resolving the duct. Therefore a similar run of ducted propeller is performed with an increased number of panels (120×160) on the duct. The new correlation of circumferentially averaged pressure distribution between the straight panels (120×80) and distorted panels (120×160) is indicated in Figure A.3.

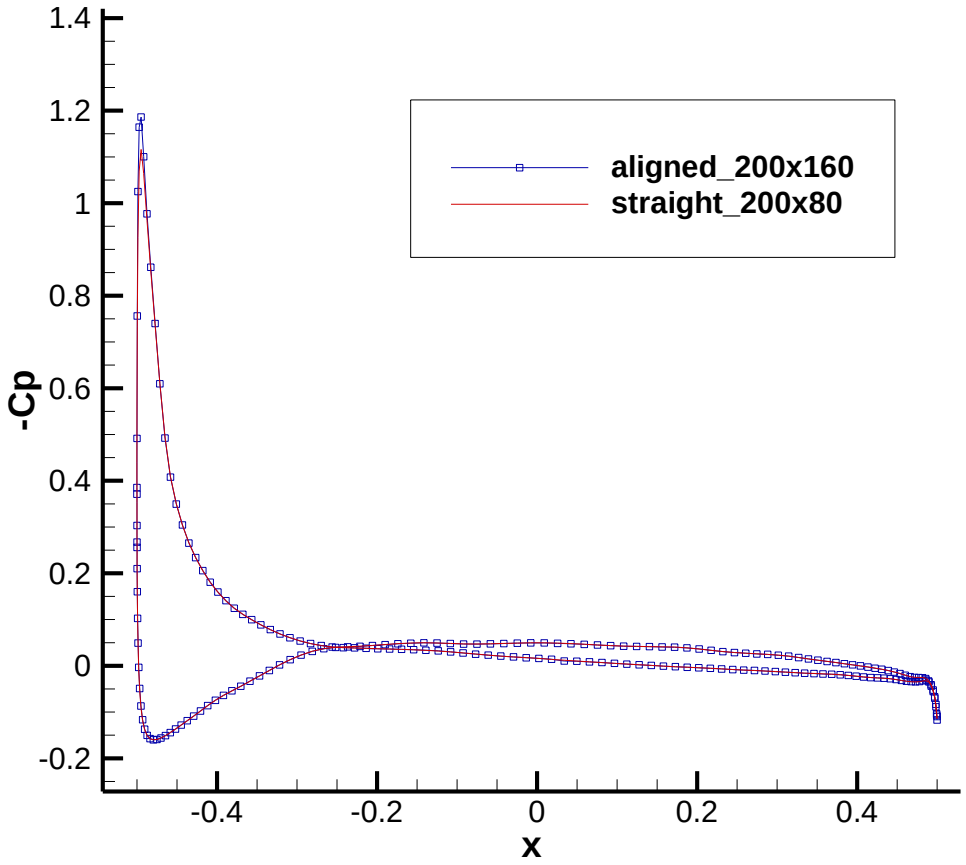

Figure A.3 Correlation of circumferentially averaged pressure distribution between straight duct panels (120×80) and distorted or aligned duct panels (120×160)

Figure A.3 shows that as the number of circumferential panels on the duct is increased, the result from the distorted duct panels agrees very well with that from the straight duct panels. This is reasonable since in order to follow the blade wake pitch, the aligned duct panels would have large skewness and more panels would be required to better resolve the duct surface.

Bibliography

[1] Hess, J. L. "Calculation of non-lifting potential flow about arbitrary three dimensional bodies." Journal of Ship Research 8, no. 2 (1964): 22-44.

[2] Gibson, I., and R. I. Lewis. "Ducted propeller analysis by surface vorticity and actuator disk theory." In Proceedings of the Symposium on Ducted Propeller, RINA, Teddington, England. 1973.

[3] Hess, John L., and Walte O. Valarezo. "Calculation of steady flow about propellers using a surface panel method." Journal of Propulsion and Power 1, no. 6 (1985): 470-476.

[4] Morino, Luigi, and Ching-Chiang Kuo. "Subsonic potential aerodynamics for complex configurations: a general theory." AIAA journal 12, no. 2 (1974): 191-197.

[5] Lee, Jin-tae. "A potential based panel method for the analysis of marine propellers in steady flow." PhD diss., Massachusetts Institute of Technology, 1987.

[6] Kerwin, Justin E., and Chang-Sup Lee. Prediction of steady and unsteady marine propeller performance by numerical lifting-surface theory. No. Paper No. 8. 1978.

[7] Greeley, David Scott, and Justin Elliot Kerwin. "Numerical methods for propeller design and analysis in steady flow." Transactions-Society of Naval Architects and Marine Engineers 90 (1982): 415-453.

[8] Kinnas, S., and S. Pyo. "Propeller wake alignment models in uniform and inclined inflow." In Propellers/Shafting'97 Symposium, Virginia Beach, VA. Soc. Naval Arch. & Marine Engnrs. 1997.

[9] Pyo, S., and S. A. Kinnas. "Propeller wake sheet roll-up modeling in three dimensions." Journal of ship research 41, no. 2 (1997): 81-92.

[10] Lee, Hanseong, and S. A. Kinnas. "Application of a boundary element method in the prediction of unsteady blade sheet and developed tip vortex cavitation on marine propellers." Journal of ship research 48, no. 1 (2004): 15-30.

[11] Tian, Ye and S. A. Kinnas. "A wake model for the prediction of propeller performance at low advance ratios." International Journal of Rotating Machinery 2012 (2012).

[12] Drela, Mark. "XFOIL: An analysis and design system for low Reynolds number airfoils." In Low Reynolds number aerodynamics, pp. 1-12. Springer Berlin Heidelberg, 1989.

[13] Milewski, William Michael. "Three-dimensional viscous flow computations using the integral boundary layer equations simultaneously coupled with a low order panel method." PhD diss., Massachusetts Institute of Technology, 1997.

[14] Hufford, Gary Scott. "Viscous flow around marine propellers using boundary layer strip theory." PhD diss., Massachusetts Institute of Technology, 1992.

[15] Hufford, Gary S., Mark Drela, and Justin E. Kerwin. "Viscous flow around marine propellers using boundary-layer strip theory." Journal of ship research 38, no. 1 (1994): 52-61.

[16] Sun, H. "Performance prediction of cavitating propulsors using a viscous/inviscid method." PhD dissertation, CAEE, UT Austin, 2008.

[17] Sun, H. and Kinnas, S. A. "Performance prediction of cavitating water-jet propulsors using a viscous/inviscid interactive method." Proc. 2008 SNAME Annual Meeting and Ship Production Symposium, Houston, TX, 2008.

[18] Yu, X. “Three dimensional viscous/inviscid interactive method and its application to propeller blades,” Master thesis, CAEE, UT Austin, 2012.

[19] S. A. Kinnas, X. Yu and Y. Tian. “Prediction of propeller performance under high loading conditions with viscous/inviscid interaction and a new wake alignment model,” In 29th Symposium on Naval Hydrodynamics, August 2012.

[20] Purohit, J. (2013), “An Improved Viscous-Inviscid Interactive Method and its Application to Ducted Propellers,” Master thesis, CAEE, UT Austin, 2013.

[21] S. A. Kinnas, C. H. Jeon, J. B. Purohit and Y. Tian. “Prediction of unsteady cavitating performance of ducted propellers.” In Third International Symposium on Marine Propulsors (smp2013), 2013.

[22] Tian, Y. and Kinnas, S.A., “Thruster and Hull Interaction”, Journal of Offshore Mechanics and Arctic Engineering. 137(4), 041801, Aug 01, 2015.

[23] Preliminary Documentation for PBD-10 Computer Program, MIT Department of Ocean Engineering, 1981.

[24] Loukakis, Theodore A. A new theory for the wake of marine propellers. No. 71-1 DR Thesis. 1971.

[25] Kinnas, S. A., S. H. Chang, Y. H. Yu, and L. He. "A hybrid viscous/potential flow method for the prediction of the performance of podded and ducted propellers." In Proceedings of the Propeller and Shafting Conference, Williamsburg, VA, pp. 1-13. 2009.

[26] Pan, Yulin. "A Viscous/Inviscid Interactive Approach and Its Application to Wetted or Cavitating Hydrofoils and Propellers with Non-zero Trailing Edge Thickness." PhD diss., University of Texas at Austin, 2009.

Vita

Hongyang Fan was born in Jiangyin, Jiangsu, China. He received the Bachelor of Science in Naval Architecture & Ocean Engineering from Shanghai Jiao Tong University, China in July, 2013. In August 2013, he started his graduate studies as a member of the Ocean Engineering Group at the University of Texas at Austin.

Address:hongyangfan@utexas.edu

This manuscript was typed by Hongyang Fan.